UNIVERSITY OF CALIFORNIA, SAN DIEGO

Analytic Closed-Form Solution of a Mixed Layer Model for Stratocumulus Clouds

A dissertation submitted in partial satisfaction of the
requirements for the degree
Doctor of Philosophy

in

Engineering Sciences (Mechanical Engineering)

by

Bengu Ozge Akyurek

Committee in charge:

Professor Jan Kleissl, Chair
Professor Marcelo Chamecki
Professor Carlos Coimbra
Professor Joel Norris
Professor David Saintillan

2017

The dissertation of Bengu Ozge Akyurek is approved, and it is acceptable in quality and form for publication on microfilm and electronically:

_____

_____

_____

_____

_____
Chair

University of California, San Diego

2017

DEDICATION

To my husband Sinan-Arrowhead, my beautiful daughter Ahu Gokce, my parents, brother and my big family, Serifogullari

EPIGRAPH

Fear is the mind killer.

—Dune, Frank Herbert

TABLE OF CONTENTS

LIST OF FIGURES

LIST OF TABLES

ACKNOWLEDGMENTS

I would like to start by thanking my advisor Prof. Jan Kleissl for his unlimited patience and support throughout my PhD. His never ending tolerance and knowledge has kept me in the right direction throughout years. Over the years, there were many ups and downs, successes and failures, trials and errors in my case as a PhD student. I am extremely grateful for the opportunities and the time he gave me not only in my academic life but also to a mother who wants to care for her newborn baby. I would like to thank my committee members, Prof. Joel Norris, Prof. Carlos Coimbra, Prof. Marcelo Chamecki, Prof. David Saintillan for their valuable discussions, feedback and contributions to this work.

I would like to thank all my lab mates and friends in Solar Resource Assessment and Forecasting Laboratory, both current and past, for their comments, feedback, discussions and guidance. It was a privilege to work with and and alongside them. I am grateful to all of them but I would also like to give special thanks to Patrick Mathiesen, Mohamed Ghonima, Xiaohui Zong, Handa Yang, Monica Zapata and Elynn Wu.

Most importantly, I owe so much to my husband. Without his support with our daughter, I wouldn't have been able to finish this thesis with a baby in a shorter time than expected. Thank you Sinan for being there for me after every failure and success, thank you for understanding how hectic a young mother's life can be while all the impossibilities were surrounding us. I also would like to thank my mom, as an extraordinary teacher, for teaching me how to pursue a career and how to balance the job and private life; always putting the family in the first place, never give up and be ambitious. I would like to thank my father for teaching me, as a respected dentist, that career, success and the ambitions are not important as long as the attitude towards people is poor or the character of a person is shallow. I would also like to thank my brother who made me laugh out loud at his jokes and stories every time we Skype. Last but not least, I would like to thank my biggest fan, my daughter Ahu Gokce, for supporting me with her hugs and kisses, and sometimes cryings. I started this PhD for myself but finishing it for us, my beautiful baby.

Chapter 1, 2 and 3 contain work that has been accepted to be published in B. Ozge Akyurek, Jan Kleissl, "Closed-Form Analytic Solution of Cloud Dissipation for a Mixed-Layer Model", AMS Journal of Atmospheric Sciences 2017. The dissertation author was the primary investigator and author of this paper.

Chapter 4 contains work that is currently being prepared for submission for publication as it may appear in B. Ozge Akyurek, Jan Kleissl, "Effect of Large Scale Horizontal Advection on Cloud Thickness Evolution for a Mixed-Layer Model", soon to be submitted to AMS Journal of Atmospheric Sciences. The dissertation author is the primary investigator and author of this paper.

VITA

2005	B. Sc. in Environmental Engineering, Yildiz Technical University, Istanbul - Turkey
2011	M. Sc. in Environmental Engineering, Hacettepe University, Ankara - Turkey
2017	Ph. D. in Engineering Sciences (Mechanical Engineering), University of California, San Diego

PUBLICATIONS

B. Ozge Akyurek, A. Sinan Akyurek, Jan Kleissl, Tajana S. Rosing, "TESLA: Taylor Expanded Solar Analog Forecasting", IEEE SmartGridComm 2014

B. Ozge Akyurek, Jan Kleissl, "Closed-Form Analytic Solution of Cloud Dissipation for a Mixed-Layer Model", AMS Journal of Atmospheric Sciences 2017

B. Ozge Akyurek, Jan Kleissl, "Effect of Large Scale Horizontal Advection on Cloud Thickness Evolution for a Mixed-Layer Model", soon to be submitted to AMS Journal of Atmospheric Sciences

ABSTRACT OF THE DISSERTATION

Analytic Closed-Form Solution of a Mixed Layer Model for Stratocumulus Clouds

by

Bengu Ozge Akyurek

Doctor of Philosophy in Engineering Sciences (Mechanical Engineering)

University of California, San Diego, 2017

Professor Jan Kleissl, Chair

Stratocumulus clouds play an important role in climate cooling and are hard to predict using global climate and weather forecast models. Thus, previous studies in the literature use observations and numerical simulation tools, such as large-eddy simulation (LES), to solve the governing equations for the evolution of stratocumulus clouds. In contrast to the previous works, this work provides an analytic closed-form solution to the cloud thickness evolution of stratocumulus clouds in a mixed-layer model framework. With a focus on application over coastal lands, the diurnal cycle of cloud thickness and whether or not clouds dissipate are of particular interest. An analytic solution enables the sensitivity analysis of implicitly interdependent variables and extrema analysis of cloud variables that

are hard to achieve using numerical solutions. In this work, the sensitivity of inversion height, cloud-base height, and cloud thickness with respect to initial and boundary conditions, such as Bowen ratio, subsidence, surface temperature, and initial inversion height, are studied. A critical initial cloud thickness value that can be dissipated pre- and post-sunrise is provided. Furthermore, an extrema analysis is provided to obtain the minima and maxima of the inversion height and cloud thickness within 24 h. The proposed solution is validated against LES results under the same initial and boundary conditions. Then, the proposed analytic framework is extended to incorporate multiple vertical columns that are coupled by advection through wind flow. This enables a bridge between the micro-scale and the meso-scale relations. The effect of advection on cloud evolution is studied and a sensitivity analysis is provided.

Chapter 1

Introduction

Atmospheric sciences focus on the everyday atmospheric processes that govern every aspect of our lives, directly or indirectly. It studies how and why our climate behaves the way it does, and what its next state will be in not just the next day, but also in the next century. This dissertation focuses on the stratocumulus clouds, a type of cloud that is very frequently observed in our lives and has a high impact on our global climate balance. Our climate effects many aspects of our lives. The air surrounds us all and we react to the changes in the climate. Our infrastructures ([1]), agriculture ([2]) and other species are affected by climate ([3]). Air traffic, wind and photovoltaic energy generation are processes that are directly governed by the immediate changes in climate ([4]).

The atmospheric process is highly inter-connected and very complex to solve as a whole. Studies are divided across multiple branches based on the scales of areas ranging from micro-processes to global scale ([5]), various time-scales starting from turbulent processes at sub-seconds ([6]) to global events at multiple days to seasons ([7]), and different aspects of chemistries such as cloud formation ([8]), drizzle ([9]) and pollutant distribution ([10]).

In a stable atmosphere, warm air is buoyant and rises over the colder air in its surrounding. Therefore, we would expect a temperature distribution in accordance. However, turbulence mixes the air and creates a more uniform region with similar thermodynamic properties. The region above the turbulent *boundary layer* (BL) is still warmer than the mixed region and a sharp temperature increase

occurs above the BL. This *temperature inversion* acts as a cap over the BL, keeping it turbulent, mixed and more uniform. Inside the BL, if the air has enough water vapor and the temperature is cool enough, the water vapor will saturate and create a *cloud layer*. This cloud layer mostly ends at the inversion cap as the sudden increase in temperature inhibits saturation. The end result is a cloud layer that stretches over larger areas and has uniform upper-bound: the *Stratocumulus* (Sc).

Since the mixing in the BL is through turbulence, the length and time scales need to be selected accordingly to caputure the turbulent effects. The scale concentrating on the turbulence is called the *micro-scale*. The time resolution is on the order of seconds and the length scale is within only a couple kilometers. This doesn't mean that it is enough to study on the micro-scale to obtain a model and solution for Sc. The micro-scale processes are highly affected by larger scale processes that are occuring in the BL. But, it means that we need to go to the micro-scale to accurately explain the cloud formation and dissipation processes of Sc.

At the cloud-top, the turbulent BL is always interacting with the stratified free-troposphere region above it. Turbulence slowly mixes with the warmer and drier air above it, causing the BL to get warmer and drier. This process is called the *entrainment*. The interaction of the turbulent air with the stratified air is an active research topic ([11]).

At the surface, we have the interaction of air with either a solid on land or a liquid over water surfaces. Since air has different properties compared to the surface material, it will have different thermodynamic properties and a thermodynamic process will occur between the air and the surface. If the surface is warmer, it will heat the air and cool the air if it is cooler. Furthermore, the moisture inside the surface will effect the water vapor concentration of the air through either condensation or evaporation. Surface models for different surface types and how to determine the properties of the surface through different measurement techniques are active research areas ([12]).

Another important property of the atmosphere is that it is constantly moving. Different temperature distributions across different locations lead to pressure

differences due to buoyancy. This pressure difference causes the air to move from a high pressure location to a low pressure one. During this movement, the incoming air has its own properties and highly changes what is observed over a fixed location in an eulerian frame of reference. The change in properties due to wind flow is an *advection* process and can have drastic effects on local climate. Since the pressure differences occur over larger distances, we need to consider a different scale; *meso-scale*. This scale studies multiple kilometers and larger areas over a longer time-scale resolution of minutes or hours. Advection is very effective on the micro-scale because it introduces external effects onto the micro-scale processes, creating conditions that are not possible under isolated conditions. For coastal areas, advection is a major factor in cloud formation and dissipation as two surface types with very different properties connect over the airmass residing over them. Water has a higher heat capacity and its temperature varies slower as compared to a solid land surface. This causes temperature and pressure differences across day and night creating a *sea-breeze circulation*. Cooler air at the surface, due to its higher pressure, flows from the ocean to the land. Over the land, this air parcel warms up and rises, creating a high pressure at higher altitudes and flowing back to the ocean resulting in a large circulation.

Pressure differences across different airmasses can occur due to the surface differences. Depending on the topography, different pressure points can naturally occur over the world. Large regions of land or ocean, coriolis forces due to Earth's rotation and the different heating rates across latitudes are natural factors contributing to these pressure regions. High pressure regions have a tendency to *diverge* and flow towards low pressure regions, where the air *converges*. This creates a tendency of air flow over a large region that can have major effects on the smaller scales of atmospheric processes. The study of these regions is on a *synoptic-scale* and go into the research area of global climate models ([13]). From the perspective of the BL, if the region is a high pressure area, the air will be *subsiding* causing a a down-push on the inversion cap and the BL. This will be counteracting the entrainment process, keeping the inversion layer intact.

As discussed in the examples above, climate is a complex and whole process.

In this dissertation we first focus on the micro-scale side to study the cloud formation and dissipation process of Sc over coastal lands, excluding the meso-scale effects in isolated conditions. Then, we introduce the meso-scale advection effects in a coastal region to study the effects of sea-breeze circulation on the cloud process. The synoptic-scale effect of divergence is included in all solutions as subsidence.

1.1 Motivation

Stratocumulus clouds (Sc) cover 21% of the earth's surface on average annually and have a relatively high albedo resulting in a cooling contribution to climate ([14, 15]). Sc also impact Photovoltaic (PV) generation output in coastal areas such as Southern California ([16]). Sc are prevalent over the ocean and the coast line, but less so inland, yet there are also studies focusing on continental Sc (e.g. [17]). Their global abundance and the increase in coastal populations make it important to accurately model and forecast their behavior. However, global forecast models fail to accurately represent and forecast Sc ([18]).

Sc generally form under a strong inversion layer and the resulting BL is spatially homogeneous and well mixed day and night due to buoyant turbulence forcing from longwave cooling at the cloud top ([19, 20]). In observational studies, it has been shown that Sc can also form during the day under decoupled conditions, especially for deeper BLs and stronger winds, temperature and moisture gradients, yet they are less prevalent to the well-mixed cases ([21, 22]). Mixed layer models (MLM) are therefore an appropriate tool and have been widely applied to Sc since the groundbreaking work of [19]. Many studies improved physical model components such as entrainment ([23, 24, 25]), radiation ([26, 27]), surface fluxes ([20]), and advection ([28]). MLM are typically numerically integrated, validated against other numerical simulations such as Large Eddy Simulation (LES), and applied to study specific cases or sensitivities in the Sc topped BL ([29] and references within). Numerical integration is required due to the fact that the MLM integro-differential equations are often very complex with multiple feedback loops ([30]). However, to understand interdependencies between variables or sensitivity of the system to

a parameter, multiple case studies and simulations need to be performed. Even then, hidden interdependencies or feedback effects may not be discovered using trial and error methods.

There are also studies that use analytic models to understand the underlying behaviors ([31, 32, 23]). These studies focus on the modeling various aspects of a physical phenomenon with more accurate analytic equations. However, these analytic expressions are not used for solving the time evolution of cloud variables in an analytic fashion.

In this dissertation, we build up a physical MLM with radiation, buoyancy flux, and surface schemes and use mathematical approximations to obtain a closed-form analytic solution to inversion height, cloud base height, and ultimately cloud dissipation. The advantage of an analytic solution is that the dependencies and sensitivities are observable directly from equations. For example, and related to our application of solar forecasting over coastal lands, the dependence of cloud thickness on Bowen ratio can be directly inferred, given the initial conditions of the system. The temporal evolution of the system can be described without numerical approximations and steady state conditions or attraction points can be detected.

We provide sensitivity and extrema analysis for inversion height, cloud base height and cloud thickness, to infer how they depend on the initial and boundary conditions, and understand when their minima and maxima occur during the diurnal cycle.

1.2 Thesis Outline

This dissertation is structured as follows. Chapter 2 starts with a background on the models that constitute the governing system of equations for the rest of the dissertation. Chapter 3 introduces the closed-form analytic solution to a mixed-layer model base air column and contains detailed analysis on the sensitivity of inversion height, cloud base height and cloud thickness evolution in time with respect to the system parameters and initial conditions, and the timing of their extrema during the diurnal cycle. Chapter 4 extends the closed-form analytic

solution to multiple vertical columns that are coupled through advection and windflow, and provides detailed analysis. Finally, Chapter 5 concludes this dissertation and provides future directions.

1.3 Nomenclature

α_{lw} Optical depth scale for longwave radiation

α_{srf} Surface turbulent efficiency

$\mathrm{A_w}$ Entrainment tuning parameter

$\mathrm{B_{cld}}$ Cloud effective blackbody radiation

β Bowen Ratio

$\mathrm{B_{srf}}$ Surface effective blackbody radiation

$\mathrm{B_{sky}}$ Effective downwelling longwave radiation above the cloud top

$\mathrm{c_p}$ Specific heat constant

$\Delta q_{\mathrm{T,\,i}}$ Total water vapor mixing ratio jump at the inversion

$\Delta \theta_{\mathrm{l,\,i}}$ Liquid potential temperature jump at the inversion

$\Delta \theta_{\mathrm{v,\,i}}$ Virtual potential temperature jump at the inversion

$\mathrm{F_{lw}}$ Net longwave radiation flux

$\mathrm{F_{rad}}$ Net radiation flux

$\mathrm{F_{sw}}$ Net shortwave radiation flux

$\mathrm{g_{lw}}$ Asymmetry factor for longwave radiation

$\mathrm{g_{sw}}$ Asymmetry factor for shortwave radiation

$\mathrm{L_v}$ Latent heat of evaporation

μ_0 Cosine of the solar zenith angle

ω_{lw} Single scattering albedo for longwave radiation

ω_{sw} Single scattering albedo for shortwave radiation

q_{l} Liquid water mixing ratio

q_{T} Total water vapor mixing ratio

$q_{\mathrm{T,\ adv}}$ Horizontal advection of water vapor mixing ratio

$q_{\mathrm{T,\ inv}}$ Total water vapor mixing ratio at the inversion

$\mathrm{R_d}$ Gas constant for dry air

$\mathrm{R_e}$ Effective droplet radius

ρ_{air} Density of air

ρ_{W} Density of water

Ri Richardson number

$\mathrm{R_v}$ Gas constant for moist air

τ_{b} Optical depth of the cloud

$\mathrm{T_{base}}$ Cloud base temperature

$\mathrm{T_{cld}}$ Effective radiative cloud temperature

θ_{l} Liquid potential temperature

$\theta_{\mathrm{l,\ adv}}$ Horizontal advection of liquid potential temperature

$\theta_{\mathrm{l,\ inv}}$ Liquid potential temperature at the inversion

θ_{v} Virtual potential temperature

$\theta_{\mathrm{v,\ 0}}$ Virtual potential temperature reference

T_{srf} Surface temperature

T_{sky} Effective downwelling radiative temperature above the cloud top

$\mathbf{v}_H$ Horizontal wind speed

w_e Entrainment velocity

$\overline{w'q'_T}$ Mean turbulent flux for total water vapor mixing ratio

w_s Subsidence velocity

$\overline{w'\theta'_l}$ Mean turbulent flux for liquid potential temperature

$\overline{w'\theta'_v}$ Mean turbulent flux for virtual potential temperature

z_b Cloud base height

z_i Inversion height

D Subsidence divergence

g Gravitational acceleration

t Time

This chapter contains material from B. Ozge Akyurek, Jan Kleissl, "Closed-Form Analytic Solution of Cloud Dissipation for a Mixed-Layer Model", AMS Journal of Atmospheric Sciences 2017. The dissertation author was the primary investigator and author of this paper.

Chapter 2

Mixed-Layer Model for Stratocumulus Clouds

2.1 Background

In this section, we define the models that approximate the physical processes. Consider a well mixed single vertical column with a single cloud layer bounded by its base height, z_{b}, and the inversion height, z_{i}. An illustration is shown in Figure 2.1. We assume constant air density ρ_{air} and constant values for the jumps at the inversion layer for total water mixing ratio, $\Delta q_{\mathrm{T,\,i}}$, and liquid potential temperature, $\Delta\theta_{\mathrm{l,\,i}}$, ([19]).

The cloud thickness h is the primary parameter of interest and its tendency can be defined as:

$$\frac{dh(t)}{dt} = \frac{dz_{\mathrm{i}}(t)}{dt} - \frac{dz_{\mathrm{b}}(t)}{dt} \tag{2.1}$$

We use the inversion tendency definition from [25] and [32], where the inversion height changes with the entrainment parameter, w_{e} and the subsidence, $w_{\mathrm{s}}(z_{\mathrm{i}})$. Subsidence is further approximated by a constant divergence within the BL, denoted by D ([25]):

$$\frac{dz_{\mathrm{i}}}{d_t} = w_{\mathrm{e}}(t) + \mathbf{v}_{\mathrm{H}} \cdot \nabla z_{\mathrm{i}} = w_{\mathrm{e}}(t) + w_{\mathrm{s}}(z_{\mathrm{i}}) = w_{\mathrm{e}}(t) + Dz_{\mathrm{i}}(t) \tag{2.2}$$

The cloud base height tendency expression ([33]) depends on the conserved

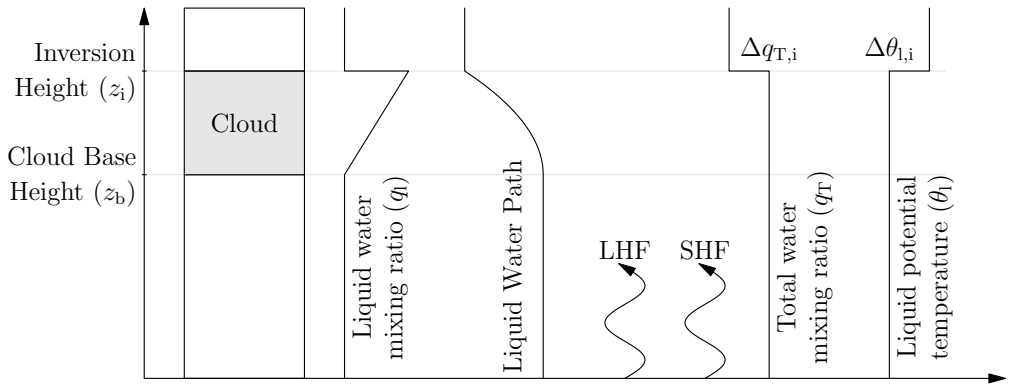

Figure 2.1: System Model and Simulation domain. The system is modeled as a single well-mixed air column. The stratocumulus cloud layer (gray) is bounded by the temperature inversion and cloud base. The liquid water content q_l linearly increases with height in the cloud layer and the resulting liquid water path is shown. The surface boundary conditions of latent (LHF) and sensible heat fluxes (SHF) are also shown.

variables of liquid potential temperature, θ_l and total moisture, q_T:

$$\frac{dz_b(t)}{dt} = \frac{R_d T_{base}}{g q_T(t)} \left(1 - \frac{L_v R_d}{c_p R_v T_{base}}\right)^{-1} \frac{dq_T(t)}{dt} + \frac{c_p \pi_{base}}{g} \left(1 - \frac{c_p R_v T_{base}}{R_d L_v}\right)^{-1} \frac{d\theta_l(t)}{dt} \tag{2.3}$$

R_d and R_v represent the gas constants for dry air and water vapor, respectively, L_v is the latent heat of evaporation, c_p is the specific heat, g is the gravitational acceleration, T_{base} is the temperature at the cloud base, π_{base} is the Exner function evaluated at the cloud base. In the following sections the inversion height and cloud base height tendencies are derived based on the budget equations for heat and moisture.

2.2 Budget Equations for Conserved Moisture and Temperature Variables

The MLM budget conservation equations are given for the liquid potential temperature and the total moisture as ([19]):

$$\frac{d\theta_{\mathrm{l}}(t)}{dt} = -\frac{\partial}{\partial z}\left(\overline{\mathrm{w}'\theta_{\mathrm{l}}'}(z,t) + \frac{\mathrm{F}_{\mathrm{rad}}(z,t)}{\mathrm{c_p}\rho_{\mathrm{air}}}\right) - \theta_{\mathrm{l,\ adv}} \tag{2.4}$$

$$\frac{dq_{\mathrm{T}}(t)}{dt} = -\frac{\partial \overline{\mathrm{w}'q_{\mathrm{T}}'}(z,t)}{\partial z} - q_{\mathrm{T,\ adv}} \tag{2.5}$$

The large scale advection values of total moisture $q_{\mathrm{T,\ adv}}$ and liquid potential temperature $\theta_{\mathrm{l,\ adv}}$ are assumed to be zero throughout this chapter. While advection effects are important for the MBL over coastal lands, the advection terms complicate the integration of the equations and are left for future study. $\overline{\mathrm{w}'\theta_{\mathrm{l}}'}(z,t)$ and $\overline{\mathrm{w}'q_{\mathrm{T}}'}(z,t)$ represent the average liquid potential temperature flux and average total moisture flux, respectively. $\mathrm{F}_{\mathrm{rad}}$ represents the net radiation flux. Due to the well-mixed assumption, both conserved variables can be assumed to be independent of height. This forces the right hand side of the equations to be also independent of height, resulting in a linear height dependency for the partial derivatives. Representing the partial derivatives as E and W, respectively, we can derive the full expressions using the boundary conditions at $z = 0$ and $z = z_{\mathrm{i}}$, as given in [20]:

$$\frac{d\theta_{\mathrm{l}}}{dt} = -\frac{\partial E}{\partial z} \tag{2.6}$$

$$\frac{dq_{\mathrm{T}}}{dt} = -\frac{\partial W}{\partial z} \tag{2.7}$$

$$E(z) = (1 - z/z_{\mathrm{i}})E(0) + (z/z_{\mathrm{i}})E(z_{\mathrm{i}}) \tag{2.8}$$

$$W(z) = (1 - z/z_{\mathrm{i}})W(0) + (z/z_{\mathrm{i}})W(z_{\mathrm{i}}) \tag{2.9}$$

The boundary conditions at the surface and inversion height are obtained as:

$$E(0) = \overline{\mathrm{w}'\theta_{\mathrm{l}}'}(0,t) + \mathrm{F}_{\mathrm{rad}}(0,t)/(\rho_{\mathrm{air}}\mathrm{c_p}) \tag{2.10}$$

$$E(z_{\mathrm{i}}) = -w_{\mathrm{e}}\Delta\theta_{\mathrm{l,\ i}} + \mathrm{F}_{\mathrm{rad}}(z_{\mathrm{i}},t)/(\rho_{\mathrm{air}}\mathrm{c_p}) \tag{2.11}$$

$$W(0) = \overline{\mathrm{w}'q_{\mathrm{T}}'}(0,t) \tag{2.12}$$

$$W(z_{\mathrm{i}}) = -w_{\mathrm{e}}\Delta q_{\mathrm{T,\ i}} \tag{2.13}$$

The final expressions for θ_{l} and q_{T} tendencies are obtained as:

$$\frac{d\theta_{\mathrm{l}}(t)}{dt} = \frac{\overline{\mathrm{w}'\theta_{\mathrm{l}}'}(0,t)}{z_{\mathrm{i}}(t)} + \frac{\mathrm{F}_{\mathrm{rad}}(0,t)}{\rho_{\mathrm{air}}\mathrm{c_p}z_{\mathrm{i}}(t)} + \frac{w_{\mathrm{e}}(t)\Delta\theta_{\mathrm{l,\,i}}}{z_{\mathrm{i}}(t)} - \frac{\mathrm{F}_{\mathrm{rad}}(z_{\mathrm{i}}(t),t)}{\rho_{\mathrm{air}}\mathrm{c_p}z_{\mathrm{i}}(t)} \tag{2.14}$$

$$\frac{dq_{\mathrm{T}}(t)}{dt} = \frac{\overline{\mathrm{w}'q_{\mathrm{T}}'}}{z_{\mathrm{i}}(t)} + \frac{w_{\mathrm{e}}(t)\Delta q_{\mathrm{T,\,i}}}{z_{\mathrm{i}}(t)} \tag{2.15}$$

2.3 Radiation Model

In this section we derive equations for the components of the net radiation flux and their attenuation through the cloud layer. Net radiation flux is decomposed into net longwave and net shortwave components:

$$\mathrm{F}_{\mathrm{rad}}(z,t) = \mathrm{F}_{\mathrm{lw}}(z,t) - \mathrm{F}_{\mathrm{sw}}(z,t) \tag{2.16}$$

2.3.1 Liquid Water Path and Optical Depth

Both radiation terms are attenuated by an optical depth term designated as τ. This term depends on the total columnar liquid water content. We assume that the liquid water mixing ratio q_{l} within the cloud increases linearly with height proportional to a constant Γ_l, which can be calculated from thermodynamics or observations:

$$q_{\mathrm{l}}(z,t) = \begin{cases} \Gamma_l(z - z_{\mathrm{b}}(t)), & z_{\mathrm{b}}(t) \le z \le z_{\mathrm{i}}(t) \\ 0, & \text{otherwise} \end{cases} \tag{2.17}$$

The liquid water path (LWP) is defined as:

$$\mathrm{LWP}(z,t) = \int_{z'=z}^{z_{\mathrm{i}}(t)} \rho_{\mathrm{air}} q_{\mathrm{l}}(z',t)dz' \tag{2.18}$$

Using this definition, LWP then becomes:

$$\mathrm{LWP}(z,t) = \begin{cases} 0, & z > z_{\mathrm{i}}(t) \\ \rho_{\mathrm{air}}\Gamma_l\left((z_{\mathrm{i}}(t) - z_{\mathrm{b}}(t))^2 - (z - z_{\mathrm{b}}(t))^2\right)/2, & z_{\mathrm{b}}(t) \le z \le z_{\mathrm{i}}(t) \\ \rho_{\mathrm{air}}\Gamma_l\left(z_{\mathrm{i}}(t) - z_{\mathrm{b}}(t)\right)^2/2, & z < z_{\mathrm{b}}(t) \end{cases} \tag{2.19}$$

The optical depth τ is defined with respect to the optical depth at the cloud top which is assumed to be zero. τ_{b} is the optical depth at and below the cloud base:

$$\tau(z,t) = \begin{cases} 0, & z > z_{\mathrm{i}}(t) \\ \dfrac{3\rho_{\mathrm{air}}\mathrm{LWP}}{2\mathrm{R_e}\rho_{\mathrm{W}}} = \dfrac{3\rho_{\mathrm{air}}\Gamma_l\left(h(t)^2 - (z - z_{\mathrm{b}}(t))^2\right)}{4\mathrm{R_e}\rho_{\mathrm{W}}}, & z_{\mathrm{b}}(t) \le z \le z_{\mathrm{i}}(t) \\ \tau_{\mathrm{b}}(t) \triangleq \dfrac{3\rho_{\mathrm{air}}\Gamma_l h^2}{4\mathrm{R_e}\rho_{\mathrm{W}}}, & z < z_{\mathrm{b}}(t) \end{cases} \quad (2.20)$$

ρ_{W} is the density of water and $\mathrm{R_e}$ is the effective droplet radius.

2.3.2 Longwave Radiation

For the longwave radiation, we utilize the model in [26] which assumes isothermal blackbody radiation and single scattering. The net radiative longwave flux is defined as:

$$\mathrm{F_{lw}}(z,t) = \mathrm{L_{lw}}(t)e^{\alpha_{\mathrm{lw}}\tau(z,t)} + \mathrm{M_{lw}}(t)e^{-\alpha_{\mathrm{lw}}\tau(z,t)} \quad (2.21)$$

α_{lw} represents the optical depth scale for longwave radiation. The coefficients L and M are obtained by solving the second order radiation differential equation in [34]:

$$\begin{aligned} \mathrm{L_{lw}}(t) &= \gamma(t)\left[(\mathrm{B_{cld}}(t) - \mathrm{B_{sky}}(t))\mathrm{c_{1,\,lw}}e^{-\alpha_{\mathrm{lw}}\tau_{\mathrm{b}}(t)}\right. \\ &+ \left.(\mathrm{B_{srf}}(t) - \mathrm{B_{cld}}(t))\mathrm{c_{2,\,lw}}\right] \quad (2.22) \\ \mathrm{M_{lw}}(t) &= \gamma(t)\left[(\mathrm{B_{cld}}(t) - \mathrm{B_{sky}}(t))\mathrm{c_{2,\,lw}}e^{\alpha_{\mathrm{lw}}\tau_{\mathrm{b}}(t)}\right. \\ &+ \left.(\mathrm{B_{srf}}(t) - \mathrm{B_{cld}}(t))\mathrm{c_{1,\,lw}}\right] \quad (2.23) \end{aligned}$$

The coefficients are defined as:

$$\begin{aligned} \gamma(t) &= \frac{-4\pi(1-\omega_{\mathrm{lw}})}{\mathrm{c}^2_{1,\,\mathrm{lw}}e^{-\alpha_{\mathrm{lw}}\tau_{\mathrm{b}}(t)} - \mathrm{c}^2_{2,\,\mathrm{lw}}e^{\alpha_{\mathrm{lw}}\tau_{\mathrm{b}}(t)}} \quad (2.24) \\ \mathrm{c_{1,\,lw}} &= \alpha_{\mathrm{lw}} - 2(1-\omega_{\mathrm{lw}}) \quad (2.25) \\ \mathrm{c_{2,\,lw}} &= \alpha_{\mathrm{lw}} + 2(1-\omega_{\mathrm{lw}}) \quad (2.26) \\ \alpha_{\mathrm{lw}} &= \sqrt{3(1-\omega_{\mathrm{lw}})(1-\omega_{\mathrm{lw}}\mathrm{g_{lw}})} \quad (2.27) \end{aligned}$$

ω_{lw} designates the single scattering albedo and $\mathrm{g_{lw}}$ is the asymmetry factor. The $\mathrm{B_{cld}}, \mathrm{B_{sky}}$ and $\mathrm{B_{srf}}$ terms are blackbody radiation arising from $\mathrm{T_{cld}}$, $\mathrm{T_{sky}}$ and $\mathrm{T_{srf}}$.

$$\mathrm{B_{cld}}(t) = \frac{\sigma}{\pi}\mathrm{T_{cld}}(t)^4, \qquad \mathrm{B_{sky}}(t) = \frac{\sigma}{\pi}\mathrm{T_{sky}}(t)^4, \qquad \mathrm{B_{srf}}(t) = \frac{\sigma}{\pi}\mathrm{T_{srf}}(t)^4 \tag{2.28}$$

$\mathrm{T_{cld}}$ represents the effective radiative temperature of the cloud and is downwelling at the cloud base and upwelling at the cloud top. $\mathrm{T_{srf}}$ designates the effective radiative temperature of the ground surface, modeled as a black body and is upwelling. $\mathrm{T_{sky}}$ is the effective downwelling radiative temperature of the column above the cloud top, modeled as a black body.

2.3.3 Shortwave Radiation

We utilize the Delta-Eddington approximation in [32] and [35] as shortwave radiation model. Using the Eddington approximation, the diffuse radiance can be divided into a linear combination of a term independent of the solar zenith angle (θ_0) and a solar zenith angle dependent term, yielding the analytic solution for the net shortwave radiation flux as:

$$\mathrm{F_{sw}}(z,t) = F_0\mu_0(t)\left(\frac{4p}{3}\mathrm{L_{sw}}(t)e^{k\tau(z,t)} + \frac{4p}{3}\mathrm{M_{sw}}(t)e^{-k\tau(z,t)} + e^{-\tau(z,t)/\mu_0(t)}(1-\frac{4}{3}\beta_{sw}(t))\right) \tag{2.29}$$

ω_{sw} designates the single scattering albedo for shortwave radiation, $\mathrm{g_{sw}}$ is the asymmetry factor, $\mu_0 = \cos(\theta_0)$, A is the surface albedo and k is the optical depth scale for shortwave radiation. Note that the incoming downward shortwave radiation F_0 is different from the net shortwave radiation at the cloud top ($F_{sw}(z_i,t)$) as the net radiation includes radiation reflected from clouds and/or the ground surface.

The coefficients are:

$$\beta_{\rm sw}(t) = 3\omega_{\rm sw}\frac{1+3{\rm g}_{\rm sw}(1-\omega_{\rm sw})\mu_0(t)^2}{4(1-k^2\mu_0(t)^2)} \tag{2.30}$$

$$\begin{aligned}{\rm L}_{\rm sw}(t) &= \frac{e^{-k\tau_{\rm b}(t)}\left(\alpha_{\rm sw}+2\beta_{\rm sw}/3\right){\rm m}_1}{e^{k\tau_{\rm b}(t)}{\rm m}_2(1+2p/3)-e^{-k\tau_{\rm b}(t)}{\rm m}_1(1-2p/3)}\\ &- \frac{(1+2p/3)e^{-\tau_{\rm b}(t)/\mu_0(t)}\left(A(\alpha_{\rm sw}+2\beta_{\rm sw}/3-1)\right)}{e^{k\tau_{\rm b}(t)}{\rm m}_2(1+2p/3)-e^{-k\tau_{\rm b}(t)}{\rm m}_1(1-2p/3)}\\ &+ \frac{(1+2p/3)e^{-\tau_{\rm b}(t)/\mu_0(t)}\left(\alpha_{\rm sw}-2\beta_{\rm sw}/3\right)}{e^{k\tau_{\rm b}(t)}{\rm m}_2(1+2p/3)-e^{-k\tau_{\rm b}(t)}{\rm m}_1(1-2p/3)}\end{aligned} \tag{2.31}$$

$$\begin{aligned}{\rm M}_{\rm sw}(t) &= \frac{e^{k\tau_{\rm b}(t)}\left(\alpha_{\rm sw}+2\beta_{\rm sw}/3\right){\rm m}_2}{e^{k\tau_{\rm b}(t)}{\rm m}_2(1+2p/3)-e^{-k\tau_{\rm b}(t)}{\rm m}_1(1-2p/3)}\\ &- \frac{(1-2p/3)e^{-\tau_{\rm b}(t)/\mu_0(t)}\left(A(\alpha_{\rm sw}+2\beta_{\rm sw}/3-1)\right)}{e^{k\tau_{\rm b}(t)}{\rm m}_2(1+2p/3)-e^{-k\tau_{\rm b}(t)}{\rm m}_1(1-2p/3)}\\ &+ \frac{(1-2p/3)e^{-\tau_{\rm b}(t)/\mu_0(t)}\left(\alpha_{\rm sw}-2\beta_{\rm sw}/3\right)}{e^{k\tau_{\rm b}(t)}{\rm m}_2(1+2p/3)-e^{-k\tau_{\rm b}(t)}{\rm m}_1(1-2p/3)}\end{aligned} \tag{2.32}$$

$${\rm m}_1 = A(1+2p/3)-(1-2p/3) \tag{2.33}$$

$${\rm m}_2 = A(1-2p/3)-(1+2p/3) \tag{2.34}$$

$$k = \sqrt{3(1-\omega_{\rm sw})(1-\omega_{\rm sw}{\rm g}_{\rm sw})} \tag{2.35}$$

$$p = \sqrt{\frac{3(1-\omega_{\rm sw})}{1-\omega_{\rm sw}{\rm g}_{\rm sw}}} \tag{2.36}$$

$$\alpha_{\rm sw}(t) = 3\omega_{\rm sw}\mu_0(t)\frac{1+{\rm g}_{\rm sw}(1-\omega_{\rm sw})}{4(1-k^2\mu_0(t)^2)} \tag{2.37}$$

2.4 Boundary Conditions

To close the system of budget equations the boundary conditions at the ground surface and inversion are needed. Entrainment at the top can be expressed as a function of the virtual potential temperature flux, $\overline{w'\theta'_{\rm v}}$, through a convective velocity scale w^* defined as in [36], [25] and [37]:

$${w^*}^3 = \frac{2.5g}{\theta_{\rm v,\,0}}\int_{z=0}^{z=z_{\rm i}}\overline{w'\theta'_{\rm v}}(z,t)dz, \qquad w_{\rm e}(t) = w^*\frac{{\rm A_w}}{\rm Ri}, \qquad {\rm Ri} = \frac{gz_{\rm i}\Delta\theta_{\rm v,\,i}}{\theta_{\rm v,\,0}{w^*}^2} \tag{2.38}$$

${\rm A_w}$ is a tuning parameter, $\theta_{\rm v,\,0}$ is a reference virtual potential temperature and Ri is the Richardson number. Combining the velocity scale equations and the

Richardson number, we obtain:

$$w_{\mathrm{e}}(t) = \frac{2.5\mathrm{A_w}}{z_{\mathrm{i}}(t)\Delta\theta_{\mathrm{v,\ i}}} \int_{z=0}^{z_{\mathrm{i}}(t)} \overline{w'\theta'_{\mathrm{v}}}(z,t)dz \tag{2.39}$$

Finally, we need the surface boundary conditions to close the system of equations. Surface fluxes of heat and water are connected to the net surface radiation through surface flux efficiency, α_{srf} and the Bowen Ratio, β as ([30]):

$$\mathrm{SHF}(t) = \overline{\mathrm{w}'\theta'_{\mathrm{l}}}(0,t)\mathrm{c_p}\rho_{\mathrm{air}} = -\alpha_{\mathrm{srf}}\left(\frac{\beta}{\beta+1}\right)\mathrm{F_{rad}}(0,t) \tag{2.40}$$

$$\mathrm{LHF}(t) = \overline{\mathrm{w}'q'_{\mathrm{T}}}(0,t)\mathrm{L_v}\rho_{\mathrm{air}} = -\alpha_{\mathrm{srf}}\left(\frac{1}{\beta+1}\right)\mathrm{F_{rad}}(0,t) \tag{2.41}$$

$\alpha_{\mathrm{srf}} = 0.88$ is applied in all simulations while Bowen Ratio is also constant for a particular simulation, but will vary from simulation to simulation to investigate effects of soil moisture content.

The radiation and surface models used in this dissertation are similar as in [30], who use numerical time-stepping to solve a similar single-column mixed layer model. Even though the authors show that the MLM results are close to a more complex simulation method (LES), the underlying connections and interdependencies between the cloud variables and the initial conditions are not analyzed. Such an analysis using numerical solution techniques is impractical due to the vast number of variables in the solution space as shown in Figure 2.2, motivating our analytic solution to this problem.

Interdependencies of atmospheric variables are abundant as illustrated in Figure 2.2 through a automatically generated dependency graph.

This chapter contains material from B. Ozge Akyurek, Jan Kleissl, "Closed-Form Analytic Solution of Cloud Dissipation for a Mixed-Layer Model", AMS Journal of Atmospheric Sciences 2017. The dissertation author was the primary investigator and author of this paper.

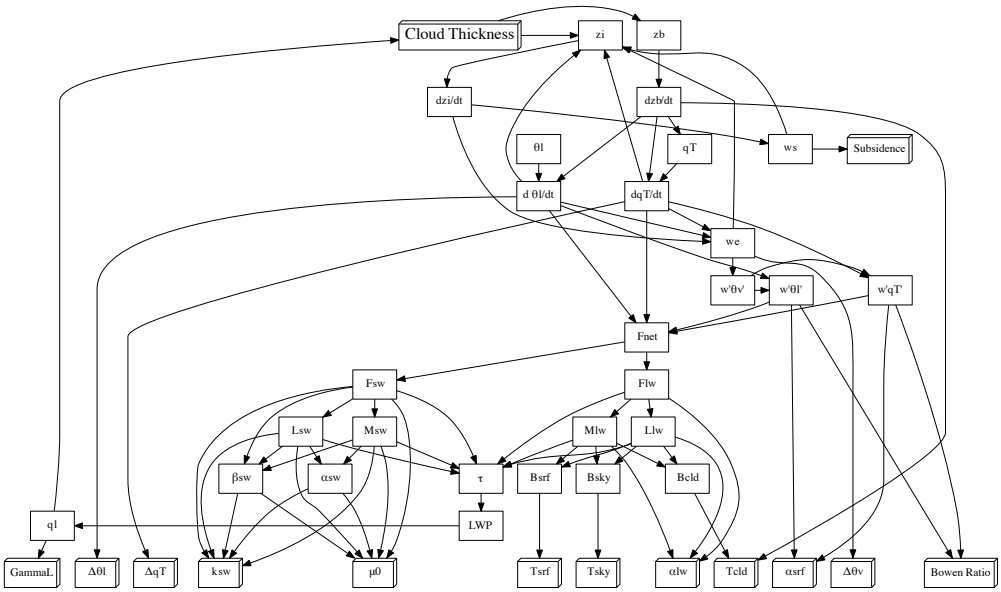

Figure 2.2: Dependency graph for all variables in the system. An arrow between two variables indicates a dependency, where the source of the arrow *depends* on the end of it, e.g. Cloud thickness depends on inversion height.

Chapter 3

Closed-Form Analytic Solution for a Mixed-Layer Model

3.1 Analytic Closed-Form Solution

3.1.1 Inversion Height Tendency

The objective of this section is to obtain a closed form solution for Eq. (2.2). This requires the entrainment velocity in Eq. (2.39) which depends on the virtual potential temperature flux $\overline{w'\theta'_{\mathrm{v}}}(z,t)$. The virtual potential temperature flux depends on the surface heat fluxes as ([20]):

$$\overline{w'\theta'_{\mathrm{v}}}(z,t) = c_{1,3}\overline{\mathrm{w'}\theta'_{\mathrm{l}}}(z,t) + c_{2,4}\overline{\mathrm{w'}q'_{\mathrm{T}}}(z,t) \tag{3.1}$$

From the surface to the cloud base height the coefficients $c_{1,3} = c_1$ and $c_{2,4} = c_2$ are used. For the cloud layer, spanning from the cloud base height to the inversion height, $c_{1,3} = c_3$ and $c_{2,4} = c_4$ ([20]).

We start by scaling Eq. (2.14) and Eq. (2.15) by $c_{1,3}$ and $c_{2,4}$, respectively and summing them up:

$$\begin{aligned} c_{1,3}\frac{d\theta_{\mathrm{l}}}{dt} + c_{2,4}\frac{dq_{\mathrm{T}}}{dt} &= \frac{\overline{w'\theta'_{\mathrm{v}}}(0,t) + c_3 w_{\mathrm{e}}(t)\Delta\theta_{\mathrm{l,\,i}} + c_4 w_{\mathrm{e}}(t)\Delta q_{\mathrm{T,\,i}}}{z_{\mathrm{i}}(t)} \\ &+ \frac{c_1 \mathrm{F_{rad}}(0,t) - c_3 \mathrm{F_{rad}}(z_{\mathrm{i}},t)}{\rho_{\mathrm{air}} \mathrm{c_p} z_{\mathrm{i}}(t)} \end{aligned} \tag{3.2}$$

The left hand side can also be expressed using Eq. (2.4):

$$\begin{aligned} c_{1,3}\frac{d\theta_{\mathrm{l}}}{dt} + c_{2,4}\frac{dq_{\mathrm{T}}}{dt} &= -c_{1,3}\frac{\partial}{\partial z}\left(\overline{\mathrm{w}'\theta'_{\mathrm{l}}}(z,t) + \frac{\mathrm{F}_{\mathrm{rad}}(z,t)}{\mathrm{c_p}\rho_{\mathrm{air}}}\right) - c_{2,4}\frac{\partial\overline{\mathrm{w}'q'_{\mathrm{T}}}(z,t)}{\partial z} \\ &= -c_{1,3}\frac{\partial}{\partial z}\left(\frac{\mathrm{F}_{\mathrm{rad}}(z,t)}{\mathrm{c_p}\rho_{\mathrm{air}}}\right) - \frac{\partial\overline{w'\theta'_{\mathrm{v}}}(z,t)}{\partial z} \end{aligned} \tag{3.3}$$

Eq. (3.2) and Eq. (3.3) are equal to each other. We use the fact that the left side of both Eq. (3.2) and Eq. (3.3) are independent of z due to the well mixed assumption, to take the integral of both equations from $z = 0$ to an arbitrary z. Leaving the virtual potential temperature flux on the left side of the equation, the expression becomes:

$$\begin{aligned} \overline{w'\theta'_{\mathrm{v}}}(z,t) &= c_1\frac{\mathrm{F}_{\mathrm{rad}}(0,t)}{\mathrm{c_p}\rho_{\mathrm{air}}} - c_{1,3}\frac{\mathrm{F}_{\mathrm{rad}}(z,t)}{\mathrm{c_p}\rho_{\mathrm{air}}} + \overline{w'\theta'_{\mathrm{v}}}(0,t) \\ &+ \frac{z}{z_{\mathrm{i}}(t)}\left(\frac{c_3\mathrm{F}_{\mathrm{rad}}(z_{\mathrm{i}},t) - c_1\mathrm{F}_{\mathrm{rad}}(0,t)}{\rho_{\mathrm{air}}\mathrm{c_p}} - \overline{w'\theta'_{\mathrm{v}}}(0,t)\right) \\ &- \frac{z}{z_{\mathrm{i}}(t)}\left(w_{\mathrm{e}}(t)(c_3\Delta\theta_{\mathrm{l,\,i}} + c_4\Delta q_{\mathrm{T,\,i}})\right) \end{aligned} \tag{3.4}$$

Utilizing the same scaling operation as in Eq. (3.2) for the surface flux definitions from Eq. (2.41) and Eq. (2.40):

$$\begin{aligned} \frac{c_1}{\mathrm{c_p}\rho_{\mathrm{air}}}\mathrm{SHF} + \frac{c_2}{\mathrm{L_v}\rho_{\mathrm{air}}}\mathrm{LHF} &= c_1\overline{\mathrm{w}'\theta'_{\mathrm{l}}}(0,t) + c_2\overline{\mathrm{w}'q'_{\mathrm{T}}}(0,t) = \overline{w'\theta'_{\mathrm{v}}}(0,t) \\ &= -\frac{\mathrm{F}_{\mathrm{rad}}(0,t)}{\beta+1}\left(\frac{\alpha_{\mathrm{srf}}\beta c_1}{\mathrm{c_p}\rho_{\mathrm{air}}} + \frac{c_2\alpha_{\mathrm{srf}}}{\rho_{\mathrm{air}}\mathrm{L_v}}\right) \end{aligned} \tag{3.5}$$

Substituting Eq. (3.5) into Eq. (3.4), we obtain:

$$\begin{aligned} &\overline{w'\theta'_{\mathrm{v}}}(z,t) = \frac{\mathrm{F}_{\mathrm{rad}}(0,t)}{\mathrm{c_p}\rho_{\mathrm{air}}}\left(c_1 - \frac{\alpha_{\mathrm{srf}}\beta c_1}{\beta+1} - \frac{c_2\alpha_{\mathrm{srf}}\mathrm{c_p}}{\mathrm{L_v}(\beta+1)}\right) - c_{1,3}\frac{\mathrm{F}_{\mathrm{rad}}(z,t)}{\mathrm{c_p}\rho_{\mathrm{air}}} \\ &+\frac{z}{z_{\mathrm{i}}(t)}\left(\frac{c_3\mathrm{F}_{\mathrm{rad}}(z_{\mathrm{i}},t)}{\rho_{\mathrm{air}}\mathrm{c_p}} - \frac{\mathrm{F}_{\mathrm{rad}}(0,t)}{\rho_{\mathrm{air}}\mathrm{c_p}}\left(c_1 - \frac{\alpha_{\mathrm{srf}}\beta c_1}{\beta+1} - \frac{c_2\alpha_{\mathrm{srf}}\mathrm{c_p}}{\mathrm{L_v}(\beta+1)}\right)\right) \\ &-\frac{z}{z_{\mathrm{i}}(t)}\left(w_{\mathrm{e}}(t)(c_3\Delta\theta_{\mathrm{l,\,i}} + c_4\Delta q_{\mathrm{T,\,i}})\right) \end{aligned} \tag{3.6}$$

Next, we integrate $\overline{w'\theta'_{\mathrm{v}}}(z,t)$ over the boundary layer depth to obtain the

entrainment velocity w_{e} in Eq. (2.39):

$$\begin{aligned} w_{\mathrm{e}}(t) &= \frac{2.5\mathrm{A_w}}{z_{\mathrm{i}}\Delta\theta_{\mathrm{v,\,i}}}\int_{z=0}^{z=z_{\mathrm{i}}}\left(1-\frac{z}{z_{\mathrm{i}}}\right)\mathrm{F_{rad}}(0,t)\left(\frac{c_1}{\mathrm{c_p}\rho_{\mathrm{air}}}\right)dz \\ &- \frac{2.5\mathrm{A_w}}{z_{\mathrm{i}}\Delta\theta_{\mathrm{v,\,i}}}\int_{z=0}^{z=z_{\mathrm{i}}}\left(1-\frac{z}{z_{\mathrm{i}}}\right)\mathrm{F_{rad}}(0,t)\left(\frac{\alpha_{\mathrm{srf}}\beta c_1}{\mathrm{c_p}\rho_{\mathrm{air}}(\beta+1)}+\frac{c_2\alpha_{\mathrm{srf}}}{\rho_{\mathrm{air}}\mathrm{L_v}(\beta+1)}\right)dz \\ &- \frac{2.5\mathrm{A_w}}{z_{\mathrm{i}}\Delta\theta_{\mathrm{v,\,i}}}\int_{z=0}^{z=z_{\mathrm{i}}}\frac{c_{1,3}}{\mathrm{c_p}\rho_{\mathrm{air}}}\mathrm{F_{rad}}(z,t)dz \\ &+ \frac{2.5\mathrm{A_w}}{z_{\mathrm{i}}\Delta\theta_{\mathrm{v,\,i}}}\int_{z=0}^{z=z_{\mathrm{i}}}\frac{z}{z_{\mathrm{i}}}\left(\frac{c_3\mathrm{F_{rad}}(z_{\mathrm{i}},t)}{\mathrm{c_p}\rho_{\mathrm{air}}}-w_{\mathrm{e}}\left(c_3\Delta\theta_{\mathrm{l,\,i}}+c_4\Delta q_{\mathrm{T,\,i}}\right)\right)dz \end{aligned} \tag{3.7}$$

Combining all w_{e} terms on the left side, we obtain:

$$\begin{aligned} w_{\mathrm{e}}(t)\left(\frac{0.8\Delta\theta_{\mathrm{v,\,i}}}{\mathrm{A_w}}+c_3\Delta\theta_{\mathrm{l,\,i}}+c_4\Delta q_{\mathrm{T,\,i}}\right) &= \mathrm{F_{rad}}(0,t)\left(\frac{c_1}{\mathrm{c_p}\rho_{\mathrm{air}}}\right) \\ &-\mathrm{F_{rad}}(0,t)\left(\frac{\alpha_{\mathrm{srf}}\beta c_1}{\mathrm{c_p}\rho_{\mathrm{air}}(\beta+1)}+\frac{c_2\alpha_{\mathrm{srf}}}{\rho_{\mathrm{air}}\mathrm{L_v}(\beta+1)}\right) \\ &+\frac{c_3}{\mathrm{c_p}\rho_{\mathrm{air}}}\mathrm{F_{rad}}(z_{\mathrm{i}},t)-\frac{2}{z_{\mathrm{i}}\mathrm{c_p}\rho_{\mathrm{air}}}\int_{z=0}^{z=z_{\mathrm{i}}}c_{1,3}\mathrm{F_{rad}}(z,t)dz \end{aligned} \tag{3.8}$$

Substituting this result in Eq. (2.2) we obtain the inversion height tendency:

$$\frac{dz_{\mathrm{i}}(t)}{dt}-Dz_{\mathrm{i}}=\zeta_1\mathrm{F_{rad}}(0,t)+\zeta_2\mathrm{F_{rad}}(z_{\mathrm{i}},t)+\frac{\zeta_3}{z_{\mathrm{i}}}\int_{z=0}^{z=z_{\mathrm{i}}}c_{1,3}\mathrm{F_{rad}}(z,t)dz \tag{3.9}$$

where ζ coefficients are employed to simplify the equation. This is a nonlinear differential equation. Each net radiation term depends on the cloud thickness through the optical depth term. Furthermore, the columnar integral of the net radiation is called a Dawson function and is not an analytic function. Thus, an analytic solution requires approximations as explained in Section 3.1.3.

3.1.2 Cloud Thickness Tendency

In addition to the inversion height tendency the cloud thickness tendency requires the cloud base height tendency. The solution strategy is to manipulate

Eq. (2.3) into simpler variables analogous to the derivation of the inversion height tendency. The total moisture and liquid potential temperature tendencies appear in Eq. (2.3), but their tendencies given in Eq. (2.14) and Eq. (2.15), depend on z_{i}^{-1}. Since inversion height is a complex expression itself, it would be difficult to solve the tendencies in their current form. To simplify the inversion height dependency, we multiply both differential equations by z_{i} and add $\theta_{\mathrm{l}}\frac{dz_{\mathrm{i}}}{dt}$ and $q_{\mathrm{T}}\frac{dz_{\mathrm{i}}}{dt}$, respectively, so that the resulting expressions are the derivatives of the product of the conserved variables with the inversion height:

$$\begin{aligned}\frac{d\left(\theta_{\mathrm{l}}(t)z_{\mathrm{i}}(t)\right)}{dt} &= \overline{\mathrm{w}'\theta_{\mathrm{l}}'}(0,t) + \frac{\mathrm{F}_{\mathrm{rad}}(0,t)}{\rho_{\mathrm{air}}\mathrm{c_p}} + w_{\mathrm{e}}(t)\theta_{\mathrm{l,\ inv}} - w_{\mathrm{e}}(t)\theta_{\mathrm{l}}(t) \\ &- \frac{\mathrm{F}_{\mathrm{rad}}(z_{\mathrm{i}}(t),t)}{\rho_{\mathrm{air}}\mathrm{c_p}} + \theta_{\mathrm{l}}(t)\frac{dz_{\mathrm{i}}}{dt} \end{aligned} \tag{3.10}$$

$$\frac{d\left(q_{\mathrm{T}}(t)z_{\mathrm{i}}(t)\right)}{dt} = \overline{\mathrm{w}'q_{\mathrm{T}}'}(0,t) + w_{\mathrm{e}}(t)q_{\mathrm{T,\ inv}} - w_{\mathrm{e}}(t)q_{\mathrm{T}}(t) + q_{\mathrm{T}}(t)\frac{dz_{\mathrm{i}}}{dt} \tag{3.11}$$

This manipulation simplifies the right side of the differential equation by eliminating the inversion height term. Only its tendency remains. Using the inversion tendency (Eq. (2.2)) and the surface fluxes (Eq. (2.40), Eq. (2.41)) we obtain:

$$\begin{aligned}\frac{d\left(\theta_{\mathrm{l}}(t)z_{\mathrm{i}}(t)\right)}{dt} - D\left(\theta_{\mathrm{l}}(t)z_{\mathrm{i}}(t)\right) &= \left(\frac{\beta+1-\alpha_{\mathrm{srf}}\beta}{\rho_{\mathrm{air}}\mathrm{c_p}(\beta+1)}\right)\mathrm{F}_{\mathrm{rad}}(0,t) \\ &- \frac{\mathrm{F}_{\mathrm{rad}}(z_{\mathrm{i}}(t),t)}{\rho_{\mathrm{air}}\mathrm{c_p}} + w_{\mathrm{e}}(t)\theta_{\mathrm{l,\ inv}}\end{aligned} \tag{3.12}$$

$$\frac{d\left(q_{\mathrm{T}}(t)z_{\mathrm{i}}(t)\right)}{dt} - D\left(q_{\mathrm{T}}(t)z_{\mathrm{i}}(t)\right) = -\frac{\alpha_{\mathrm{srf}}}{\mathrm{L_v}\rho_{\mathrm{air}}(\beta+1)}\mathrm{F}_{\mathrm{rad}}(0,t) + w_{\mathrm{e}}(t)q_{\mathrm{T,\ inv}} \tag{3.13}$$

Note that we again need the net radiation expressions as in the inversion height expression to solve these differential equations. Finally, we use the cloud thickness tendency in [33] to obtain the cloud thickness:

$$\begin{aligned}\frac{dh}{dt} &= \frac{dz_{\mathrm{i}}(t)}{dt} - \frac{\mathrm{R_d}\mathrm{T_{base}}}{gq_{\mathrm{T}}(t)}\left(1 - \frac{\mathrm{L_v}\mathrm{R_d}}{\mathrm{c_p}\mathrm{R_v}\mathrm{T_{base}}}\right)^{-1}\frac{dq_{\mathrm{T}}(t)}{dt} \\ &- \frac{\mathrm{c_p}\Pi_b}{g}\left(1 - \frac{\mathrm{c_p}\mathrm{R_v}\mathrm{T_{base}}}{\mathrm{R_d}\mathrm{L_v}}\right)^{-1}\frac{d\theta_{\mathrm{l}}(t)}{dt}\end{aligned} \tag{3.14}$$

3.1.3 Approximation of Net Radiation Flux Term

The net radiation flux appears in three forms: 1) surface $\mathrm{F_{rad}}(0,t)$, 2) inversion height $\mathrm{F_{rad}}(z_\mathrm{i}(t),t)$, and 3) columnar average $\frac{1}{z_\mathrm{i}(t)}\int_{z=0}^{z=z_\mathrm{i}(t)}\mathrm{F_{rad}}(z,t)dz$. We start with the approximations for the net longwave expressions at $z=0$ and z_i based on Eq. (2.21). Then we continue with the net shortwave expressions at $z=0$ and z_i. Finally, we approximate the columnar integral of net radiation as a linear combination of the net radiation at $z=0$ and z_i.

$$\mathrm{F_{lw}(z=0,}t) = \mathrm{L_{lw}}(t)e^{\alpha_\mathrm{lw}\tau_\mathrm{b}(t)} + \mathrm{M_{lw}}(t)e^{-\alpha_\mathrm{lw}\tau_\mathrm{b}(t)} \tag{3.15}$$

$$\mathrm{F_{lw}(z=}z_\mathrm{i},t) = \mathrm{L_{lw}}(t) + \mathrm{M_{lw}}(t) \tag{3.16}$$

We simplify these expressions by neglecting higher order (<-1) exponential optical depth terms ($\exp(-\alpha_\mathrm{lw}\tau_\mathrm{b})$) as follows:

$$\begin{aligned}\mathrm{F_{lw}(z,}t) &\simeq \frac{4\pi(1-\omega_\mathrm{lw})(\mathrm{B_{srf}}-\mathrm{B_{cld}})}{c_2} \\ &+ \frac{8\pi\alpha_\mathrm{lw}(1-\omega_\mathrm{lw})(\mathrm{B_{cld}}-\mathrm{B_{sky}})}{c_2^2}e^{-\alpha_\mathrm{lw}\tau_b}\end{aligned} \tag{3.17}$$

$$\begin{aligned}\mathrm{F_{lw}}(z_\mathrm{i}(t),t) &\simeq \frac{4\pi(1-\omega_\mathrm{lw})(\mathrm{B_{cld}}-\mathrm{B_{sky}})}{c_2} \\ &+ \frac{8\pi\alpha_\mathrm{lw}(1-\omega_\mathrm{lw})(\mathrm{B_{srf}}-\mathrm{B_{cld}})}{c_2^2}e^{-\alpha_\mathrm{lw}\tau_b}\end{aligned} \tag{3.18}$$

Even though this simplification is not required for the analytic solution, it simplifies the sensitivity analysis in Section 3.3 and the error is less than 1%. Specifics for the error estimation are provided in Section 3.4.2

To permit integration of net shortwave radiation into the cloud tendency expressions, we need to simplify solar zenith angle dependent terms, since solar zenith angle changes with time in a sinusoidal shape and complex nonlinear dependencies on μ_0 such as in Eq. (2.37) or the third exponential in Eq. (2.29) are difficult to integrate. We use the following approximations for α_sw and β_sw in Eq. (2.37) and Eq. (2.30), with less than 2% and 1% error, respectively (see Section 3.4.3).

$$\alpha_\mathrm{sw} \simeq 3\mu_0\omega_\mathrm{sw}\frac{1+\mathrm{g_{sw}}(1-\omega_\mathrm{sw})}{4}, \qquad \beta_\mathrm{sw} \simeq 3\omega_\mathrm{sw}/4 \tag{3.19}$$

To approximate the net shortwave radiation at the inversion height, we use its mathematical bounds at: clear sky, $\tau = 0$, and infinite depth, $\tau \to \infty$.

$$\mathrm{F_{sw}}(z = z_\mathrm{i}, \tau_b = 0) = F_0\mu_0(1 - A) \tag{3.20}$$

$$\mathrm{F_{sw}}(z = z_\mathrm{i}, \tau_b \to \infty) = F_0\mu_0(1 - \frac{4\beta_{sw}}{3 + 2p}) + F_0\mu_0\frac{4p\alpha_{sw}}{3 + 2p} \tag{3.21}$$

The following approximation assumes an exponential dependence of net shortwave radiation on optical depth between these limits. The error of approximation is less than 6% (see Section 3.4.3 for more details):

$$\begin{aligned} \mathrm{F_{sw}}(z = z_\mathrm{i}) \;&\simeq\; \mathrm{F_{sw}}(z = z_\mathrm{i}, \tau_\mathrm{b} \to \infty) + [\mathrm{F_{sw}}(z = z_\mathrm{i}, \tau_\mathrm{b} \to \infty) \\ &-\; \mathrm{F_{sw}}(z = z_\mathrm{i}, \tau_\mathrm{b} = 0)]\, e^{-2k\tau_\mathrm{b}} \end{aligned} \tag{3.22}$$

The net shortwave radiation at the surface is approximated in terms of the value at the inversion height scaled by a factor of attenuation depending on the optical depth, with an error of less than 7% (see Section 3.4.3):

$$\mathrm{F_{sw}}(z = 0) \simeq \mathrm{F_{sw}}(z = z_\mathrm{i})e^{-k\tau_\mathrm{b}} \tag{3.23}$$

The columnar integral of net (shortwave and longwave) radiation flux can be approximated by a linear combination of net radiation values at the surface and inversion height with an error of 6% (see Section 3.4.4):

$$\frac{1}{z_\mathrm{i}}\int_{z=0}^{z_\mathrm{i}} \mathrm{F_{rad}}(z, t)dz \simeq s_1\mathrm{F_{rad}}(z = 0) + s_2\mathrm{F_{rad}}(z = z_\mathrm{i}) \tag{3.24}$$

$$s_1 = 0.99, s_2 = 0.04 \tag{3.25}$$

3.1.4 Inversion Height Solution

Using the simplified, integrable approximations for the net radiation terms a closed-form solution for the inversion height in Eq. (3.9) can be obtained. The columnar integral expression in Eq. (3.25) is employed to write Eq. (3.9) as a

combination of net radiation terms at the surface and inversion height.

$$\frac{dz_{\mathrm{i}}(t)}{dt} - Dz_{\mathrm{i}}(t) = \psi_1(t)\mathrm{F}_{\mathrm{rad}}(0,t) + \psi_2(t)\mathrm{F}_{\mathrm{rad}}(z_{\mathrm{i}},t) \tag{3.26}$$

$$\psi_1 \triangleq \frac{\frac{c_1}{\mathrm{c_p}\rho_{\mathrm{air}}} - \frac{\alpha_{\mathrm{srf}}\beta c_1}{\mathrm{c_p}\rho_{\mathrm{air}}(\beta+1)} - \frac{c_2\alpha_{\mathrm{srf}}}{\rho_{\mathrm{air}}\mathrm{L_v}(\beta+1)} - \frac{2s_1}{\mathrm{c_p}\rho_{\mathrm{air}}}}{\frac{0.8\Delta\theta_{\mathrm{v,\,i}}}{\mathrm{A_w}} + c_3\Delta\theta_{\mathrm{l,\,i}} + c_4\Delta q_{\mathrm{T,\,i}}} \tag{3.27}$$

$$\psi_2 \triangleq \frac{\frac{c_3-2s_2}{\mathrm{c_p}\rho_{\mathrm{air}}}}{\frac{0.8\Delta\theta_{\mathrm{v,\,i}}}{\mathrm{A_w}} + c_3\Delta\theta_{\mathrm{l,\,i}} + c_4\Delta q_{\mathrm{T,\,i}}} \tag{3.28}$$

The solution strategy is to find all time dependent variables inside the net radiation expressions and then solve the differential equation. For net longwave (Eq. (2.21)) the blackbody radiations are time dependent and for net shortwave (Eq. (3.22) and (3.23)) the solar zenith angle is time dependent. Furthermore, both radiation terms depend on the optical depth exponentially and optical depth depends on the square of the cloud thickness given in Eq. (2.20). We use two approximations, which are further discussed in the following paragraphs: 1) $\mathrm{T_{srf}}$, $\mathrm{T_{cld}}$, and $\mathrm{T_{sky}}$ effective radiative temperatures are constant over a 24 hour period. As a result the blackbody radiation terms are constants. 2) The change in cloud thickness h is negligible compared to the radiation length scales. This means that the effect of change in optical depth can be ignored *only* for radiation terms resulting in constant exponential optical depth terms. The actual cloud thickness solution, $h(t)$, is not a constant and the actual time-dependent expression is presented in Section 3.1.5.

The first approximation can be supported as follows: 1) The model is only valid in overcast conditions. In overcast conditions, the daily range in surface temperature compared to the actual temperature is small, where the root mean square error (RMSE) of the constant temperature assumption is about 6%, 2) Surface and cloud radiative temperatures follow similar diurnal patterns decreasing the error of the difference of blackbody radiation differences in Eq. (2.22) and Eq. (2.23). The RMSE of a constant blackbody difference assumption is about 4%. 3) The change in surface and cloud radiative temperatures is largest near solar noon due to the peak in net shortwave irradiance at small solar zenith angle. However, at noon the net longwave radiation is only $\sim 10\%$ of the net shortwave radiation and therefore the longwave balance does not contribute significantly to the overall

net radiation. In conclusion, it is justifiable to approximate the differences in blackbody radiations as constant. To further reduce the error, rather than using the initial temperatures at midnight, the mean temperatures of the previous day are used.

For the second approximation, we need to investigate the exponential optical depth terms for net longwave ($\exp(\alpha_{\mathrm{lw}}\tau_{\mathrm{b}})$) and net shortwave ($\exp(k\tau_{\mathrm{b}})$) expressions separately. Using the optical depth expression in Eq. (2.20), the exponent of the shortwave radiation can be written in the form of: $(h(t)/h_{\mathrm{sw}})^2$, where $h_{\mathrm{sw}} \triangleq \sqrt{(4\mathrm{R_e}\rho_{\mathrm{W}})/(3\rho_{\mathrm{air}}\Gamma_l k)}$, and $h_{sw} \sim [250, 500]$ m for k taken from [35], $\mathrm{R_e}$ from [26], and for Γ_l between $[0.5, 2]\times 10^{-6}$ m^{-1}. The cloud thickness has to change on the order of h_{sw} to cause a significant change in the value of the exponent. The same notation for longwave yields the exponent in the form of: $(h(t)/h_{\mathrm{lw}})^2$ with $h_{\mathrm{lw}} = \sqrt{(4\mathrm{R_e}\rho_{\mathrm{W}})/(3\rho_{\mathrm{air}}\Gamma_l\alpha_{\mathrm{lw}})}$. $h_{\mathrm{lw}} >> h_{\mathrm{sw}}$, resulting in an even smaller exponent value than the shortwave. For a cloud thickness of 250 m, the RMSE of keeping the exponential optical depth term constant with respect to a varying numerical optical depth solution is $\sim 7\%$ as demonstrated in Section 3.4.5. The appendix also provides comparisons of daily model runs for constant and variable optical thickness under different Bowen Ratios and Γ_l values. The constant optical thickness results follows the variable optical thickness results, but differences increase for greater Γ_l and smaller Bowen Ratios. Large Γ_l result in smaller h_{sw} scales, causing larger deviation from the constant optical thickness assumption, whereas smaller Bowen Ratios delay cloud dissipation resulting in the accumulation of errors over longer time horizons.

Using both approximations, the only time dependent terms are the solar zenith angle terms, $\mu_0(t)$ and $\mu_0^2(t)$, and the inversion height tendency equation simplifies into:

$$\frac{dz_{\mathrm{i}}(t)}{dt} - Dz_{\mathrm{i}}(t) = a_1 + a_2\mu_0(t) + a_3\mu_0^2(t). \tag{3.29}$$

The solution of differential equations of type $\frac{dy}{dx} - Dy = f(x)$ is:

$$y(x) = y(0)e^{Dx} + e^{Dx}\int_{x'=0}^{x} e^{-Dx'}f(x')dx' \tag{3.30}$$

Assuming that $u_1(t)$, $u_2(t)$ and $u_3(t)$ are the solutions of

$$\frac{du_1}{dt} - Du_1 = 1, \qquad \frac{du_2}{dt} - Du_2 = \mu_0, \qquad \frac{du_3}{dt} - Du_3 = \mu_0^2 \tag{3.31}$$

we can write the inversion height as:

$$z_{\mathrm{i}}(t) = z_{\mathrm{i}}(0)e^{Dt} + a_1u_1(t) + a_2u_2(t) + a_3u_3(t) \tag{3.32}$$

We use the solar zenith angle definition of $\mu_0 = \max(\mu_1 + \mu_2\cos(t\pi/H - \pi), 0)$, where $\mu_1 = \sin(\mathrm{lat})\sin(\mathrm{dec})$, $\mu_2 = \cos(\mathrm{lat})\cos(\mathrm{dec})$, lat is the local latitude, dec is the declination and H is 12 hours. We solve for the functions u_1, u_2 and u_3 using Eq. (3.30). The equations for a single day are given below. The general forms for multiple days are more complex and provided in Section 3.5:

$$u_1(t) = \frac{e^{Dt} - 1}{D} \tag{3.33}$$

$$\begin{aligned} u_2(t) &= \mu_2\frac{\pi H^{-1}\sin(t\pi/H - \pi) - D\cos(t\pi/H - \pi)}{D^2 + \pi^2H^{-2}} \\ &+ e^{Dt-Dt_1}\frac{\pi H^{-1}\left(\sqrt{\mu_2^2 - \mu_1^2}\right) + \mu_1D^{-1}\pi^2H^{-2}}{D^2 + \pi^2H^{-2}} - \mu_1D^{-1} \end{aligned} \tag{3.34}$$

$$\begin{aligned} u_3(t) &= 2\mu_1\mu_2\frac{\pi H^{-1}\sin(t\pi/H - \pi) - D\cos(t\pi/H - \pi)}{D^2 + \pi^2H^{-2}} \\ &+ 2\mu_1e^{Dt-Dt_1}\frac{\pi H^{-1}\sqrt{\mu_2^2 - \mu_1^2} - \mu_1D}{D^2 + \pi^2H^{-2}} \\ &+ \frac{\mu_2^2}{2}\frac{2\pi H^{-1}\sin(2t\pi/H) - D\cos(2t\pi/H)}{D^2 + 4\pi^2H^{-2}} \\ &+ e^{Dt-Dt_1}\frac{\pi D(\mu_1^2 - \mu_2^2/2) - 2\mu_1\pi H^{-1}\sqrt{\mu_2^2 - \mu_1^2}}{D^2 + 4\pi^2H^{-2}} \end{aligned} \tag{3.35}$$

The unit of these functions is seconds due to the time-integration. Using these functions and the corresponding coefficients, the inversion height can be calculated for any t without numerical integrations that would be required in mixed-layer models. The functional forms as plotted in Figure 3.1 directly reveal the following. At night time, when $\mu_0 = 0$, u_2 and u_3 follow the same exponential trend as u_1 as in $\exp(Dt)$ with additional oscillatory terms, therefore u_2 and u_3 decrease during the night. u_1 also follows a negative exponential trend due to the negative sign of D. This means that the combined effect of all three functions causes

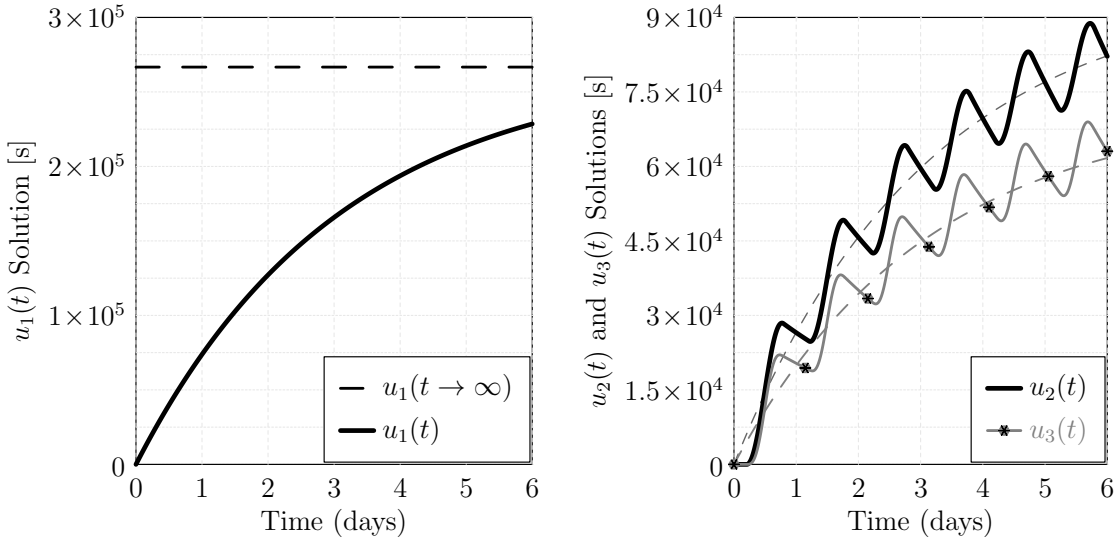

Figure 3.1: Time evolutions of the $u_1(t)$, $u_2(t)$ and $u_3(t)$ functions that constitute the inversion height solution in Eq. (3.32). For subsidence, $D = -3.75 \times 10^{-6}$ s^{-1} is used. Solar zenith angle is calculated for a latitude of 32.85° N and the 196^{th} day of the year.

the inversion height to change exponentially and the exponent is the subsidence divergence parameter, D. D is hard to determine and difficult to measure; it typically assumes values on the order of $-[10^{-6}, 10^{-5}]$ s^{-1}. During the day, u_2 and u_3 increase, dominate over u_1 and behave like a sigmoid function. The signs and magnitudes of the coefficients for the u functions also determine the trends for the cloud base height as will be shown in Section 3.3.

Since the initial condition $z_{\mathrm{i}}(0)$ is scaled by $\exp(Dt)$, the analytic solution also shows that the e-folding time for the effect of the initial condition $z_{\mathrm{i}}(0)$ on the inversion height to approach zero is $1/D \sim 3$ days. This means that the initial inversion height has a negligible effect on the solution in ~ 3 days. Furthermore, since all u functions have the same exponential trend of $\exp(Dt)$, $z_{\mathrm{i}}(t)$ converges within 5% of steady state in approximately $1/3D \sim 9$ days. Once $z_{\mathrm{i}}(t)$ reaches the steady state solution, the inversion height oscillates with sinusoids of periods 12 hours and 24 hours. However, in practice this finding is largely irrelevant as the synoptic meteorological conditions induce change over shorter time scales rendering the mixed layer model results not applicable.

3.1.5 Cloud Thickness Solution

In order to obtain the final cloud thickness expression, the cloud base height expression is subtracted from the inversion height expression. In Eq. (2.3) only q_{T} and θ_{l} tendencies vary in time as the other terms are either constant or assumed constant due to the assumption of constant effective radiative temperature. We integrate Eq. (2.3) to obtain:

$$\begin{aligned} z_{\mathrm{b}}(t) - z_{\mathrm{b}}(0) &= \frac{\mathrm{R_d T_{base}}}{g}\left(1 - \frac{\mathrm{L_v R_d}}{\mathrm{c_p R_v T_{base}}}\right)^{-1} \ln\left(\frac{q_{\mathrm{T}}(t)}{q_{\mathrm{T}}(0)}\right) \\ &+ \frac{\mathrm{c_p}\Pi_b}{g}\left(1 - \frac{\mathrm{c_p R_v T_{base}}}{\mathrm{R_d L_v}}\right)^{-1}\theta_{\mathrm{l}}(t) \end{aligned} \tag{3.36}$$

Assuming the change in $q_{\mathrm{T}}(t)$ to be small compared to its initial value, we use $\ln(x+1) \simeq x$ to linearize the expression and denote the coefficients of the time-varying terms as δ_1 and δ_2:

$$z_{\mathrm{b}}(t) - z_{\mathrm{b}}(0) = \delta_1(q_{\mathrm{T}}(t) - q_{\mathrm{T}}(0)) + \delta_2(\theta_{\mathrm{l}}(t) - \theta_{\mathrm{l}}(0)) \tag{3.37}$$

$$\frac{dz_{\mathrm{b}}(t)}{dt} = \delta_1\frac{dq_{\mathrm{T}}(t)}{dt} + \delta_2\frac{d\theta_{\mathrm{l}}(t)}{dt} \tag{3.38}$$

In Eq. (3.12) and Eq. (3.13) the $z_{\mathrm{i}}q_{\mathrm{T}}$ and $z_{\mathrm{i}}\theta_{\mathrm{l}}$ differentials are of the same functional form as the inversion height tendency. Thus, we manipulate the cloud base height expressions to obtain the same format so that the total moisture and liquid potential temperature results can be substituted directly. To achieve this, we multiply Eq. (3.37) by dz_{i}/dt and Eq. (3.38) by z_{i} and sum them up to obtain:

$$\frac{d(z_{\mathrm{i}}z_{\mathrm{b}})}{dt} = \delta_1\frac{d(z_{\mathrm{i}}q_{\mathrm{T}})}{dt} + \delta_2\frac{d(z_{\mathrm{i}}\theta_{\mathrm{l}})}{dt} + \frac{dz_{\mathrm{i}}}{dt}(z_{\mathrm{b}}(0) - \delta_1 q_{\mathrm{T}}(0) - \delta_2\theta_{\mathrm{l}}(0)) \tag{3.39}$$

Scaling Eq. (3.37) by Dz_{i} and subtracting it from Eq. (3.39) yields:

$$\frac{dz_{\mathrm{i}}z_{\mathrm{b}}}{dt} - Dz_{\mathrm{i}}z_{\mathrm{b}} = \delta_1\left(\frac{d(z_{\mathrm{i}}q_{\mathrm{T}})}{dt} - Dz_{\mathrm{i}}q_{\mathrm{T}}\right) + \delta_2\left(\frac{d(z_{\mathrm{i}}\theta_{\mathrm{l}})}{dt} - Dz_{\mathrm{i}}\theta_{\mathrm{l}}\right) \tag{3.40}$$

$$+ \left(\frac{dz_{\mathrm{i}}}{dt} - Dz_{\mathrm{i}}\right)(z_{\mathrm{b}}(0) - \delta_1 q_{\mathrm{T}}(0) - \delta_2\theta_{\mathrm{l}}(0)) \tag{3.41}$$

The $z_{\mathrm{i}}q_{\mathrm{T}}$ and $z_{\mathrm{i}}\theta_{\mathrm{l}}$ differentials can be substituted from Eq. (3.12) and Eq. (3.13):

$$\begin{aligned} \frac{dz_{\mathrm{i}}(z_{\mathrm{b}} - z_{\mathrm{adj}})}{dt} - Dz_{\mathrm{i}}(z_{\mathrm{b}} - z_{\mathrm{adj}}) &= \frac{\delta_2\left(\beta + 1 - \alpha_{\mathrm{srf}}\beta\right)\mathrm{L_v} - \delta_1\alpha_{\mathrm{srf}}\mathrm{c_p}}{\rho_{\mathrm{air}}\mathrm{c_p L_v}(\beta+1)}\mathrm{F_{rad}}(0,t) \\ &- \frac{\delta_2\mathrm{F_{rad}}(z_{\mathrm{i}}(t),t)}{\rho_{\mathrm{air}}\mathrm{c_p}} \end{aligned} \tag{3.42}$$

where $z_{\text{adj}} \triangleq z_{\text{b}}(0) + \delta_1 \Delta\theta_{\text{l, i}} + \delta_2 \Delta q_{\text{T, i}}$. Aggregating all constant coefficients in ψ_3 and ψ_4 we obtain:

$$\frac{dz_{\text{i}}(z_{\text{b}} - z_{\text{adj}})}{dt} - Dz_{\text{i}}(z_{\text{b}} - z_{\text{adj}}) = \psi_3 \text{F}_{\text{rad}}(0,t) + \psi_4 \text{F}_{\text{rad}}(z_{\text{i}}(t),t) \quad (3.43)$$

$$\psi_3 \triangleq \frac{\delta_2(1-\alpha_{\text{srf}})}{\rho_{\text{air}}\text{c}_{\text{p}}} + \frac{\delta_2 \alpha_{\text{srf}} \text{L}_{\text{v}} - \delta_1 \alpha_{\text{srf}} \text{c}_{\text{p}}}{\rho_{\text{air}} \text{c}_{\text{p}} \text{L}_{\text{v}} (\beta + 1)}, \qquad \psi_4 \triangleq -\frac{\delta_2}{\rho_{\text{air}}\text{c}_{\text{p}}} \quad (3.44)$$

Eq. (3.42) depends only on the radiation terms which already had been derived for the inversion height expression:

$$z_{\text{i}}(t)(z_{\text{b}}(t) - z_{\text{adj}}) = z_{\text{i}}(0)(z_{\text{b}}(0) - z_{\text{adj}})e^{Dt} + b_0 u_1(t) + b_1 u_2(t) + b_2 u_3(t) \quad (3.45)$$

where the constants are combined into b_1, b_2 and b_3 for convenience. Solving for the cloud base height, we obtain:

$$z_{\text{b}}(t) = \frac{b_1 u_1(t) + b_2 u_2(t) + b_3 u_3(t) + z_{\text{i}}(0)(z_{\text{b}}(0) - z_{\text{adj}})e^{Dt}}{a_1 u_1(t) + a_2 u_2(t) + a_3 u_3(t) + z_{\text{i}}(0)e^{Dt}} + z_{\text{adj}} \quad (3.46)$$

And finally, the cloud thickness is obtained from $h(t) = z_{\text{i}}(t) - z_{\text{b}}(t)$.

3.2 Validation against LES

We verify our solution against Large Eddy Simulation (LES) specifically the UCLA-LES ([29]) on a 100×100 grid with 193 vertical levels. The horizontal resolution is 25 m and the vertical resolution is 5 m resulting in a domain of 2.5 km $\times$ 2.5 km $\times$ 960 m. The LES land surface model is a constant Bowen Ratio model that converts the incoming net radiation into SHF and LHF according to Eqs. (2.40) and Eq. (2.41). Initial conditions are CGILS s12 from [38] and initial profiles of q_{T} and θ_{l} are shown in Figure 3.2. The initial inversion height is 677 m, the initial cloud thickness is 238 m and LWP is 72.4 g m^{-2}. LES is initialized at 03:00 LST. The results for the first hour of integrations are considered spin-up time and not shown. LES is run for 23 more hours with samples taken every 20 seconds and averaged over 10 minutes. LES inversion height, cloud base height, inversion jumps for total moisture and liquid potential temperature, total moisture at the surface, and the effective radiative temperatures T_{srf} and T_{cld} at 04:00 LST serve as initial conditions for the analytic model. The effective downwelling radiative

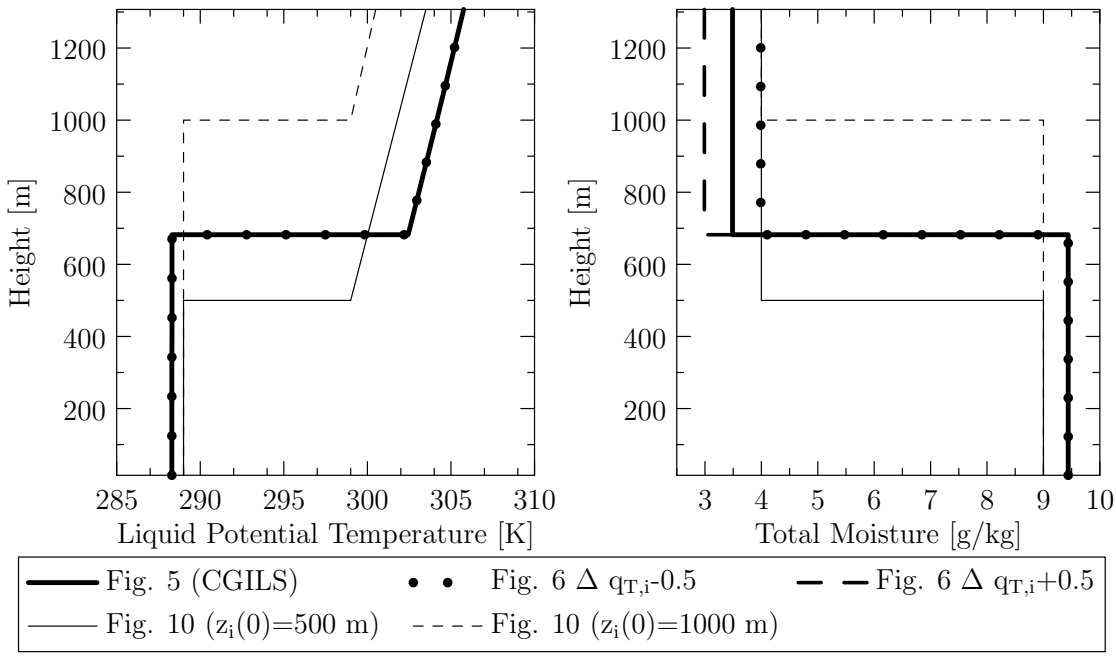

Figure 3.2: Initial profiles used for solutions and simulations. Initial profiles of liquid potential temperature and total water mixing ratio used for LES are taken from CGILS s12 data (thick solid line). Throughout this chapter, the initial profiles have been slightly modified to study various conditions, such as total moisture jump sensitivity in Fig. 3.4 (dotted and thick dashed lines) and initial inversion height sensitivity in Fig. 3.8 (thin solid and dashed lines).

temperature above the cloud top (T_{sky}) is obtained from the LES longwave flux, the constant value of the exponential optical depth ($\exp(k\tau_b)$) is calculated from LES shortwave flux and the subsidence divergence (D) is extracted from LES using Eq. (2.2) by subtracting entrainment from the inversion height derivative.

The validation consisted of two sets of sensitivity experiments: 1) Varying Bowen Ratio and 2) Varying $\Delta q_{T,\,i}$ jump at the inversion. Bowen Ratio sensitivity results in Figure 3.3 show agreement in the inversion height and cloud thickness time series, and cloud dissipation time; the inversion height RMSE compared to LES is less than 1.5% and the cloud thickness RMSE is less than 9%.

At this time, the cloud base height can also be compared against the *lifting condensation level* (LCL) - the level, where the moisture in air is expected to saturate based on surface temperature and relative humidity ([39]). The LCL results for $\beta = 0.1$ and $\beta = 0.2$ in Figure 3.3 agree with our cloud thickness

formulation. The small difference is due to the approximate nature of the LCL formulation. We use the current formulation ([33]) for the rest of this paper, since it is integrated with the simulated MLM profiles. In contrast, the LCL formulation depends on near-surface temperature and relative humidity, which would require additional equations to obtain the closed-form results.

Both inversion height (Eq. (3.28)) and cloud base height (Eq. (3.45)) were shown to depend on the inversion jump, including the total moisture jump, $\Delta q_{\mathrm{T,\,i}}$. Furthermore, the inversion jump also affects entrainment and the turbulent fluxes through the boundary conditions (Eqs. (2.11), (2.13)). Even though multiple interdependent variables depend on $\Delta q_{\mathrm{T,\,i}}$, we are able to infer how $\Delta q_{\mathrm{T,\,i}}$ affects the cloud thickness through our analytic solution. A detailed sensitivity analysis is presented in Section 3.3, where the analytic solution suggests that the inversion height decreases and cloud thickness increases with smaller magnitude inversion jumps. For the validation, LES were run for Bowen Ratios of 0.3 and 1 and the q_{T} jump was varied by ∓ 0.5 g kg^{-1} (moister and drier air in the free troposphere), while keeping the boundary layer value at 9.43 g kg^{-1}. Figure 3.4 shows that the analytic solution closely follows LES results in both trend and dissipation times. The inversion height RMSE compared to LES is again less than 1.5% and the cloud thickness RMSE is less than 5%. The underestimation of the inversion height is offset by a similar amount for cloud base height, which in return results in a low cloud thickness error. The cloud dissipates only for $\beta = 1$ and the time of dissipation differs only by 5 minutes.

3.3 Sensitivity Analysis

3.3.1 Inversion Height Sensitivity

In section 3.1, we found that the inversion height tendency is a linear combination of 3 functions: u_1, u_2 and u_3. The common property of these functions is that they generally increase exponentially and the exponent is the subsidence divergence (D). The evolution of the inversion height in time then depends on the coefficients of these functions given in Eq. (3.29), where the coefficients were kept

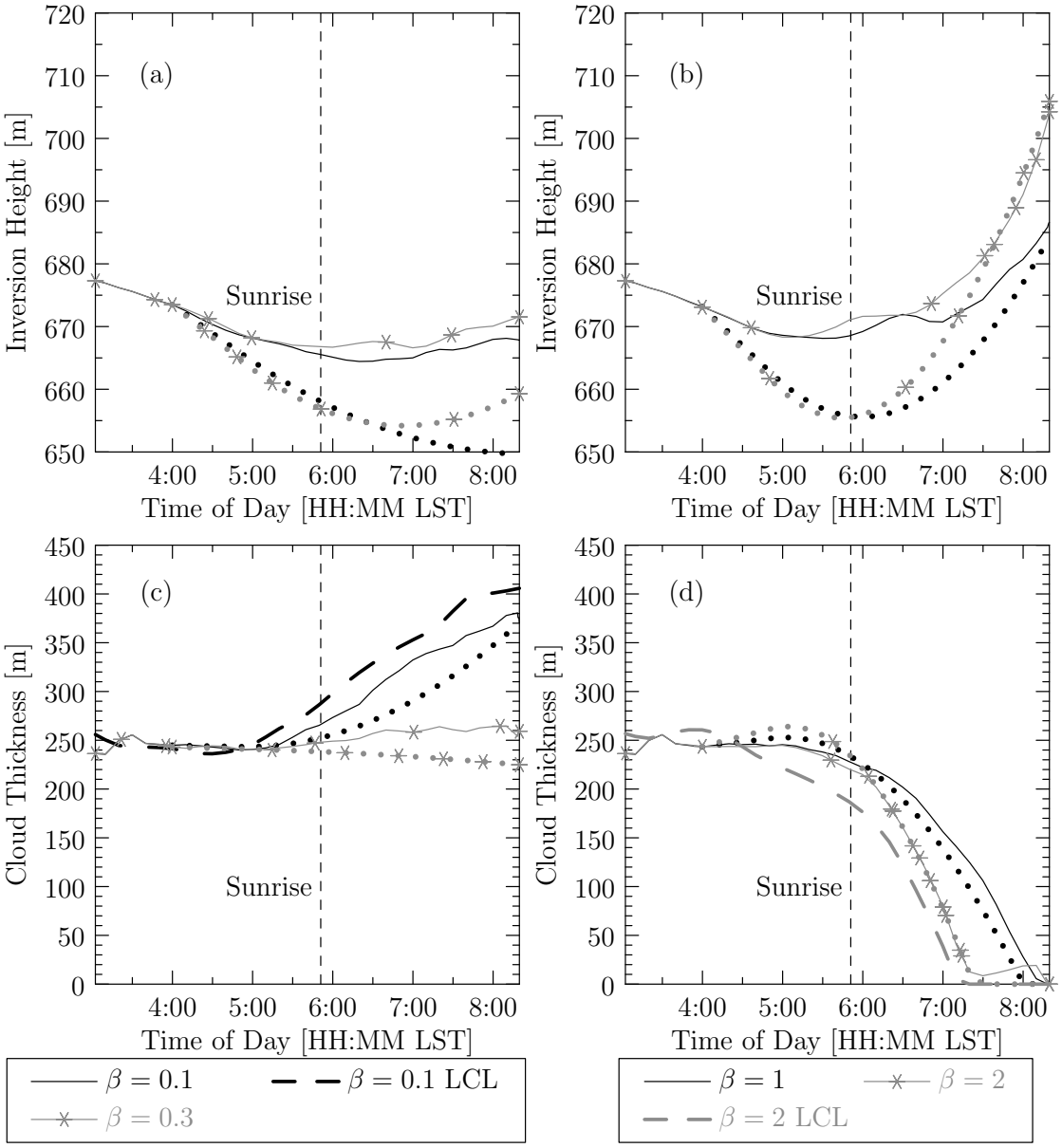

Figure 3.3: Bowen Ratio sensitivity comparison between the analytic solution and LES results. Analytic solution is represented by dotted lines and LES simulations as solid lines. Simulations are shown until the cloud dissipated for the largest Bowen Ratio, i.e. until 0800 LST, because the analytic model is not valid in clear conditions. Inversion height, z_i, is plotted for (a) $\beta = \{0.1, 0.3\}$ and (b) $\beta = \{1, 2\}$. Cloud thickness, h, is plotted for (c) $\beta = \{0.1, 0.3\}$ and (d) $\beta = \{1, 2\}$. Cloud thickness was also calculated using LCL for the $\beta = 0.1$ and $\beta = 2$ cases (dashed). The vertical dashed lines mark sunrise.

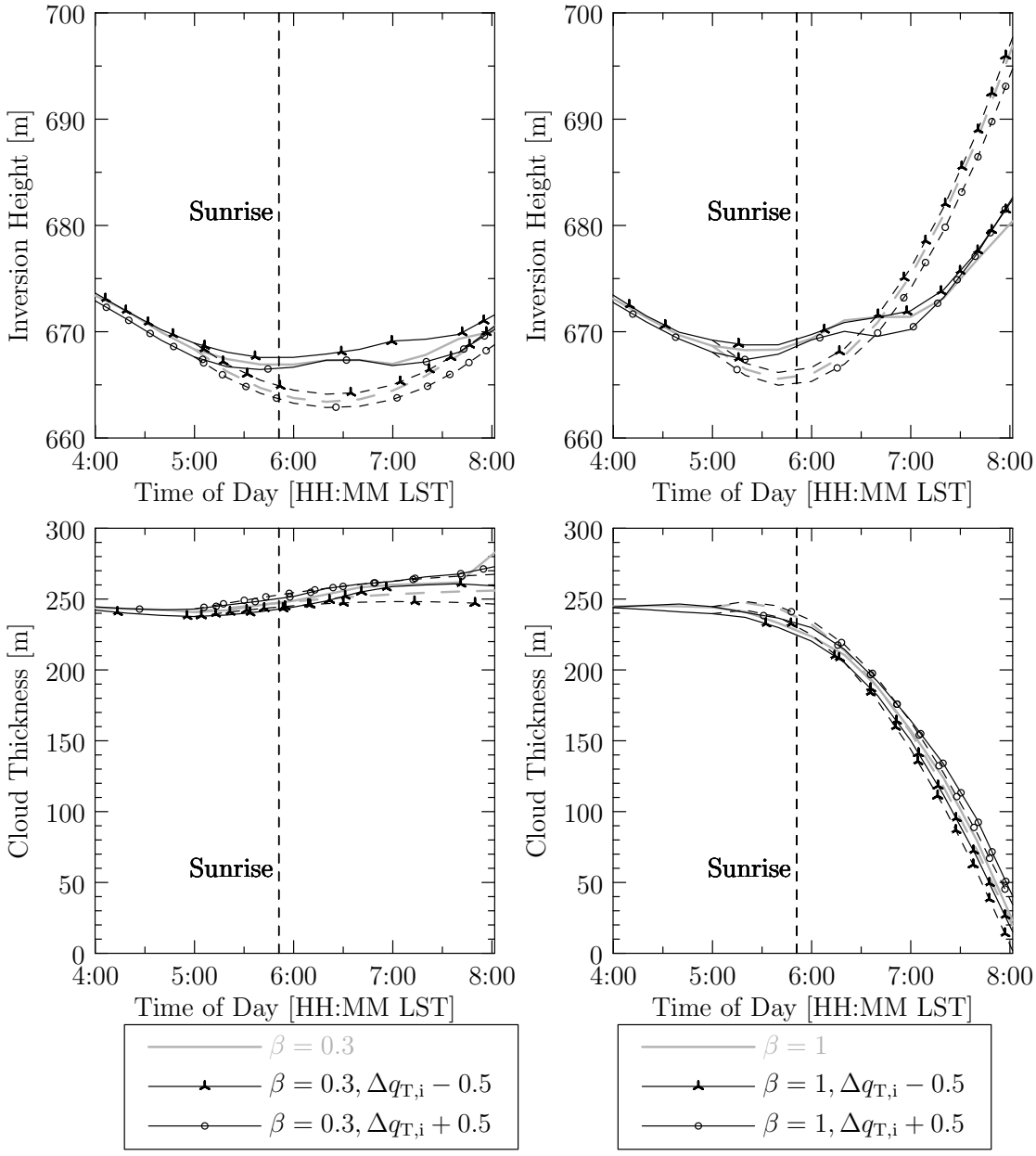

Figure 3.4: Sensitivity of inversion height (top), and cloud thickness (bottom) to total moisture jump at the inversion and initial cloud base height, computed by the analytic solution (dashed) and the LES simulation (solid lines). Results for Bowen Ratios of 0.3 (left) and 1 (right) are shown. The original total moisture jump is colored gray, reduced case is marked with triangle and the increased case is marked with a circle.

in their compact forms to emphasize the linear combination of the three functions. Now, we write out these coefficients and analyze their dependence on the initial and boundary conditions.

$$a_1 = \frac{4\pi(1-\omega_{\mathrm{lw}})}{\mathrm{c}_{2,\,\mathrm{lw}}^2}\left((\mathrm{c}_{2,\,\mathrm{lw}}\psi_1 + 2e_{\mathrm{lw}}\alpha_{\mathrm{lw}}\psi_2)(\mathrm{B}_{\mathrm{srf}} - \mathrm{B}_{\mathrm{cld}}) + (\mathrm{c}_{2,\,\mathrm{lw}}\psi_2 + 2e_{\mathrm{lw}}\alpha_{\mathrm{lw}}\psi_1)(\mathrm{B}_{\mathrm{cld}} - \mathrm{B}_{\mathrm{sky}})\right) \quad (3.47)$$

$$a_2 = -(\psi_2 + e_1\psi_1)F_0\left(1 - \frac{4\beta_{\mathrm{sw}}}{3+2p} + e_2\left(\frac{4\beta_{\mathrm{sw}}}{3+2p} - A\right)\right) \quad (3.48)$$

$$a_3 = -(1-e_2)(\psi_2 + e_1\psi_1)F_0\left(\frac{3p\omega_{\mathrm{sw}}(1+\mathrm{g}_{\mathrm{sw}}(1-\omega_{\mathrm{sw}}))}{3+2p}\right) \quad (3.49)$$

$$\psi_1 \triangleq \frac{\frac{c_1-\alpha_{\mathrm{srf}}c_1-2s_1}{\mathrm{c_p}\rho_{\mathrm{air}}} + \frac{\alpha_{\mathrm{srf}}(c_1\mathrm{L_v}-c_2\mathrm{c_p})}{\mathrm{c_p}\rho_{\mathrm{air}}\mathrm{L_v}(\beta+1)}}{\frac{0.8\Delta\theta_{\mathrm{v,\,i}}}{\mathrm{A_w}} + c_3\Delta\theta_{\mathrm{l,\,i}} + c_4\Delta q_{\mathrm{T,\,i}}}, \qquad \psi_2 \triangleq \frac{\frac{c_3-2s_2}{\mathrm{c_p}\rho_{\mathrm{air}}}}{\frac{0.8\Delta\theta_{\mathrm{v,\,i}}}{\mathrm{A_w}} + c_3\Delta\theta_{\mathrm{l,\,i}} + c_4\Delta q_{\mathrm{T,\,i}}} \quad (3.50)$$

where for convenience, we defined $e_m \triangleq \exp(-mk\tau_{\mathrm{b}})$ and $e_{\mathrm{lw}} \triangleq \exp(-\alpha_{\mathrm{lw}}\tau_{\mathrm{b}})$ and remember that the exponential optical depth value ($\exp(-k\tau_{\mathrm{b}})$) was assumed to be constant in Section 3.1.4.

The turbulent flux coefficients in Eq. (3.1), $c_1 = 1, c_2 = 108$ K, $c_3 = 0.5, c_4 = 970$ K, and the convective surface efficiency of $\alpha_{\mathrm{srf}} = 0.9$ in Eq. (2.40) and Eq. (2.41) are obtained from [30]. $\mathrm{A_w} = 0.2$ in Eq. (2.38) is from [36]. Constants related to longwave radiation are from [26] and shortwave radiation from [32]. The coefficients become:

$$\begin{aligned} a_1 &\simeq \frac{\left(39.55\times10^{-12}\ \mathrm{m\ s^{-1}\ K^{-3}}\right)}{\zeta_D}\left(\left(\frac{1}{\beta+1} - 2.29 + 0.52e_{\mathrm{lw}}\right)(\mathrm{T}_{\mathrm{srf}}^4 - \mathrm{T}_{\mathrm{cld}}^4)\right. \\ &+ \left.\left(\frac{e_{\mathrm{lw}}}{\beta+1} - 2.31e_{\mathrm{lw}} + 0.51\right)(\mathrm{T}_{\mathrm{cld}}^4 - \mathrm{T}_{\mathrm{sky}}^4)\right) \quad (3.51) \\ a_2 &\simeq \frac{(0.23\ \mathrm{m\ s^{-1}\ K})(0.23+e_2)}{\zeta_D}\left(2.3e_1 - 0.52 - \frac{e_1}{\beta+1}\right) \quad (3.52) \\ a_3 &\simeq (1-e_2)\frac{a_2}{1.53} \quad (3.53) \\ \zeta_D &\triangleq 4\Delta\theta_{\mathrm{v,\,i}} + 0.5\Delta\theta_{\mathrm{l,\,i}} + (970\ \mathrm{K})\Delta q_{\mathrm{T,\,i}} \quad (3.54) \end{aligned}$$

where ζ_D aggregates the inversion jumps and has been defined for notational convenience. The unit of ζ_D is K, $[\psi_1] = [\psi_2] =$ $\mathrm{W^{-1}\ s^{-1}\ m^3}$, and $[a_1] = [a_2] = [a_3] =$ $\mathrm{m\ s^{-1}}$.

Furthermore, a_2 is a scalar multiple of a_3, so we can combine the $u_2(t)$ and $u_3(t)$ functions into a new function $u_4(t) = u_2(t) + u_3(t)\frac{1-e_2}{1.53}$. Combining the

coefficients, the inversion height expression becomes:

$$z_{\mathrm{i}}(t) = z_{\mathrm{i}}(0)e^{Dt} + a_1 u_1(t) + a_2 u_4(t) \tag{3.55}$$

The functions u_1 and u_4 are always positive. Thus, their combined tendency in time depends on the sign and magnitude of their coefficients. ζ_D is the common denominator of all coefficients and its only negative term is the inversion jump in total moisture. However, given the strong temperature inversions for the stratocumulus-topped marine boundary layer, the total moisture jump would have to be unrealistically large to create a negative sign for ζ_D. For example, if $\Delta\theta_{\mathrm{v,\,i}} = \Delta\theta_{\mathrm{l,\,i}} = 10$ K, the jump in total moisture would have to be 33 g kg^{-1} to reverse the sign, but typical values of q_{T} in the boundary layer are only 10 g kg^{-1}. Thus let us assume that $\zeta_D > 0$ K.

For the optical depth exponentials, e_1 and e_{lw}, a thinner cloud ranging between $[0, 200]$ m thickness and a thicker cloud in the interval $[200, 400]$ m are analyzed. For the thinner cloud, the optical depth variables are calculated as: $e_1 = 0.9, e_{\mathrm{lw}} = 0.39$; and for the thicker cloud: $e_1 = 0.7, e_{\mathrm{lw}} = 0.03$. For the thin cloud case, a_2 is positive for all Bowen Ratios. For a_1, there is a balance between the $\mathrm{B_{cld}} - \mathrm{B_{sky}}$ and $\mathrm{B_{srf}} - \mathrm{B_{cld}}$ blackbody radiation differences, slightly weighted towards the latter. The effect of Bowen Ratio is small due to its coefficient being small relative to the rest of the terms. A low radiative temperature for the cloud ($\mathrm{T_{cld}}$) favors positive a_1, whereas high surface or $\mathrm{T_{sky}}$ radiative temperatures favor negative a_1. Using the standard atmospheric lapse rate of -6.5 K km^{-1} and assuming that effective radiative temperature equals air temperature, a_1 is always negative for the thin cloud case. A negative a_1 means that the inversion height increases proportionally with the $\mathrm{T_{sky}}$ radiative temperature and inversely proportional with the surface radiative temperature. A large $\mathrm{T_{sky}}$ would lead to a higher downwelling longwave radiation and thus faster warming. For a thin cloud with low optical depth, a large proportion of the downwelling longwave radiation from above the cloud top reaches the surface and contributes to the sensible heat flux. This leads to a temperature increase in the boundary layer, increasing the turbulent fluxes and entrainment, which results in increased inversion height. For a thick cloud, most of the downwelling radiation above the cloud will be attenuated

and doesn't contribute to the surface fluxes, resulting in a cooler boundary layer. It contributes to the inversion layer without being attenuated, resulting in a decline in the inversion height as opposed to the thin cloud case.

For the thick cloud case, a_2 is positive for all Bowen Ratios. The sign of a_1 depends on both the Bowen Ratio and the radiative temperature balance. However, only the sign of the T_{sky} term is negative for all Bowen Ratios, thus the inversion height is inversely proportional to the T_{sky} radiative temperature. The change in the direction of the effect for a thicker cloud emerges since the downwelling longwave radiation above the cloud top is attenuated through the cloud's high optical thickness and only a negligible fraction reaches the surface.

To infer the combined effect of the oscillating terms in Eq. (3.55), we need the numerical values of u_1 and u_4. For $D = -3.75 \times 10^{-6}$ s^{-1}, Julian day of 196 and latitude 32.85° N, $u_4 \approx 8.2u_1$ in magnitude on average. For typical effective radiative temperatures, it is physically impossible for the weighted summation $(a_1u_1 + a_2u_4)$ to be negative. For example, for thin clouds if $T_{cld} = T_{sky}$, T_{srf} would have to be more than 560 K to cause a negative trend during day time. Increasing Bowen Ratio increases a_2. Since u_4 is the dominant term, the combined trend increases with Bowen Ratio. To show this, we fix T_{srf}, T_{cld}, ζ_D, D and vary the Bowen Ratio and T_{sky}, as shown in Figure 3.5.

Before sunrise $u_4 = 0$ such that the results represent only u_1 and all lines for both thin and thick clouds show a downward slope since the negative term of a_1 is dominant. This comes from the fact that a_1 includes only net longwave radiation terms. During the night, the net longwave radiation causes the boundary layer to cool decreasing the inversion height. For the thin cloud case, throughout the day higher T_{sky} radiative temperatures are associated with larger inversion height since the cloud's optical thickness is small enough to admit downwelling longwave radiation to the surface, which is converted into sensible heat flux and warms up the boundary layer. For the thick case, we see exactly the opposite, where higher T_{sky} radiative temperature leads to lower inversion heights. A large optical thickness attenuates the downwelling radiation above the cloud before it reaches the land surface, which results in a cooler mixing layer and reduces surface

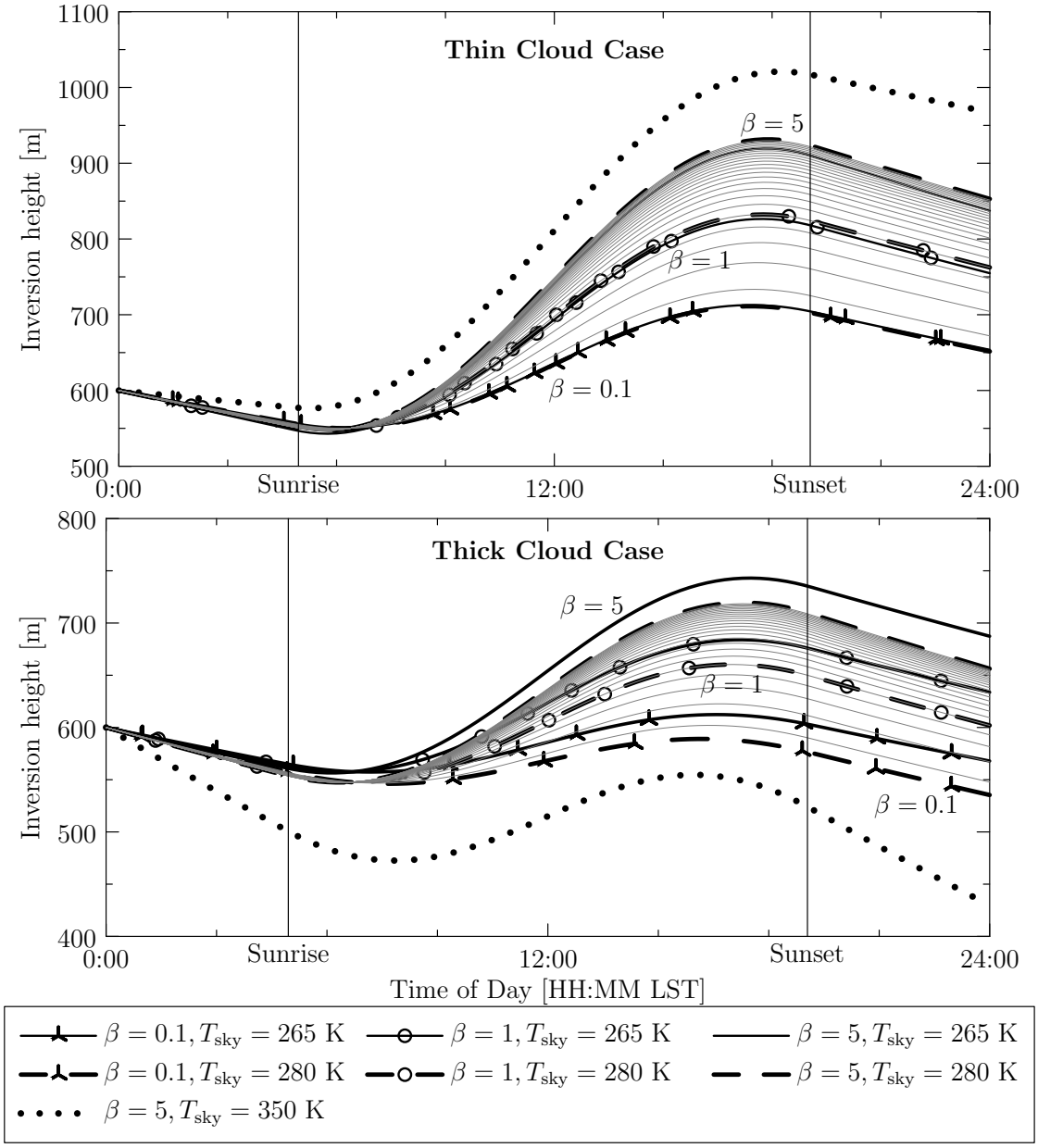

Figure 3.5: Inversion height trend ($z_{\mathrm{i}}(t)$) with respect to different Bowen Ratios and $\mathrm{T_{sky}}$ radiative temperatures for the thin cloud case ($[0, 200]$ m, top) and the thick cloud case ($[200, 400]$ m, bottom). Other variables are fixed at $\mathrm{T_{srf}} = 289$ K, $\mathrm{T_{cld}} = 285$ K, $\zeta_D = 51$ K, $D = -3.75 \times 10^{-6}$ s^{-1}. Simulations with $\mathrm{T_{sky}} = 265$ K (solid) and $\mathrm{T_{sky}} = 280$ K (dashed) are shown. Simulations for Bowen Ratios between 0.1 and 5 are shown as thin gray lines for the $\mathrm{T_{sky}} = 280$ K case with 0.2 increments. The dotted line is an admittedly unrealistic parameter choice to show a case where $z_{\mathrm{i}}(t)$ decreases. For this and all future graphs a latitude equal to 32.85° N and Julian day of 196 were used for solar zenith angle calculations.

turbulent fluxes.

Larger Bowen Ratio causes z_{i} to increase by a factor of $1/(\beta+1)$ as is illustrated by the spacing between the gray lines of constant Bowen Ratios for $\mathrm{T_{sky}} = 280$ K. Decreased moisture content in the soil associated with larger Bowen Ratio increases the sensible heat flux and the warming increases the inversion height. Since the ratio of radiation flux converted into turbulent fluxes is fixed through α_{srf}, the rate of the increases in the sensible heat flux and inversion height slow with increasing Bowen Ratio as reflected in the closer line spacing. Finally, the trend of the inversion height is also affected inversely by ζ_D. A larger jump in potential temperature results in a smaller change in inversion height, whereas a larger jump in the magnitude of total water mixing ratio causes in contrast a greater change. This arises mainly from the fact that the turbulent fluxes are bounded by the negative of the inversion jumps at the inversion layer, as presented in Eqs. (2.11), (2.13).

3.3.2 Cloud Base Height Sensitivity

For the sensitivity analysis of the cloud base height from Eq. (3.46) it is enlightening to analyze $z_{\mathrm{i}}(z_{\mathrm{b}} - z_{\mathrm{adj}})$ as – similar to z_{i} – its functional form is a linear combination of the three u functions in Eq. (3.45). The coefficients of u_1, u_2, and u_3 are:

$$b_1 = \frac{4\pi(1-\omega_{\mathrm{lw}})}{\mathrm{c}_{2,\,\mathrm{lw}}^2}\left((\mathrm{c}_{2,\,\mathrm{lw}}\psi_3 + 2e_{\mathrm{lw}}\alpha_{\mathrm{lw}}\psi_4)(\mathrm{B_{srf}} - \mathrm{B_{cld}}) + (\mathrm{c}_{2,\,\mathrm{lw}}\psi_4 + 2e_{\mathrm{lw}}\alpha_{\mathrm{lw}}\psi_3)(\mathrm{B_{cld}} - \mathrm{B_{sky}})\right) \tag{3.56}$$

$$b_2 = -(\psi_4 + e_1\psi_3)F_0\left(1 - \frac{4\beta_{\mathrm{sw}}}{3+2p} + e_2\left(\frac{4\beta_{\mathrm{sw}}}{3+2p} - A\right)\right) \tag{3.57}$$

$$b_3 = -(1-e_2)(\psi_4 + e_1\psi_3)F_0\left(\frac{3p\omega_{\mathrm{sw}}(1+\mathrm{g_{sw}}(1-\omega_{\mathrm{sw}}))\alpha_{\mathrm{sw}}}{3+2p}\right) \tag{3.58}$$

with

$$\psi_3 \triangleq \frac{\delta_2(1-\alpha_{\mathrm{srf}})}{\rho_{\mathrm{air}}\mathrm{c_p}} + \frac{\delta_2\alpha_{\mathrm{srf}}\mathrm{L_v} - \delta_1\alpha_{\mathrm{srf}}\mathrm{c_p}}{\rho_{\mathrm{air}}\mathrm{c_p}\mathrm{L_v}(\beta+1)}, \qquad \psi_4 \triangleq -\frac{\delta_2}{\rho_{\mathrm{air}}\mathrm{c_p}} \tag{3.59}$$

δ_1 and δ_2 from Eq. (3.38) are calculated using $q_T(0) = 9$ g kg^{-1} value as

-211590 m K^{-1} and 125 m K^{-1}, respectively. The coefficients become:

$$b_1 \simeq \left(9.2 \times 10^{-9} \text{ m}^2 \text{ s}^{-1} \text{ K}^{-4}\right) \left(\left(\frac{1}{\beta + 1} + 1.88 - 2.21 e_{\text{lw}} \right) \left(\text{T}_{\text{srf}}^4 - \text{T}_{\text{cld}}^4 \right) + \left(\frac{e_{\text{lw}}}{\beta + 1} + 1.88 e_{\text{lw}} - 2.22 \right) \left(\text{T}_{\text{cld}}^4 - \text{T}_{\text{sky}}^4 \right) \right)$$

$$b_2 \simeq (11 \text{ m}^2 \text{ s}^{-1})(0.235 + e_2) \left(7.33 - e_1 - \frac{12.43 e_1}{\beta + 1} \right)$$

$$b_3 = (1 - e_2) b_2 / 1.53$$

The units of ψ_3 and ψ_4 are W^{-1} s^{-1} m^4, and $[b_1] = [b_2] = [b_3] =$ m^2 s^{-1}. As for the inversion height (Eq. (3.55)), u_2 and u_3 are combined into u_4:

$$z_{\text{i}}(z_{\text{b}} - z_{\text{adj}}) = z_{\text{i}}(0)(z_{\text{b}}(0) - z_{\text{adj}}) e^{Dt} + b_1 u_1(t) + b_2 u_4(t) \tag{3.60}$$

As in the inversion height analysis in Section 3.33.3.1, we consider two cases of thin and thick clouds with $e_1 = 0.9$, $e_{\text{lw}} = 0.39$ and $e_1 = 0.7$, $e_{\text{lw}} = 0.03$, respectively.

As with the coefficient of inversion height a_1, for b_1 there is a balance between the $\text{B}_{\text{srf}} - \text{B}_{\text{cld}}$ and $\text{B}_{\text{cld}} - \text{B}_{\text{sky}}$ blackbody radiation differences. Using a lapse rate for a standard atmosphere b_1 is negative for any Bowen Ratio. The equation for b_2 is very similar to a_2, except that for Bowen Ratios $\beta \geq 0.74$ for the thin cloud case and $\beta \geq 0.31$ for the thick cloud case, b_2 changes sign and becomes positive. The combined trend depends on the u_1 and u_4 functions. Since $u_4 \approx 8.2 u_1$ and b_2 is much greater than b_1, b_2 is the dominant term in the equality. Therefore the sign of $z_{\text{i}}(z_{\text{b}} - z_{\text{adj}})$ changes with the sign of b_2 during daytime. To show this, similar to the inversion height analysis, the sensitivity of β and T_{sky} is shown in Figure 3.6. The results for the daytime reflect sign and magnitude variation in u_4 with Bowen Ratio. As expected, cloud base height starts to increase during daytime at a Bowen Ratio of 0.47 and the cloud base height increases with increasing Bowen Ratio. The sensitivity to T_{sky} radiative temperature is small due to the dominance of u_4. $z_{\text{i}}(z_{\text{b}} - z_{\text{adj}})$ is only an intermediate expression that allows understanding cloud base height trends, but it does not have a physical meaning;

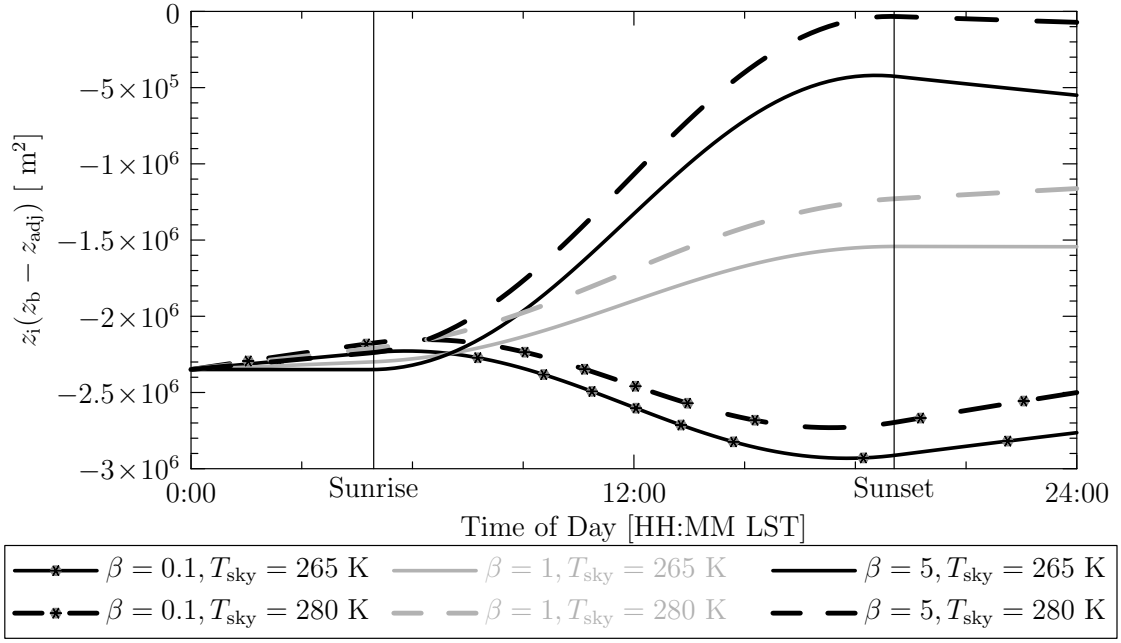

Figure 3.6: $z_i(z_b - z_{adj})$ (proxy for cloud base height) timeseries for different Bowen Ratios and T_{sky} radiative temperatures. Cases for $T_{sky} = 265$ K (solid) and $T_{sky} = 280$ K (dashed) are shown. Other variables are fixed at $T_{srf} = 289$ K, $T_{cld} = 285$ K, $\zeta_D = 51$ K, $D = -3.75 \times 10^{-6}$ s^{-1}.

instead Eq. (3.46) is considered now:

$$z_{\mathrm{b}}(t) = z_{\mathrm{b}}(0) + \frac{(b_1 + a_1(\delta_1 \Delta q_{\mathrm{T,\,i}} + \delta_2 \Delta \theta_{\mathrm{l,\,i}}))u_1(t)}{z_{\mathrm{i}}(0)e^{Dt} + a_1 u_1(t) + a_2 u_4(t)} + \frac{(b_2 + a_2(\delta_1 \Delta q_{\mathrm{T,\,i}} + \delta_2 \Delta \theta_{\mathrm{l,\,i}}))u_4(t)}{z_{\mathrm{i}}(0)e^{Dt} + a_1 u_1(t) + a_2 u_4(t)} \tag{3.61}$$

Using the values from the sensitivity analysis for $z_{\mathrm{i}}(z_{\mathrm{b}} - z_{\mathrm{adj}})$ and z_{i}, and neglecting the u_1 terms as u_4 is the dominant term during daytime:

$$z_{\mathrm{b}}(t) \simeq z_{\mathrm{b}}(0) + (4.34\ \mathrm{m}^2)(0.23 + e_2)\left(15.6 + 13e_1 - \frac{38.6e_1}{\beta + 1}\right)\frac{u_4(t)}{z_{\mathrm{i}}(0)e^{Dt}} \tag{3.62}$$

For the thin cloud case, cloud base height changes direction for $\beta \geq 0.27$, whereas for the thick cloud case, the direction change occurs for $\beta \geq 0.1$. The cloud base height for different Bowen Ratios is plotted in Figure 3.7. This result shows that the cloud base height trend changes direction depending on the Bowen Ratio. Only a single $\mathrm{T_{sky}}$ radiative temperature is shown as the effect of u_1 is negligible. Increasing Bowen Ratio causes a decrease in the latent heat flux and an increase in the sensible heat flux. The resulting drying and heating of the boundary layer increases the cloud base height more than the inversion height. The cloud then dissipates faster with increasing Bowen Ratios. The effect of Bowen Ratio decreases with increasing cloud optical thickness, as more radiation is absorbed or reflected within the cloud resulting in smaller surface turbulent fluxes.

Furthermore, note that the cloud base height converges to a steady state:

$$z_{\mathrm{b}}(t \to \infty) \simeq z_{\mathrm{b}}(0) + \delta_1 \Delta \theta_{\mathrm{l,\,i}} + \delta_2 \Delta q_{\mathrm{T,\,i}} + \frac{b_2}{a_2} = z_{\mathrm{adj}} + \frac{b_2}{a_2} \tag{3.63}$$

As shown earlier in this section, a_2 is positive and b_2 changes from negative to positive with higher Bowen Ratios. Therefore, larger Bowen Ratios lead to larger steady state cloud base height.

3.3.3 Cloud Thickness Sensitivity

Using inversion height and cloud base height trends, we can directly infer the cloud thickness sensitivity. In this section we study the maximum initial cloud thickness that can be dissipated 1) before sunrise, 2) before sunset or whether the cloud dissipates within 24 hours at all.

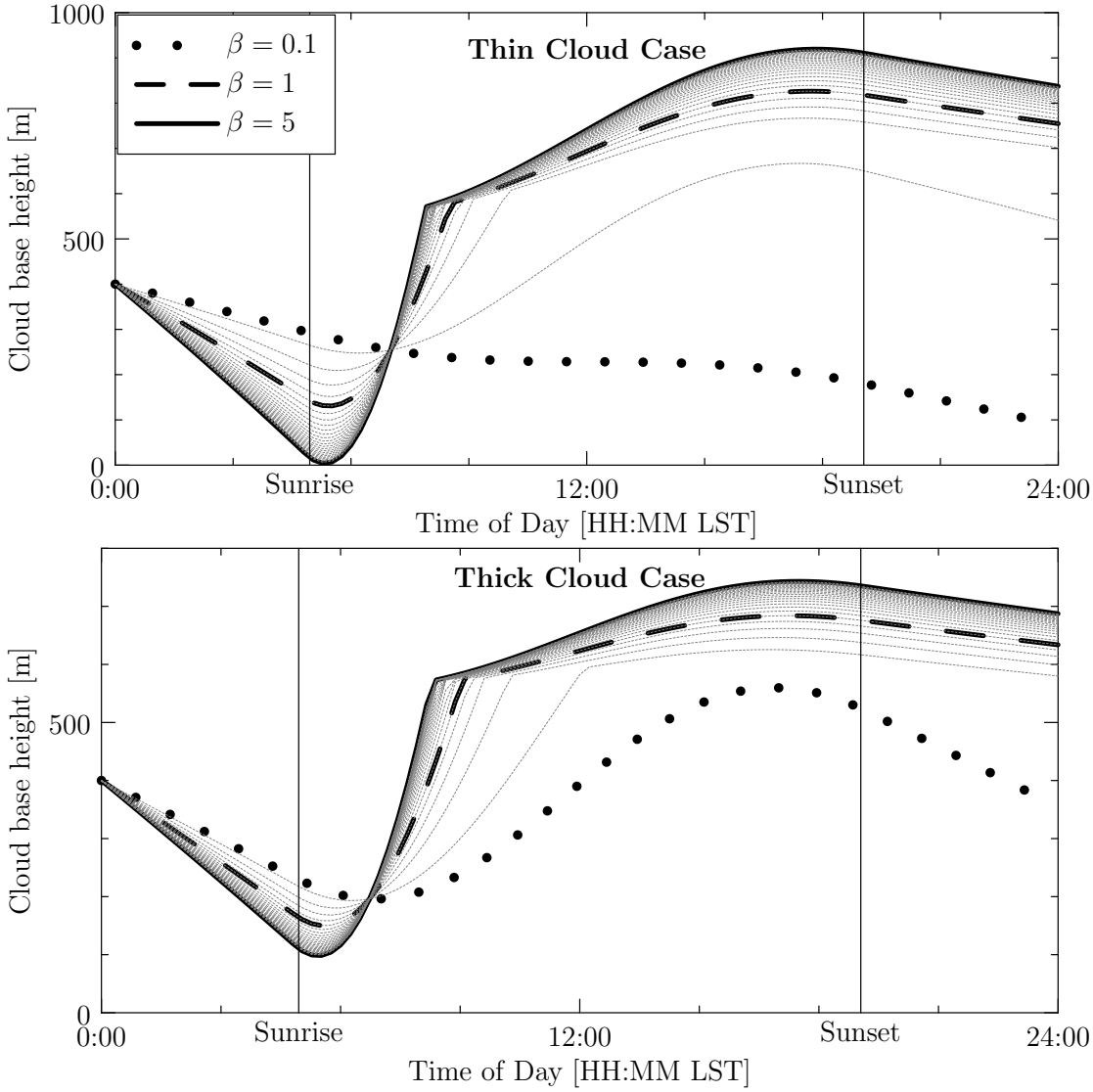

Figure 3.7: Cloud Base Height timeseries ($z_{\mathrm{b}}(t)$) for different Bowen Ratios for the thin cloud case ($[0, 200]$ m, top) and the thick cloud case ($[200, 400]$ m, bottom). The kink in the line occurs when the cloud base height reaches the inversion height. The thin gray lines represent Bowen Ratios from 0.1 to 5 with 0.2 increments. Other variables are fixed at $\mathrm{T_{srf}} = 289$ K, $\mathrm{T_{cld}} = 285$ K, $\zeta_D = 51, D = -3.75 \times 10^{-6}$ s^{-1}, $z_{\mathrm{adj}} = 1600$ m, $z_{\mathrm{i}}(0) = 600$ m, $\mathrm{T_{sky}} = 265$ K.

Table 3.1: Projected critical cloud thickness values for the cases in Fig. 3.8.

	$\beta = 0.2, z_{\mathrm{i}}(0) = 1500$ m, D_n	$\beta = 0.6, z_{\mathrm{i}}(0) = 1500$ m, D_n
Before sunrise	75 m	56 m
Before sunset	19 m	506 m
Dissipation Time	none	9.7 hours
	$\beta = 0.2, z_{\mathrm{i}}(0) = 500$ m, D_n	$\beta = 0.6, z_{\mathrm{i}}(0) = 500$ m, D_n
Before sunrise	0 m	0 m
Before sunset	0 m	500 m
Dissipation Time	none	9.2 hours
	$\beta = 5, z_{\mathrm{i}}(0) = 1500$ m, D_n	$\beta = 5, z_{\mathrm{i}}(0) = 500$ m, D_n
Before sunrise	13 m	0 m
Before sunset	1401 m	500 m
Dissipation Time	7.9 hours	7.7 hours
	$\beta = 0.2, z_{\mathrm{i}}(0) = 500$ m, $5D_n$	$\beta = 0.6, z_{\mathrm{i}}(0) = 1000$ m, $5D_n$
Before sunrise	26 m	190 m
Before sunset	211 m	1000 m
Dissipation Time	16.7 hours	5.3 hours
	$\beta = 5, z_{\mathrm{i}}(0) = 1500$ m, $5D_n$	
Before sunrise	330 m	
Before sunset	1500 m	
Dissipation Time	2.8 hours	

Cloud Thickness Evolution

Fig. 3.8 shows the thickness evolution of a cloud with 200 m initial thickness (top) and the resulting surface shortwave radiative fluxes, especially important from the solar forecasting aspect (bottom). The expected dissipation times using Eq. (3.65) and Eq. (3.67), later presented in this section, are tabulated in Table 3.1 for the cases in Fig. 3.8. The initial conditions used for the cases are also shown in Fig. 3.2.

The dashed lines compare the effect of Bowen Ratio under normal subsidence for an initial inversion height of 1500 m. Under these conditions, Eq. (3.65) predicts that the cloud does not dissipate before sunrise, but Eq. (3.67) predicts that the cloud dissipates during the day if $\beta > 0.3$. As expected in the figure only $\beta = 0.2$ does not dissipate. The lines with markers compare the same Bowen Ratio scenarios for a lower initial inversion height of 500 m. Under these conditions, the cloud dissipates at about the same time as for the initial inversion height of 1500 m for $\beta = 0.6$ and $\beta = 5$. Finally, the thick solid lines compare the effect of a strong

subsidence for different initial inversion heights. As expected stronger subsidence decreases cloud thickness. For strong subsidence (-1.875×10^{-5} s^{-1}), Eq. (3.65) predicts that for $z_{\mathrm{i}}(0) > 1050$ m, the cloud dissipates before sunrise and Eq. (3.67) predicts that $z_{\mathrm{i}}(0) = 500$ m and $\beta > 0.16$ dissipates during the day. The results validate the analytically derived conditions.

Dissipation Before Sunrise

The expression for dissipation at t_{sunrise} will be derived to determine the critical initial cloud thickness, h_{crit}. In order for the cloud to dissipate, the initial cloud thickness must be less than h_{crit}. Before sunrise, $u_4 = 0$ and a_1 is negligible compared to b_1 such that:

$$\begin{aligned} h(t) = z_{\mathrm{i}}(0)e^{Dt} - z_{\mathrm{b}}(0) - \frac{b_1(e^{Dt}-1)}{z_{\mathrm{i}}(0)De^{Dt}} &= h(0)e^{Dt} \\ &- (1-e^{Dt})\left(z_{\mathrm{b}}(0) - \frac{b_1}{e^{Dt}Dz_{\mathrm{i}}(0)}\right) \end{aligned} \tag{3.64}$$

Since cloud thickness either monotonically increases or decreases during the night, the critical cloud thickness would dissipate exactly at sunrise. We manipulate Eq. (3.64) to obtain the maximum allowable initial cloud thickness for the dissipation condition to be satisfied:

$$h_{\mathrm{crit}} \leq \left(1 - e^{Dt_{\mathrm{sunrise}}}\right)\left(z_{\mathrm{i}}(0) - \frac{b_1}{e^{Dt}Dz_{\mathrm{i}}(0)}\right) \simeq -t_{\mathrm{sunrise}}\left(z_{\mathrm{i}}(0)D - \frac{b_1}{e^{Dt}z_{\mathrm{i}}(0)}\right) \tag{3.65}$$

We infer the following points from this condition: 1) Deeper boundary layers can dissipate thicker clouds. This comes from the fact that the contribution of the initial inversion height ($z_{\mathrm{i}}(0)$) decreases in time through subsidence (Eq. (3.55)), whereas the initial cloud base height ($z_{\mathrm{b}}(0)$) is not multiplied by a subsidence term in Eq. (3.61). For example, if $\mathrm{T_{srf}}$, $\mathrm{T_{cld}}$, and $\mathrm{T_{sky}}$ radiative temperatures were the same such that the net longwave radiation and related coefficients (a_1, b_1) are zero, the inversion height would still decrease in time due to subsidence, whereas cloud base height would stay constant as shown in Eq. (3.61). Thus, a larger inversion height subsides faster, resulting in more dissipation. The physical mechanism behind this is a faster subsidence rate due to a high inversion height. A faster

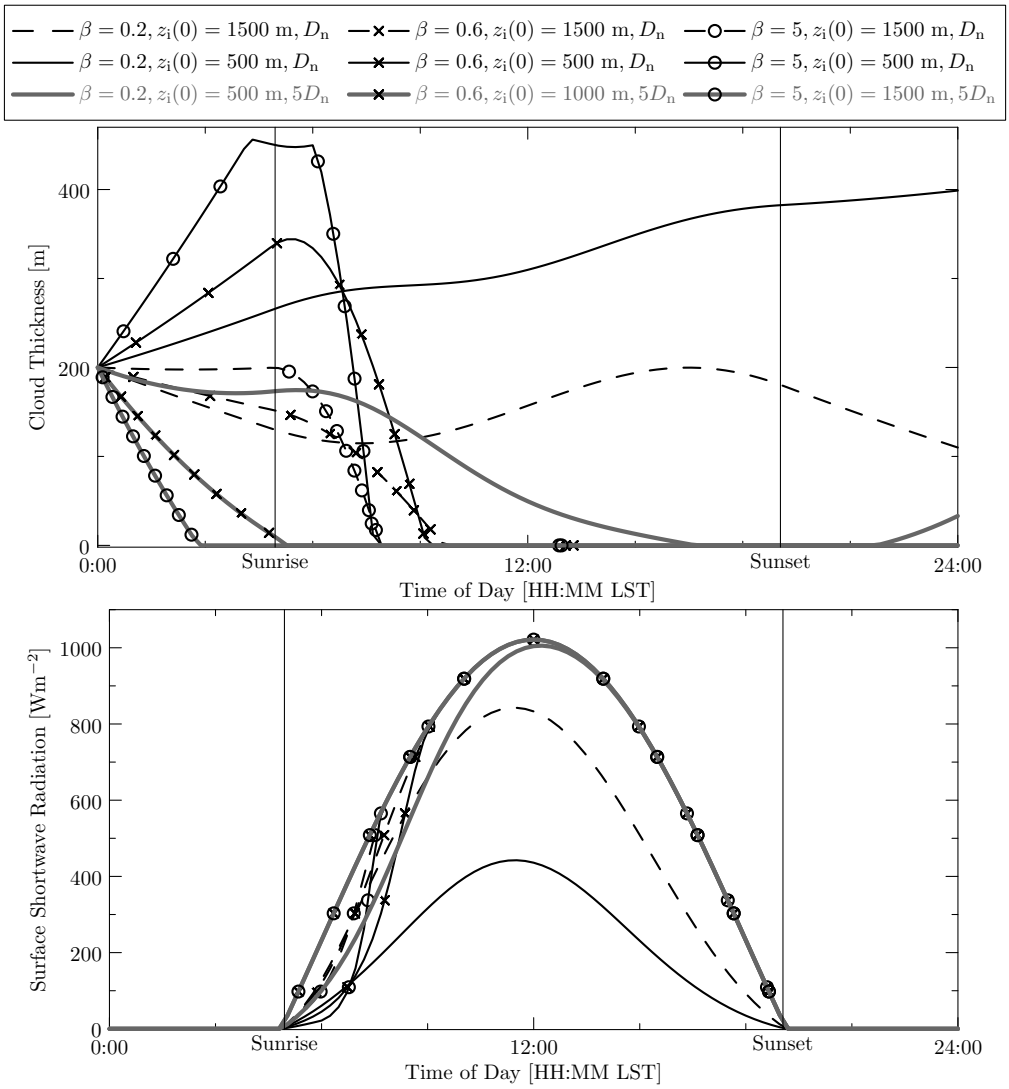

Figure 3.8: Cloud thickness evolution (top) and resulting surface shortwave radiative fluxes (bottom) for different Bowen Ratios, initial inversion heights, and subsidence values. High initial inversion height cases of $z_i = 1500$ m are represented by dashed lines, $z_i = 500$ m cases are represented by solid lines and high subsidence cases are represented by thick lines. $D_n = -3.75 \times 10^{-6}$ s^{-1}, $\mathrm{T_{srf}} = 289$ K, $\mathrm{T_{cld}} = 285$ K, $\mathrm{T_{sky}} = 270$ K, $\zeta_D = 51$ K, $\Delta q_{\mathrm{T,\,i}} = -10$ g kg^{-1}, $\Delta\theta_{\mathrm{l,\,i}} = 10$ K.

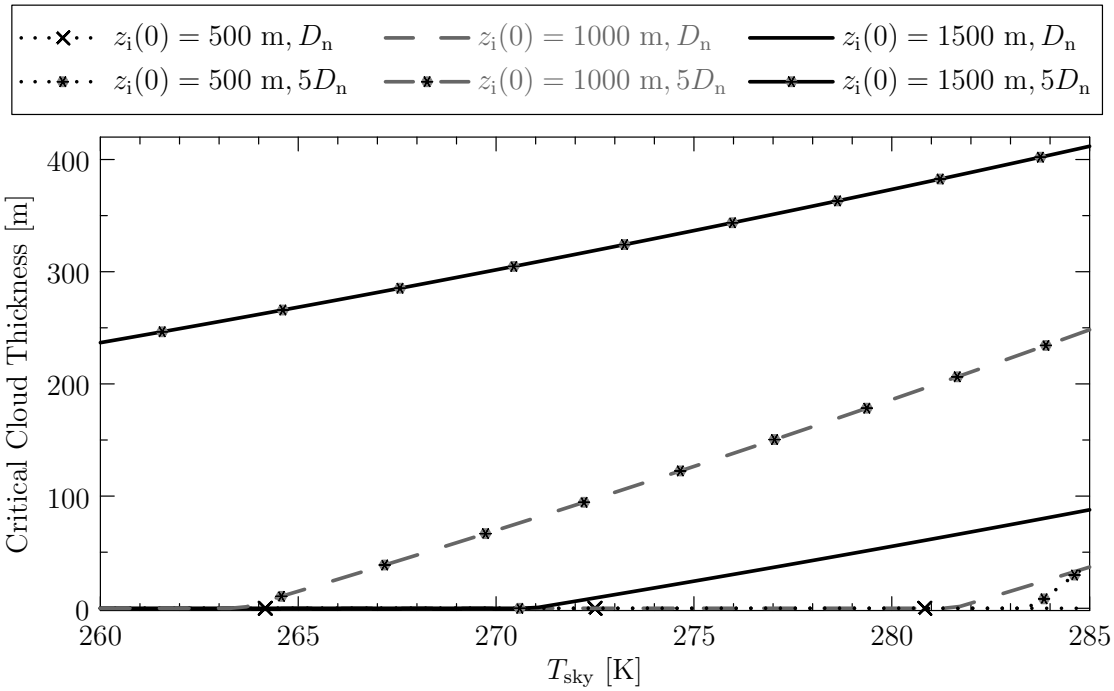

Figure 3.9: Maximum cloud thickness that can be dissipated by sunrise for different T_{sky} radiative temperatures, initial inversion heights and subsidence values. For normal subsidence values of D_n, only a very thin cloud dissipates for the $z_i(0) = 1000$ m and $z_i(0) = 1500$ m cases. A zero result means that the cloud will not dissipate before sunrise for the given conditions. $D_n = -3.75 \times 10^{-6}$ s^{-1}. Other variables are fixed at $\beta = 1, T_{srf} = 289$ K, $T_{cld} = 285$ K, $\zeta_D = 51$ K.

subsidence rate results in a faster decrease in the cloud thickness; 2) Stronger subsidence dissipates thicker clouds. This is expected due to the faster decrease in the inversion height. The physical process is the same as the previous item. As the subsidence divergence increases, the subsidence rate of the cloud top also increases, resulting in a thinner cloud; 3) The cloud base analysis showed that b_1 is proportional to the T_{sky} radiative temperature. Thus, a higher T_{sky} increases the maximum "dissipatable" cloud thickness before sunrise. However, a 1 K increase in T_{sky} only leads to approximately a 7.5 m increase in h_{crit}, thus T_{sky} has a smaller effect compared to the initial inversion height. The maximum dissipatable cloud thickness before sunrise for various T_{sky} radiative temperatures, subsidence values, and initial inversion heights is presented in Figure 3.9.

Dissipation After Sunrise

The second dissipation option materializes through a closing of the gap between inversion height and cloud base height during the day due to a faster increase in cloud base height. Previously, we observed that the dominant daytime term is u_4. Dropping the u_1 terms, the cloud thickness expression can be written as:

$$h(t) = z_{\mathrm{i}}(0)e^{Dt} + a_2 u_4(t) - z_{\mathrm{b}}(0) - \frac{(b_2 + a_2(\delta_1 \Delta q_{\mathrm{T,\,i}} + \delta_2 \Delta\theta_{\mathrm{l,\,i}}))u_4(t)}{z_{\mathrm{i}}(0)e^{Dt} + a_2 u_4(t)} \tag{3.66}$$

The maximum dissipatable or critical initial cloud thickness at sunset is obtained as:

$$h_{\mathrm{crit}} \leq z_{\mathrm{i}}(0)(1 - e^{Dt_{\mathrm{sunset}}}) - a_2 u_4(t_{\mathrm{sunset}}) + \frac{(b_2 + a_2(\delta_1 \Delta q_{\mathrm{T,\,i}} + \delta_2 \Delta\theta_{\mathrm{l,\,i}}))u_4(t_{\mathrm{sunset}})}{z_{\mathrm{i}}(0)e^{Dt_{\mathrm{sunset}}} + a_2 u_4(t_{\mathrm{sunset}})} \tag{3.67}$$

Using $\Delta q_{\mathrm{T,\,i}} = -5$ g kg^{-1}, $\Delta\theta_{\mathrm{l,\,i}} = 10$ K, $\Delta\theta_{\mathrm{v,\,i}} = 10$ K, the critical thickness is obtained as:

$$\begin{aligned} h_{\mathrm{crit}} &= 0.23 z_{\mathrm{i}}(0) + \frac{(13.96 \times 10^6 \text{ m}^2)(0.14 + 0.6e_2)\left(0.4 + 0.32e_1 - \frac{e_1}{\beta+1}\right)}{1.31 z_{\mathrm{i}}(0) + (10^3 \text{ m})(0.14 + 0.6e_2)\left(2.3e_1 - 0.52 - \frac{e_1}{\beta+1}\right)} \\ &- (586 \text{ m})(0.14 + 0.6e_2)\left(2.3e_1 - 0.52 - \frac{e_1}{\beta+1}\right) \end{aligned} \tag{3.68}$$

For the thin cloud case, the critical thickness expression becomes:

$$h_{\mathrm{crit}} = \frac{0.23\left(z_{\mathrm{i}}(0) + (500 \text{ m})\left(1.74 + \frac{1}{\beta+1}\right)\right)^2 + (5.61 \times 10^6 \text{ m}^2)\left(0.72 - \frac{1}{\beta+1}\right)}{z_{\mathrm{i}}(0) + (430 \text{ m})\left(1.72 - \frac{1}{\beta+1}\right)} \tag{3.69}$$

We infer the following points based on this condition: 1) The dominant term is the negative Bowen Ratio dependent term in the numerator of Eq. (3.69). h_{crit} increases with increasing Bowen Ratio. However, the dependence on Bowen Ratio weakens as $1/\beta$ consistent with Section 3.3.1. When the Bowen Ratio increases the positive feedback on the inversion height is weaker compared to the positive feedback on the cloud base height and the combined effect is an increase in h_{crit}. Since the net radiation flux that is converted into turbulent fluxes is constant, the sensitivity to Bowen Ratio decreases for high Bowen Ratios. 2) The dominant term

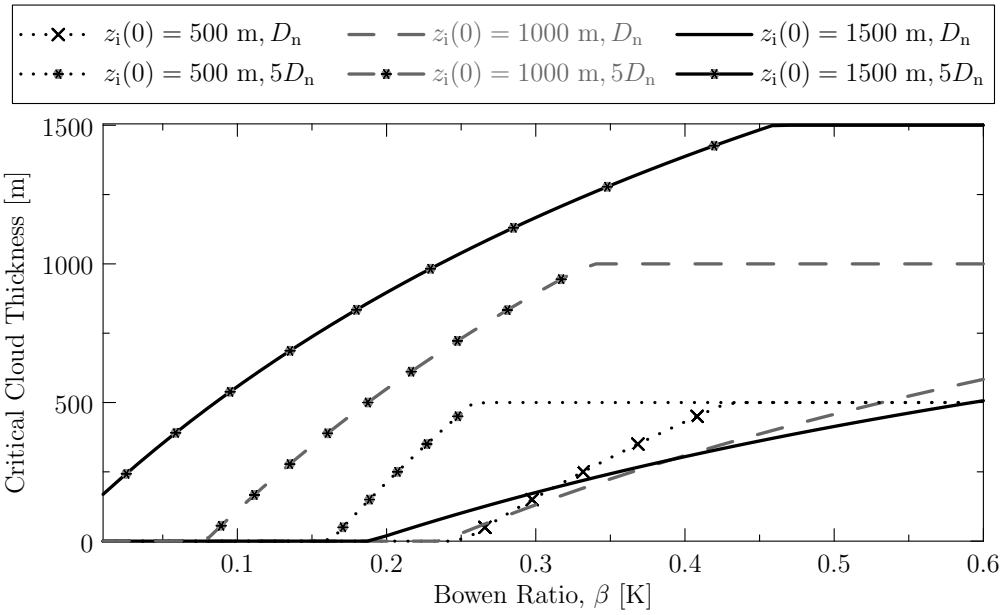

Figure 3.10: Maximum cloud thickness that can be dissipated by sunset for different Bowen Ratios, initial inversion heights and subsidence values. A zero result means that the cloud will not dissipate before sunset for the given conditions. Horizontal lines result when the "dissipatable" cloud thickness reaches the initial inversion height. Parameters are $D_n = -3.75 \times 10^{-6}$ s^{-1}, $\mathrm{T_{srf}} = 289$ K, $\mathrm{T_{cld}} = 285$ K, $\mathrm{T_{sky}} = 270$ K, $\zeta_D = 51$ K, $\Delta q_{\mathrm{T,\,i}} = -5$ g kg^{-1}, $\Delta\theta_{\mathrm{l,\,i}} = 10$ K, $\Delta\theta_{\mathrm{v,\,i}} = 10$ K.

changes sign with Bowen Ratio, making dissipation impossible for small Bowen Ratios and possible for larger Bowen Ratios. Therefore there is a region of the parameter space without dissipation before sunset. The Bowen Ratio threshold that causes dissipation before sunset, is inversely proportional to the initial inversion height. 3) Larger initial inversion heights enhance dissipation (first quadratic term). As explained in the previous section for dissipation before sunrise, the term that contains the initial inversion height decreases exponentially with subsidence, whereas the term with the initial cloud base height persists in time. 4) Larger potential temperature inversion jumps and smaller magnitudes of total moisture inversion jumps enable dissipation as they have been shown in Section 3.3.1 to limit inversion height growth (Eq. (3.67)). 5) Stronger subsidence enables dissipation, resulting directly from the decrease in inversion height. We plot the maximum cloud thickness that can be dissipated during the day for various Bowen Ratios, subsidence values, and initial inversion heights in Figure 3.10. Combining

both night and day results, stronger subsidence, larger inversion height and higher Bowen Ratio enable dissipation and result in higher h_{crit} values.

3.3.4 Extrema Analysis

One of the advantages of an analytic solution is the ability to analyze derivatives for extrema determination. Extrema may be of interest, e.g. in solar forecasting where the thickest cloud conditions determine the maximum required amount of back-up generation. We performed extrema analysis on inversion height and cloud thickness to find out where their minima and maxima occur. To find the extrema points, we take the first and second derivative of the inversion height Eq. (3.55):

$$\frac{dz_{\mathrm{i}}(t)}{dt} = z_{\mathrm{i}}(0)De^{Dt} + a_1e^{Dt} + a_2u_4'(t) \tag{3.70}$$

$$\frac{d^2z_{\mathrm{i}}(t)}{dt^2} = z_{\mathrm{i}}(0)D^2e^{Dt} + a_1De^{Dt} + a_2u_4''(t) = a_2(u_4''(t) - Du_4'(t)) \tag{3.71}$$

The extrema points are obtained by solving the equation:

$$\frac{dz_{\mathrm{i}}(t)}{dt} = 0 \rightarrow \frac{z_{\mathrm{i}}(0)D}{a_2} + \frac{a_1}{a_2} = -\frac{u_4'(t)}{e^{Dt}} \tag{3.72}$$

The terms of the equality are plotted in Figure 3.11. The extrema are close to sunrise and sunset. A greater initial inversion height leads to extrema moving towards mid-day. Furthermore, since $a_1/a_2 \ll 1$, the effect of Bowen Ratio and longwave and shortwave radiation terms is small compared to the initial inversion height.

The second derivative determines whether these points are maxima or minima. We know that $a_2 > 0, D < 0$ and $u_4''(t) \gg Du_4'(t)$. So the sign is determined by the sign of the second derivative of u_4. The sign is positive until mid-day as the cosine of the solar zenith angle is increasing and it is negative after mid-day. This means that the first extremum after sunrise is a minimum and the second extrema before sunset is a maximum. This is an expected result as during night time longwave cooling decreases the inversion height. A minimum occurs when after sunrise net shortwave radiation counteracts longwave cooling and eventually

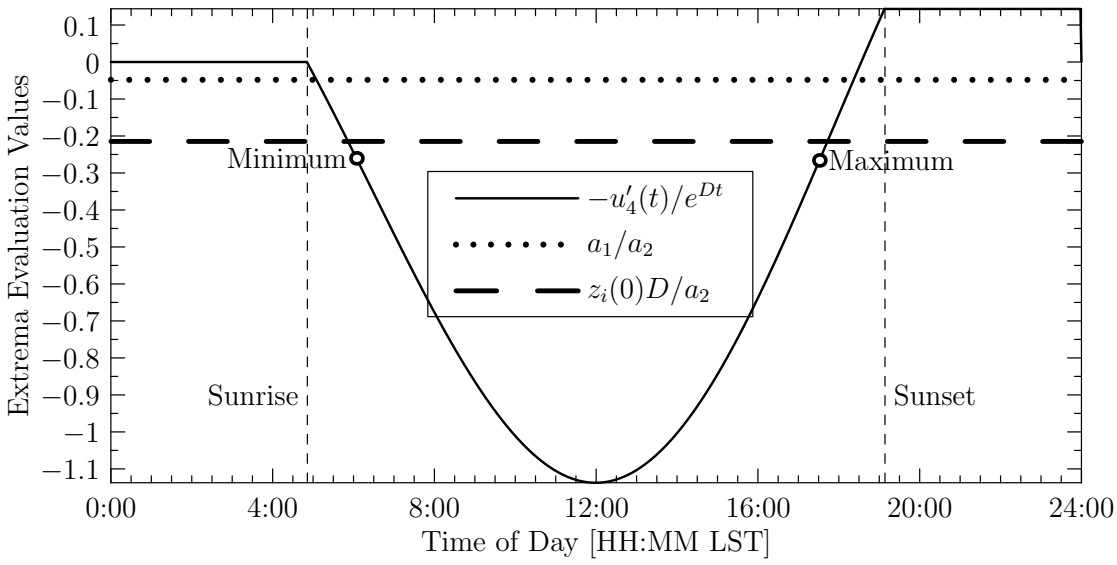

Figure 3.11: Evaluation of the terms in Eq. (3.72) to find the inversion height extrema points.

becomes dominant to increase z_i. Similarly in the afternoon, net shortwave radiation results in an increase in inversion height until longwave cooling dominates closer to sunset.

We continue with the cloud thickness expression. The cloud base height was (Eq. (3.61)):

$$z_\mathrm{b}(t) = \frac{z_\mathrm{i}(t)z_\mathrm{adj} + b_1u_1(t) + b_2u_4(t) + z_\mathrm{i}(0)(z_\mathrm{b}(0) - z_\mathrm{adj})e^{Dt}}{z_\mathrm{i}(t)} \tag{3.73}$$

The cloud thickness is obtained by subtracting cloud base height in Eq. (3.73) from $z_\mathrm{i}(t)$:

$$h(t) = \frac{z_\mathrm{i}^2(t) - z_\mathrm{i}(t)z_\mathrm{adj} - b_1u_1(t) - b_2u_4(t) - z_\mathrm{i}(0)(z_\mathrm{b}(0) - z_\mathrm{adj})e^{Dt}}{z_\mathrm{i}(t)} \tag{3.74}$$

$$= \frac{z_\mathrm{i}^2(t) + bz_\mathrm{i}(t) + c(t)}{z_\mathrm{i}(t)} \tag{3.75}$$

The derivatives are:

$$\frac{dh(t)}{dt} = \left(1 - \frac{c(t)}{z_\mathrm{i}^2}\right)\frac{dz_\mathrm{i}(t)}{dt} + \frac{dc(t)}{dt}\frac{1}{z_\mathrm{i}(t)} = 0 \tag{3.76}$$

$$\frac{d^2h(t)}{dt^2} = \frac{2c(t)}{z_\mathrm{i}(t)^3}\left(\frac{dz_\mathrm{i}(t)}{dt}\right)^2 + \left(1 - \frac{c(t)}{z_\mathrm{i}(t)^2}\right)\frac{d^2z_\mathrm{i}(t)}{dt^2} + \frac{d^2c(t)}{dt^2}\frac{1}{z_\mathrm{i}(t)} - 2\frac{dc(t)}{dt}\frac{1}{z_\mathrm{i}^2(t)}\frac{dz_\mathrm{i}(t)}{dt} \tag{3.77}$$

The cloud thickness derivative contains the inversion height derivative. We expand the inversion height expression from Eq. (3.55) for the first derivative as:

$$\begin{aligned}\frac{dz_{\mathrm{i}}}{dt}z_{\mathrm{i}}^2 = (b_1u_1' + b_2u_2' + b_3u_3' + Dz_{\mathrm{i}}(0)(z_{\mathrm{b}}(0) - z_{\mathrm{adj}})e^{Dt}) \\ \times(a_1u_1 + a_2u_2 + a_3u_3 + z_{\mathrm{i}}(0)e^{Dt}) \\ -(b_1u_1 + b_2u_2 + b_3u_3 + z_{\mathrm{i}}(0)(z_{\mathrm{b}}(0) - z_{\mathrm{adj}})e^{Dt}) \\ \times(a_1u_1' + a_2u_2' + a_3u_3' + Dz_{\mathrm{i}}(0)e^{Dt})\end{aligned} \tag{3.78}$$

Using the fact that $u_1' - Du_1 = 1$, $u_2' - Du_2 = \mu_0$ and $u_3' - Du_3 = \mu_0^2$, the expression becomes:

$$\begin{aligned}\frac{dz_{\mathrm{i}}}{dt} &= \left.\frac{(a_1b_2 - a_2b_1)u_4(t)}{z_{\mathrm{i}}^2}\right|_{t=t_{\mathrm{ext}}} \\ &- \left.\frac{z_{\mathrm{i}}(0)e^{Dt}\left((b_1 + b_2\mu_0(t)) + (a_1 + a_2\mu_0(t))(z_{\mathrm{adj}} - z_{\mathrm{b}}(0))\right)}{z_{\mathrm{i}}^2}\right|_{t=t_{\mathrm{ext}}}\end{aligned} \tag{3.79}$$

Eq. (3.79) states that the cloud thickness extrema points exist when the derivative of the inversion height is equal to the right hand side (RHS) of the expression. We utilize the sensitivity results presented previously in this section for all coefficients to assess the extrema of cloud thickness. During night time for $\mu_0 = u_4 = 0$ the RHS is positive. Therefore, no extremum is present before sunrise as the derivative of the inversion height was shown to be negative.

During daytime for large Bowen Ratios that lead to the dissipation of the cloud before sunset, the RHS has a small negative value close to zero due to the quadratic term in the denominator, $b_2 > 0$ and $a_2 > 0$. This means that the extrema, if they exist, are close to the extrema of the inversion height - right after sunrise and right before sunset - since the inversion height extrema are when the inversion height derivative is zero. Inversion height is increasing during the day, except between sunrise and the inversion height minimum and between the inversion height maximum and sunset. The extremum for cloud thickness must occur during these two intervals when the inversion height decreases and the RHS is negative.

When smaller Bowen Ratios lead to persistence of the cloud, the RHS changes sign during the day from negative to positive. Since the initial sign of

RHS is negative, the first extremum between sunrise and the minimum inversion height still exists, however the other extremum shifts to the interval between the minimum inversion height and maximum inversion height, where the inversion height derivative is positive and matches the sign of the RHS.

We check for cloud thickness minima and maxima conditions for the inversion height extrema points. The sign of the following expression determines the extrema condition:

$$\left(1 - \frac{c(t)}{z_{\mathrm{i}}(t)^2}\right)\frac{d^2 z_{\mathrm{i}}(t)}{dt^2} + \frac{d^2 c(t)}{dt^2}\frac{1}{z_{\mathrm{i}}(t)}$$

The sign depends on the initial inversion height. The sign is the opposite of the second derivative of the inversion height for small initial inversion heights and the same for large initial inversion heights. Therefore for shallow boundary layers, the morning cloud thickness extremum is a maximum and occurs between sunrise and the minimum inversion height and the afternoon extremum is a minimum. For higher boundary layers, the morning cloud thickness extremum is a minimum and the afternoon extremum is a maximum. However, since larger inversion heights were shown to increase h_{crit} in Section 3.3.3, the afternoon maximum may not be observed as the cloud may already have dissipated before the extremum depending on the Bowen Ratio. Two examples are shown in Figure 3.12, where $\beta = 0.2$ and the only difference is the initial inversion height. As expected, the minimum and maximum switch intervals between the two examples.

Combining this extrema result with the inversion height extrema, we have three scenarios for dissipation: 1) Cloud dissipation occurs before the minimum inversion height and then no cloud thickness maximum occurs as e.g. for the high subsidence and $z_{\mathrm{i}}(0) \geq 1000$ m cases in Figure 3.8. 2) For larger initial inversion height, dissipation occurs after sunrise. 3) For small initial inversion height, dissipation occurs after sunrise and before sunset with a maximum after sunrise depending on the Bowen Ratio. Since the extrema analysis can only give the extrema of the cloud thickness and not the values at those points, it is possible that the cloud may dissipate before the minimum.

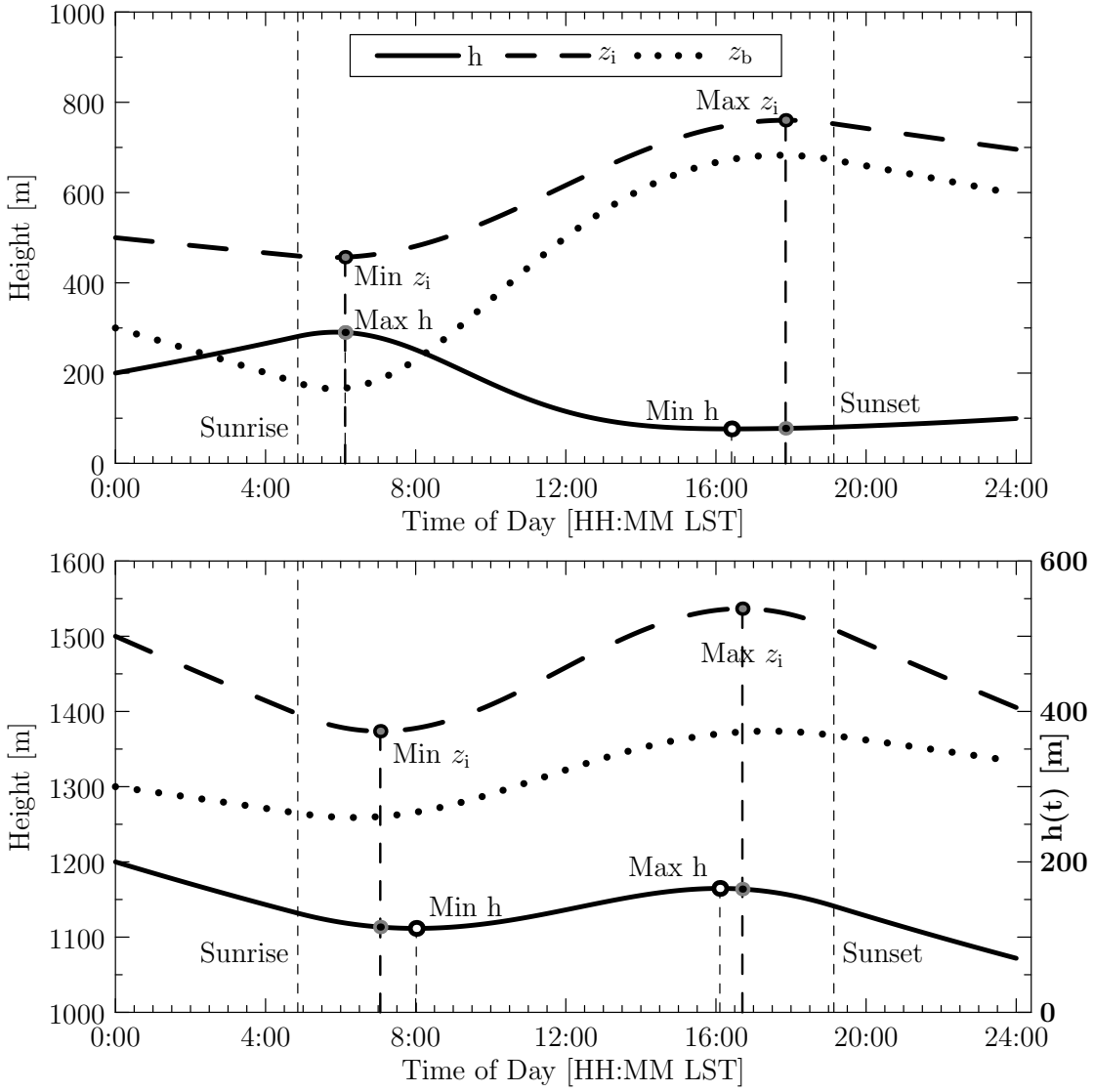

Figure 3.12: Evaluation of the cloud thickness and its extrema values. Both cases have an initial cloud thickness of 200 m, but the top figure has $z_i(0) = 500$ m and the bottom figure has $z_i(0) = 1500$ m. The remaining parameters are the same, i.e. $\beta = 0.2, \mathrm{T_{srf}} = 289$ K, $\mathrm{T_{cld}} = 285$ K, $\mathrm{T_{sky}} = 270$ K, $\zeta_D = 51$ K.

3.4 Error Calculations

3.4.1 Error Calculation Methods and Metrics

We use the root mean square error (RMSE) definition as:

$$\text{RMSE} \triangleq \sqrt{\frac{1}{\text{N}}\sum_{i=1}^{\text{N}}\left(\text{x}_{\text{model}}(i)-\text{x}_{\text{ref}}(i)\right)^2} \tag{3.80}$$

$\text{x}_{\text{model}}(i)$ represents the i^{th} point generated by our model, whereas $\text{x}_{\text{ref}}(i)$ is the i^{th} point associated with a reference (usually the ground truth). The percentage error is defined by normalizing the RMSE by the mean reference value:

$$\%\text{Error} = \frac{\text{RMSE}}{\frac{1}{\text{N}}\sum_{i=1}^{\text{N}}\text{x}_{\text{ref}}(i)} \tag{3.81}$$

This percentage error model is only used for positive valued variables.

Throughout this section, errors are assessed by comparing the results of our approximations with their original forms. For longwave calculations, we use the parameters from [26] and for shortwave calculations we use the parameters from [27]. The errors are calculated numerically over a range of parameter values and then averaged. For inversion height, the interval of $z_{\text{i}} \in [500\text{ m}, 1000\text{ m}]$ with 50 m resolution is used, whereas for the cloud thickness $h \in [50\text{ m}, 400\text{ m}]$ is used. Since optical thickness depends on Γ_l, we use the interval $\Gamma_l \in [0.1\times10^{-6}\text{ m}^{-1}, 2\times10^{-6}\text{ m}^{-1}]$ with a resolution of $10^{-7}]\text{ m}^{-1}$. Longwave radiation depends on the T_{srf}, T_{cld}, and T_{sky} effective radiative temperatures. The standard atmosphere adiabatic lapse rate of -6.5 K m^{-1} allows calculating the T_{cld} and T_{sky} radiative temperatures from the surface temperature. We use the interval $\text{T}_{\text{srf}} \in [285\text{ K}, 295\text{ K}]$ with 1 K resolution. For solar zenith angle calculations, we use daytime with 100 s resolution.

3.4.2 Longwave Error Calculations for the approximations in Eqs. (3.15) and (3.16)

We set $\omega_{\text{lw}} = 0.694$ and $\text{g}_{\text{lw}} = 0.83$ for all longwave calculations. We performed more than 35 million experiments, where we calculated the percentage

error of our approximation in Eq. (3.18) and (3.17) with respect to the original formulation in Eq. (3.16) and (3.15). The maximum RMSE observed is 0.53 and the maximum percentage error is 0.05%, while the mean percentage error is 0.03%. The maximum error is observed for Eq. (3.16), $z_{\mathrm{i}} = 500$ m, $\Gamma_l = 2 \times 10^{-6}$ m^{-1} and $\mathrm{T_{srf}} = 285$ K.

3.4.3 Shortwave Error Calculations for the approximations in Eqs. (3.23) and (3.22)

We set $\omega_{\mathrm{sw}} = 0.993$ and $\mathrm{g_{sw}} = 0.83$ for all shortwave calculations. We calculate α_{sw} and β_{sw} (Eq. 3.19) and compare against Eq. (2.37) and Eq. (2.30), respectively to obtain the error performance. We performed more than 32 million experiments. The resulting mean percentage error is 2%. The percentage error of our approximation at the inversion height in Eq. (3.22) is 6% and the maximum RMSE observed is 43 W m^{-2}. The maximum error is observed for the $z_{\mathrm{i}} = 500$ m, $\Gamma_l = 10^{-6}$ m^{-1} and $z_{\mathrm{b}} = 335$ m case. For the shortwave approximation at the surface in Eq. (3.23), the percentage error is 7% and the maximum RMSE is 44 W m^{-2}. The maximum error is observed for the $z_{\mathrm{i}} = 500$ m, $\Gamma_l = 10^{-6}$ m^{-1} and $z_{\mathrm{b}} = 325$ m case.

3.4.4 Net Radiation Error Calculations for the approximations in Eq. (3.25)

We use the same configurations as in the previous sections 3.4.2, 3.4.3. The mean percentage error of the columnar integral linear approximation in Eq. (3.25) is 6% and the RMSE is 41 W m^{-2}.

3.4.5 Constant Assumption Validations

The first assumption states that the $\mathrm{T_{srf}}$, $\mathrm{T_{cld}}$ and $\mathrm{T_{sky}}$ radiative temperature variations are small compared to the actual temperatures. Assuming a 30 K sinusoidal variation during the day from 265 K to 295 K and back to 265 K, the RMSE of assuming a fixed temperature is only 4.5 K corresponding to less than 2%

error. The errors are amplified to 6% in the black body radiation calculation due to the fourth-order temperature dependence. The second assumption states that similar trends in temperature will decrease the effective error since the equations depend on the difference of the black body radiations. To verify this claim we create a second temperature timeseries at a height of 1 km. Under the standard atmosphere assumption, the lapse rate is -6.5 K km^{-1}] so the second temperature timeseries therefore varies sinusoidally from 256.5 K to 286.5 K instead. The error of the difference of black body radiation drops to 5%. The third assumption states that the net shortwave radiation is greater than the net longwave radiation in the cloud layer during the day. Using the assumptions in the previous example, the average ratio of net shortwave to net longwave during the day is 8.7.

The constant optical depth assumption with τ_{b} calculated once using the initial thickness and then set constant is validated against a model run with a variable (real) optical depth that is solved iteratively at every minute. Different optical depth variation were created through two scenarios with different Bowen Ratios of 0.2 and 1. Furthermore, since the optical depth depends on Γ_l, we analyzed two scenarios with $\Gamma_l = 10^{-7}$ m^{-1} (Figure B1 - top) and $\Gamma_l = 5 \times 10^{-7}$ m^{-1} (Figure B1 - bottom). The results in Figure B1 show that the iterative and constant solutions are close in all Bowen Ratio cases. In the case of $\Gamma_l = 5 \times 10^{-7}$ m^{-1}, the distance between the solutions increase relative to the $\Gamma_l = 10^{-7}$ m^{-1} case. The main reason is that the LWP and the cloud optical depth are 5 times higher, resulting in the optical thickness scale (h_{sw}) that is 5 times smaller. The difference is largest for $\beta = 0.2$, since the cloud does not dissipate within 24 hours and the error accumulates over a longer time.

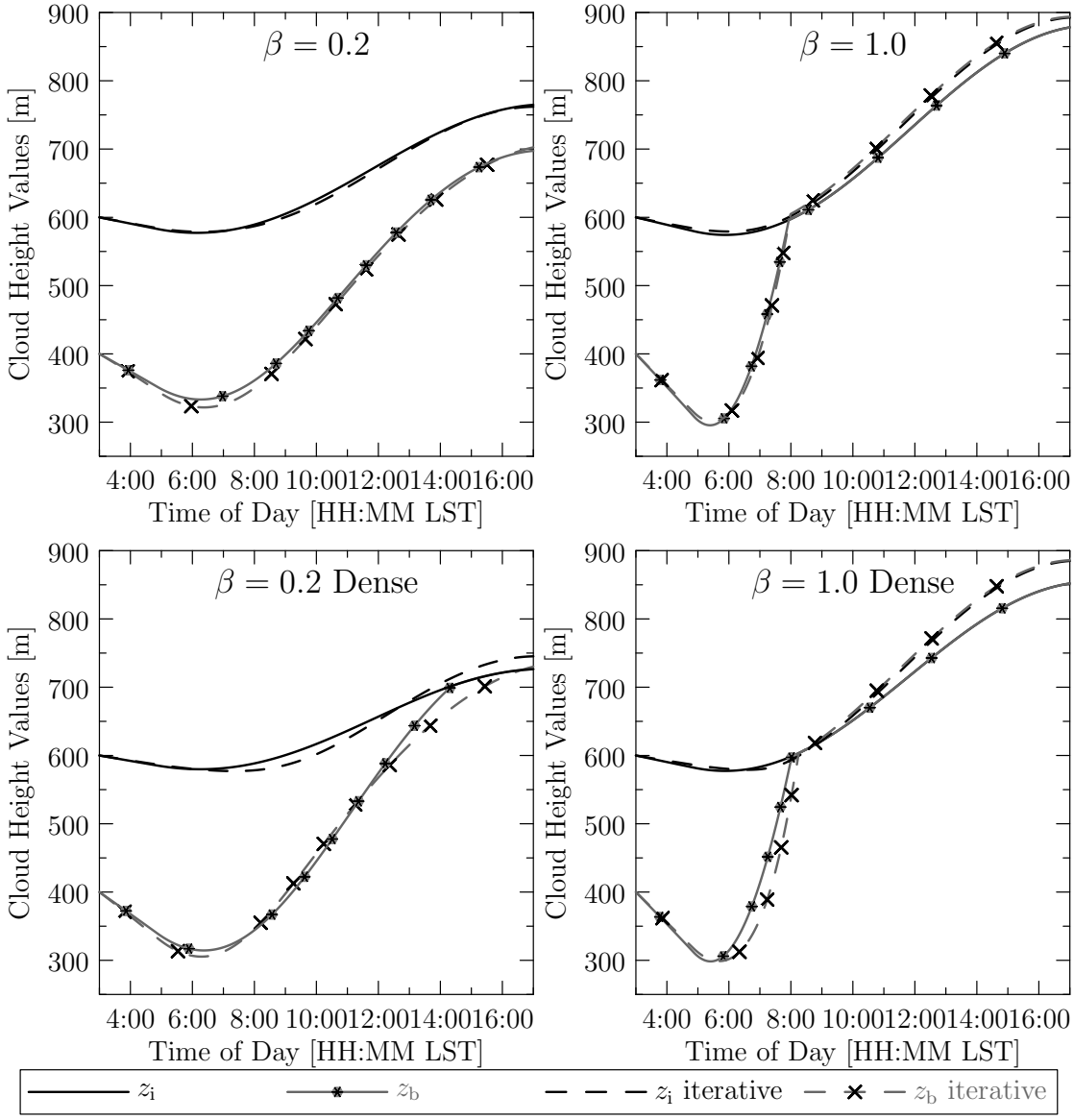

Figure 3.13: Constant and iterative optical depth solution comparison. The constant optical depth solution (solid) follows the iterative optical depth solution (dashed) closely, showing that our constant optical depth assumption is valid. $\Gamma_l = 5 \times 10^{-7}$ m^{-1} for the normal case, and $\Gamma_l = 10^{-7}$ m^{-1} for the dense case. Rest of the simulation parameters are $z_{\rm i}(0) = 600$ m, $z_{\rm b}(0) = 400$ m, $\mathrm{T_{srf}} = 289$ K, $\mathrm{T_{cld}} = 285$ K, $\mathrm{T_{sky}} = 265$ K, $D = -3.75 \times 10^{-6}$ s^{-1}.

3.5 Derivation of u_1, u_2, u_3 functions

We start the solution from $u_1(t)$:

$$u_1(t) = e^{Dt} \int_{t'=0}^{t} e^{-Dt'} dt' \tag{3.82}$$

$$= \frac{e^{Dt} - 1}{D} \tag{3.83}$$

We continue with $u_2(t)$. This function involves the solar zenith angle and can be written in a general form as: $\mu_0(t) = \max\left\{\mu_1 + \mu_2 \cos\left(\frac{t\pi}{H} - \pi\right), 0\right\}$. The solution is as follows:

$$u_2(t) = e^{Dt} \int_{t'=0}^{t} e^{-Dt'} \max\left\{\mu_1 + \mu_2 \cos\left(\frac{t'\pi}{H} - \pi\right), 0\right\} dt' \tag{3.84}$$

Note that the expression in the maximum is a periodic expression. The non-zero region within a day spans from t_1, sunrise, to t_2, sunset. If t is greater than 1 day, then the solar zenith angle expression will be repeated. The general solution for a time t on following days is:

$$\begin{aligned} u_2(t) &= e^{Dt} \left(\int_{t_1}^{t_2} e^{-Dt'} \mu_0(t') dt' + \ldots + \int_{t_1+2nH}^{t} e^{-Dt'} \mu_0(t') dt' \right) \\ &= e^{Dt} \sum_{j=0}^{n-1} e^{-2DHj} \int_{t_1}^{t_2} e^{-Dt'} \mu_0(t') dt' + e^{Dt-2DHn} \int_{t_1}^{t-2nH} e^{-Dt'} \mu_0(t') dt' \\ &= e^{Dt} \left(\frac{1 - e^{-2DHn}}{1 - e^{-2DH}} \right) \int_{t_1}^{t_2} e^{-Dt'} \mu_0(t') dt' + e^{Dt-2DHn} \int_{t_1}^{t-2nH} e^{-Dt'} \mu_0(t') dt' \end{aligned}$$

We start with the solution of the integral with a general bound:

$$\begin{aligned}
\int_{t_1}^{x} e^{Dx-Dt'}\mu_0(t') &= \mu_1 e^{Dx}\int_{t_1}^{x} e^{-Dt'}dt' + \mu_2 e^{Dx}\int_{t_1}^{x} e^{-Dt'}\cos(t'\pi/H-\pi)dt' && (3.85)\\
&= \frac{\mu_1}{D}\left(e^{Dx-Dt_1}-1\right) + \mu_2 e^{Dx}\int_{t'=t_1}^{x}\frac{e^{it'\pi/H-i\pi-Dt'}+e^{-it'\pi/H+i\pi-Dt'}}{2}dt'\\
&= \frac{\mu_1}{D}\left(e^{Dx-Dt_1}-1\right)\\
&+ \mu_2 e^{Dx}\frac{e^{ix\pi/H-i\pi-Dx}-e^{it_1\pi/H-i\pi-Dt_1}}{2i\pi/H-2D}\\
&+ \mu_2 e^{Dx}\frac{e^{-ix\pi/H+i\pi-Dt}-e^{-it_1\pi/H+i\pi-Dt_1}}{-2i\pi/H-2D} && (3.86)\\
&= \mu_2\frac{\pi H^{-1}\sin(x\pi/H-\pi)-D\cos(x\pi/H-\pi)}{D^2+\pi^2H^{-2}}\\
&+ e^{Dx-Dt_1}\frac{\pi H^{-1}\left(\sqrt{\mu_2^2-\mu_1^2}\right)-\mu_1 D}{D^2+\pi^2H^{-2}}\\
&+ \mu_1 D^{-1}e^{Dx-Dt_1}-\mu_1 D^{-1} && (3.87)\\
&= \mu_2\frac{\pi H^{-1}\sin(x\pi/H-\pi)-D\cos(x\pi/H-\pi)}{D^2+\pi^2H^{-2}}\\
&+ e^{Dx-Dt_1}\frac{\pi H^{-1}\left(\sqrt{\mu_2^2-\mu_1^2}\right)+\mu_1 D^{-1}\pi^2H^{-2}}{D^2+\pi^2H^{-2}}-\mu_1 D^{-1} && (3.88)
\end{aligned}$$

Using this result, we construct u_2:

$$\begin{aligned}
u_2(t) &= e^{Dt-Dt_2}\left(\frac{1-e^{-2DHn}}{1-e^{-2DH}}\right)\frac{\pi H^{-1}\left(\sqrt{\mu_2^2-\mu_1^2}\right)-\mu_1 D^{-1}\pi^2H^{-2}}{D^2+\pi^2H^{-2}}\\
&+ e^{Dt-Dt_1}\left(\frac{1-e^{-2DHn}}{1-e^{-2DH}}\right)\frac{\pi H^{-1}\left(\sqrt{\mu_2^2-\mu_1^2}\right)+\mu_1 D^{-1}\pi^2H^{-2}}{D^2+\pi^2H^{-2}}\\
&+ \mu_2\frac{\pi H^{-1}\sin(t\pi/H-\pi)-D\cos(t\pi/H-\pi)}{D^2+\pi^2H^{-2}}\\
&+ e^{Dt-2DHn-Dt_1}\frac{\pi H^{-1}\left(\sqrt{\mu_2^2-\mu_1^2}\right)+\mu_1 D^{-1}\pi^2H^{-2}}{D^2+\pi^2H^{-2}}-\mu_1 D^{-1} \quad (3.89)
\end{aligned}$$

The resulting equation has three components: a constant, an oscillatory component with a periodicity of 24 hours and an exponentially decreasing component, which has subsidence as its exponent. As in the previous component, this means that the exponential term will vanish after roughly 10 days.

We continue with $u_3(t)$. We now deal with the square of the solar zenith angle. Taking the square of the expression, we obtain a very similar expression as before:

$$\begin{aligned}\mu_0^2 &= \mu_1^2 + 2\mu_1\mu_2\cos(t\pi/H-\pi) + \mu_2^2\cos^2(t\pi/H-\pi) \\ &= \left(\mu_1^2+\mu_2^2/2\right) + \left(2\mu_1\mu_2\cos(t\pi/H-\pi)\right) + \left(\mu_2^2/2\right)\cos(2t\pi/H) \quad (3.90)\end{aligned}$$

We start with the solution of the integral with a general bound for μ_0^2:

$$\begin{aligned}&= \left(\mu_1^2+\mu_2^2/2\right)e^{Dx}\int_{t_1}^{x} e^{-Dt'}dt' + 2\mu_1\mu_2 e^{Dx}\int_{t_1}^{x} e^{-Dt'}\cos(t'\pi/H-\pi)dt' \\ &+ \left(\mu_2^2/2\right)e^{Dx}\int_{t_1}^{x} e^{-Dt'}\cos(2t'\pi/H)dt' \quad (3.91) \\ &= \frac{(\mu_1^2-\mu_2^2/2)}{D}\left(e^{Dx-Dt_1}-1\right) + 2\mu_1\mu_2 e^{Dx}\int_{t'=t_1}^{x}\frac{e^{it'\pi/H-i\pi-Dt'}+e^{-it'\pi/H+i\pi-Dt'}}{2}dt' \\ &+ \left(\mu_2^2/2\right)e^{Dx}\int_{t'=t_1}^{x}\frac{e^{2it'\pi/H-Dt'}+e^{-2it'\pi/H-Dt'}}{2}dt' \quad (3.92) \\ &= \frac{(\mu_1^2+\mu_2^2/2)}{D}\left(e^{Dx-Dt_1}-1\right) \\ &+ 2\mu_1\mu_2 e^{Dx}\frac{e^{ix\pi/H-i\pi-Dx}-e^{it_1\pi/H-i\pi-Dt_1}}{2i\pi/H-2D} \\ &+ 2\mu_1\mu_2 e^{Dx}\frac{e^{-ix\pi/H+i\pi-Dt}-e^{-it_1\pi/H+i\pi-Dt_1}}{-2i\pi/H-2D} \\ &+ \left(\mu_2^2/2\right)e^{Dx}\frac{e^{2ix\pi/H-Dx}-e^{2it_1\pi/H-Dt_1}}{4i\pi/H-2D} \\ &+ \left(\mu_2^2/2\right)e^{Dx}\frac{e^{-2ix\pi/H-Dt}-e^{-2it_1\pi/H-Dt_1}}{-4i\pi/H-2D} \quad (3.93)\end{aligned}$$

$$
\begin{aligned}
&= \frac{(\mu_1^2 - \mu_2^2/2)}{D}\left(e^{Dx - Dt_1} - 1\right) \\
&+ 2\mu_1\mu_2 \frac{\pi H^{-1}\sin(x\pi/H - \pi) - D\cos(x\pi/H - \pi)}{D^2 + \pi^2 H^{-2}} \\
&+ 2\mu_1 e^{Dx - Dt_1} \frac{\pi H^{-1}\sqrt{\mu_2^2 - \mu_1^2} - \mu_1 D}{D^2 + \pi^2 H^{-2}} \\
&+ \frac{\mu_2^2}{2} \frac{2\pi H^{-1}\sin(2x\pi/H) - D\cos(2x\pi/H)}{D^2 + 4\pi^2 H^{-2}} \\
&+ e^{Dx - Dt_1} \frac{D(\mu_1^2 - \mu_2^2/2) - 2\mu_1\pi H^{-1}\sqrt{\mu_2^2 - \mu_1^2}}{D^2 + 4\pi^2 H^{-2}}
\end{aligned} \tag{3.94}
$$

Using the respective x values we obtain:

$$
\begin{aligned}
&2\mu_1 \left(\frac{1 - e^{-2DHn}}{1 - e^{-2DH}}\right)\left(e^{Dt - Dt_2}\frac{\pi H^{-1}\sqrt{\mu_2^2 - \mu_1^2} - \mu_1\pi^2 H^{-2}}{D^2 + \pi^2 H^{-2}}\right. \\
&\qquad \left. + e^{Dt - Dt_1}\frac{\pi H^{-1}\sqrt{\mu_2^2 - \mu_1^2} + \mu_1\pi^2 H^{-2}}{D^2 + \pi^2 H^{-2}}\right) \\
&- \left(\frac{1 - e^{-2DHn}}{1 - e^{-2DH}}\right)\left(e^{Dt - Dt_2}\frac{2\pi H^{-1}\mu_1\sqrt{\mu_2^2 - \mu_1^2} + D(\mu_1^2 - \mu_2^2)}{D^2 + 4\pi^2 H^{-2}}\right. \\
&\qquad \left. - e^{Dt - Dt_1}\frac{D(\mu_1^2 - \mu_2^2) - 2\mu_1\pi H^{-1}\sqrt{\mu_2^2 - \mu_1^2}}{D^2 + 4\pi^2 H^{-2}}\right) \\
&\qquad + \frac{(\mu_1^2 - \mu_2^2/2)}{D}\left(e^{Dt - 2DnH - Dt_1} - 1\right) + \\
&\qquad 2\mu_1\mu_2 \frac{\pi H^{-1}\sin(t\pi/H - \pi) - D\cos(t\pi/H - \pi)}{D^2 + \pi^2 H^{-2}} \\
&\qquad + 2\mu_1 e^{Dt - 2DnH - Dt_1}\frac{\pi H^{-1}\sqrt{\mu_2^2 - \mu_1^2} - \mu_1 D}{D^2 + \pi^2 H^{-2}} \\
&\qquad + \frac{\mu_2^2}{2}\frac{2\pi H^{-1}\sin(2t\pi/H) - D\cos(2t\pi/H)}{D^2 + 4\pi^2 H^{-2}} \\
&\qquad + e^{Dt - 2DnH - Dt_1}\frac{D(\mu_1^2 - \mu_2^2/2) - 2\mu_1\pi H^{-1}\sqrt{\mu_2^2 - \mu_1^2}}{D^2 + 4\pi^2 H^{-2}}
\end{aligned} \tag{3.95}
$$

This is similar to the previous result and results in 3 different components: a constant, oscillatory and exponential component with subsidence as its exponent.

This chapter contains material from B. Ozge Akyurek, Jan Kleissl, "Closed-Form Analytic Solution of Cloud Dissipation for a Mixed-Layer Model", AMS Journal of Atmospheric Sciences 2017. The dissertation author was the primary investigator and author of this paper.

Chapter 4

Effect of Large Scale Advection on Cloud Thickness Evolution for a Mixed-Layer Model

4.1 Introduction

In the previous chapter, we have obtained an analytic solution to the cloud mechanisms, which was used to analyze cloud thickening and dissipation. One major assumption was to neglect large scale horizontal advection effects on the solution. The lack of advection results in a closed and isolated system. Our results showed that unless the soil moisture content is high (Bowen Ratio < 0.2), Sc does not persist. However, even though the cloud's isolated trend on the micro-scale is towards dissipation, external effects on the column from the meso-scale can balance this trend, resulting in more persistent Sc behavior, which is more consistent with observations.

Coastal areas are special from the atmospheric standpoint in that they represent an airmass with two different types of surfaces affecting it. On one side, the large cool ocean area creates a cool airmass. Over the land, shortwave radiation causes the land surface to warm up during the day, resulting in a low pressure region. The pressure difference results in a sea-breeze circulation from ocean to land,

advecting cool air from ocean to the land. If the land surface is dry, the advected air from the ocean also moistens the land area. The combined effect of cool and moist air results in increased saturation and enables persistence of clouds. For conditions that would normally lead to a quick dissipation under isolated conditions, advection introduces a counter-balance to the dissipation process. Whether or not advection is strong enough to maintain the cloud over dry lands is an important question an analytic solution can bring an answer to. The advantage of an analytic solution over running multiple numerical simulations is that the analytic solution provides the connections between variables in a transparent way, without the need for analyzing implicit system of equations with complex feedbacks ([30]). Furthermore, as shown in our previous chapter, the analytic solution can extract and explain conditions that are not directly apparent from the underlying equations.

The literature on Sc is divided into micro-scale and meso-scale solutions. Micro-scale works focus on cloud and turbulence dynamics, and either ignore advection completely or include it through static forcings at the boundary. The static forcing method is applied by assuming the neighboring regions to be large and unaffected by the studied column. Even though this method can be used to study the interface between large ocean and land regions, there are two main shortcomings. First, the effect of the neighboring regions is not parametrized, but is only forced numerically. This would make the study of sensitivity to neighboring region conditions, such as surface temperature or turbulent surface fluxes, not possible since we would not be able to discern the cause of the results. Secondly, the neighboring regions are static and will not be affected by the studied column at all, resulting in no feedback that might have altered the neighboring regions. As compared to micro-scale, meso-scale works include advection and interactions between heterogeneous areas, but provide this in tradeoff with turbulence modeling accuracy and result in long computation times. Furthermore, for numerical studies, the numerical solution of advection by itself is an additional challenge as it can easily lead to numerical instability.

In this chapter, we first extend our analytic solution to use a wind speed based surface flux model in order to represent ocean surface types. Then we extend

our analytic solution of cloud thickness to the conserved variables of total water mixing ratio and liquid potential temperature. Using these new analytic solutions as the basis, we propose a novel analytic closed-form solution to a multiple column system coupled through advection, bridging the micro-scale cloud model and the meso-scale advection model for better accuracy.

4.1.1 System Model

The basis of our model is the same vertical column of air with a cloud layer bounded by an inversion layer. Turbulent fluxes in the boundary layer create a well-mixed column. An illustration of a single column along with modeled parameters is shown in Figure 2.1. Due to the well-mixed property, the total water mixing ratio and the liquid potential temperature remain constant with altitude until the inversion layer. The total moisture and liquid potential temperature are driven by the latent and sensible heat fluxes at the surface and entrainment at the inversion. The inversion height is governed by two counteracting variables: a synoptic scale subsidence divergence that reduces the inversion height and entrainment that mixes the turbulent air in the boundary layer with the stratified region above the inversion base height. Subsidence is assumed to be proportional to the inversion height with a constant divergence and entrainment depends on the total buoyancy force in the boundary layer. The cloud base height is the saturation point of the water vapor and depends on the total water content and liquid potential temperature. Together with the inversion height, cloud base height forms the cloud layer. Due to the condensed liquid water within the cloud layer, the cloud acts as an attenuating region for radiation flux in both longwave and shortwave spectra.

4.1.2 Advection Model

The major assumption of this model is that it is isolated from external effects. We propose to extend this model by adding multiple adjacent columns and including large scale horizontal advection interaction between them. We model the advection of the conserved variables of total water mixing ratio (q_{T}) and liquid

potential temperature ($\theta_{\rm l}$), and also the inversion height ($z_{\rm i}$). We assume that the wind speed is constant within the boundary layer, which is necessary to maintain vertical homogeneity of the columns. In other terms, advection is assumed to be constant with height. Furthermore, we assume that the inversion heights of the columns are close to each other, such that there is advection across the entrainment regions, but no mixing of turbulent air of a column with the stratified air above its neighboring column directly. This assumption can easily be supported by the fact that the inversion cap above a large region is continuous. Furthermore, it will be shown that the inversion height of all columns converge to each other quickly even if their initial inversion heights are different. The proposed model is illustrated for two columns in Figure 4.1.

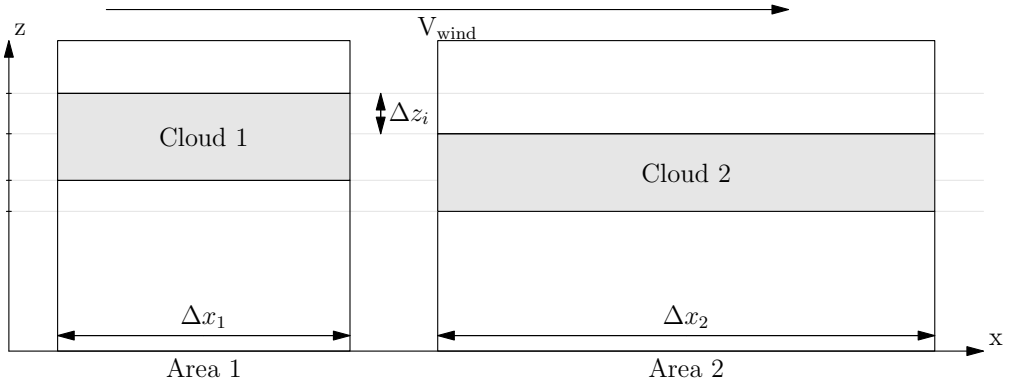

Figure 4.1: Two adjacent air columns coupled through large scale horizontal advection by wind. Each air column is modeled to be well-mixed.

4.1.3 Governing Equations

We start with the budget equations for the conserved variables of total water mixing ratio, $q_{\rm T}$ and liquid potential temperature, $\theta_{\rm l}$. The models and their solutions presented in this section follow our previous derivations ([40]).

$$\frac{d\theta_{\rm l}(t)}{dt} + \theta_{\rm l,\ adv}(t) = -\frac{\partial}{\partial z}\left(\overline{{\rm w}'\theta_{\rm l}'}(z,t) + \frac{{\rm F_{rad}}(z,t)}{{\rm c_p}\rho_{\rm air}}\right) \tag{4.1}$$

$$\frac{dq_{\rm T}(t)}{dt} + q_{\rm T,\ adv}(t) = -\frac{\partial \overline{{\rm w}'q_{\rm T}'}(z,t)}{\partial z} \tag{4.2}$$

$\overline{\mathrm{w}'\theta_\mathrm{l}'}(z,t)$ and $\overline{\mathrm{w}'q_\mathrm{T}'}(z,t)$ represent the liquid potential temperature turbulent flux and total water mixing ratio turbulent flux, respectively. $\mathrm{F_{rad}}$ represents the net radiation flux. Due to the well-mixed assumption, both conserved variables can be assumed to be independent of height. Since the wind speed is assumed to be constant with height within the boundary layer and inversion height is assumed to be constant across multiple columns, the advection terms are also independent of height. This forces the right hand side of the equations to be also independent of height, resulting in a linear height dependency for the partial derivatives. Representing the expressions within the partial derivatives as E and W, respectively, we can derive the full expressions using the boundary conditions at $z = 0$ and $z = z_\mathrm{i}$, as given in [20]:

$$\frac{d\theta_\mathrm{l}}{dt} + \theta_{\mathrm{l,\ adv}} = -\frac{\partial E}{\partial z} \qquad \frac{dq_\mathrm{T}}{dt} + q_{\mathrm{T,\ adv}} = -\frac{\partial W}{\partial z} \tag{4.3}$$

$$E(z) = (1 - z/z_\mathrm{i})E(0) + (z/z_\mathrm{i})E(z_\mathrm{i}) \qquad W(z) = (1 - z/z_\mathrm{i})W(0) + (z/z_\mathrm{i})W(z_\mathrm{i}) \tag{4.4}$$

The boundary conditions at the surface and inversion height are:

$$E(0) = \overline{\mathrm{w}'\theta_\mathrm{l}'}(0,t) + \mathrm{F_{rad}}(0,t)/(\rho_\mathrm{air}\mathrm{c_p}) \tag{4.5}$$

$$E(z_\mathrm{i}) = -w_\mathrm{e}\Delta\theta_{\mathrm{l,\ i}} + \mathrm{F_{rad}}(z_\mathrm{i},t)/(\rho_\mathrm{air}\mathrm{c_p}) \tag{4.6}$$

$$W(0) = \overline{\mathrm{w}'q_\mathrm{T}'}(0,t) \tag{4.7}$$

$$W(z_\mathrm{i}) = -w_\mathrm{e}\Delta q_{\mathrm{T,\ i}} \tag{4.8}$$

The final expressions for θ_l and q_T tendencies are:

$$\frac{d\theta_\mathrm{l}(t)}{dt} + \theta_{\mathrm{l,\ adv}}(t) = \frac{\overline{\mathrm{w}'\theta_\mathrm{l}'}(0,t)}{z_\mathrm{i}(t)} + \frac{\mathrm{F_{rad}}(0,t)}{\rho_\mathrm{air}\mathrm{c_p}z_\mathrm{i}(t)} + \frac{w_\mathrm{e}(t)\Delta\theta_{\mathrm{l,\ i}}}{z_\mathrm{i}(t)} - \frac{\mathrm{F_{rad}}(z_\mathrm{i}(t),t)}{\rho_\mathrm{air}\mathrm{c_p}z_\mathrm{i}(t)} \tag{4.9}$$

$$\frac{dq_\mathrm{T}(t)}{dt} + q_{\mathrm{T,\ adv}}(t) = \frac{\overline{\mathrm{w}'q_\mathrm{T}'}(0,t)}{z_\mathrm{i}(t)} + \frac{w_\mathrm{e}(t)\Delta q_{\mathrm{T,\ i}}}{z_\mathrm{i}(t)} \tag{4.10}$$

The budget equations depend on the net radiation flux, surface fluxes, entrainment, inversion height and advection. We use the surface boundary condition from [30], where the net radiation flux on the surface is converted into the turbulent fluxes with an efficiency of α_srf in a ratio proportional to the Bowen Ratio,

such that:

$$\mathrm{LHF} = \overline{\mathrm{w}'q_{\mathrm{T}}'}(0,t)\rho_{\mathrm{air}}\mathrm{L_v} = -\alpha_{\mathrm{srf}}\frac{1}{\beta+1}\mathrm{F_{rad}}(0,t) \tag{4.11}$$

$$\mathrm{SHF} = \overline{\mathrm{w}'\theta_{\mathrm{l}}'}(0,t)\rho_{\mathrm{air}}\mathrm{c_p} = -\alpha_{\mathrm{srf}}\frac{\beta}{\beta+1}\mathrm{F_{rad}}(0,t) \tag{4.12}$$

For the inversion height, we use the definition from [25] that connects the inversion height tendency to entrainment and subsidence, where D is the subsidence divergence, assumed to be constant:

$$\frac{dz_{\mathrm{i}}}{dt} = w_{\mathrm{e}} + Dz_{\mathrm{i}} - z_{\mathrm{i,\ adv}} \tag{4.13}$$

We use the entrainment closure in [41] to express entrainment as the total buoyancy within the boundary layer, which can in turn be represented in terms of the net radiation flux. With mathematical manipulation, the advection equations can be written in the same form:

$$\frac{d(\theta_{\mathrm{l}}(t)z_{\mathrm{i}}(t))}{dt} - D(\theta_{\mathrm{l}}(t)z_{\mathrm{i}}(t)) + (\theta_{\mathrm{l}}(t)z_{\mathrm{i}}(t))_{\mathrm{adv}} = \mathcal{T}(\mathrm{F_{rad}}(t)) \tag{4.14}$$

$$\frac{d(q_{\mathrm{T}}(t)z_{\mathrm{i}}(t))}{dt} - D(q_{\mathrm{T}}(t)z_{\mathrm{i}}(t)) + (q_{\mathrm{T}}(t)z_{\mathrm{i}}(t))_{\mathrm{adv}} = \mathcal{Q}(\mathrm{F_{rad}}(t)) \tag{4.15}$$

$$\frac{d(z_{\mathrm{i}}(t))}{dt} - D(z_{\mathrm{i}}(t)) + (z_{\mathrm{i,\ adv}}(t)) = \mathcal{Z}(\mathrm{F_{rad}}(t)) \tag{4.16}$$

Note that the differential form of all three equalities are the same except for a different dependence on the net radiation terms, as shown on the right hand side of the equations represented by the calligraphic letters. This form is utilized in the next section to obtain a closed-form analytic solution when horizontal advection is present in the system. Before we proceed with the advection solution, we extend our model to include a wind speed based surface flux model to represent the ocean surface.

4.1.4 Analytic Solution for an Ocean Surface Model

The previous chapter defines the surface fluxes using a Bowen Ratio relation to the net surface radiation flux. Although this model is beneficial in understanding the sensitivity of the cloud to the land soil moisture, it is insufficient in modeling

the surface of the ocean. The surface fluxes are not linearly dependent on the surface net radiation flux and are generally lower in magnitude over the ocean due to its higher heat capacity, relative to land. Since we are investigating the effect of multiple columns on each other, including the ocean for a coastal area, we need to obtain the analytic solution for a surface model more appropriate for an ocean surface.

We utilize the bulk aerodynamic formulas in [37] to model the sensible and latent heat fluxes as:

$$\mathrm{LHF} = \mathrm{L_v}\rho_{\mathrm{air}} C_T V (q_{\mathrm{T,\,s}} - q_{\mathrm{T}}) \tag{4.17}$$

$$\mathrm{SHF} = \mathrm{c_p}\rho_{\mathrm{air}} C_T V (\theta_{\mathrm{l,\,s}} - \theta_{\mathrm{l}}) \tag{4.18}$$

$$C_T \triangleq 0.001 V (1 + 0.07 V) \tag{4.19}$$

C_T is the transfer coefficient ([42]), V is the 10 m wind speed, $q_{\mathrm{T,\,s}}$ is the saturation mixing ratio and $\theta_{\mathrm{l,\,s}}$ is the saturation liquid potential temperature. Substituting into Eq. (2.14) and Eq. (2.15):

$$\frac{d\theta_{\mathrm{l}}(t)}{dt} + \theta_{\mathrm{l,\,adv}}(t) = \frac{C_T V(\theta_{\mathrm{l,\,s}} - \theta_{\mathrm{l}})}{z_{\mathrm{i}}(t)} + \frac{\mathrm{F_{rad}}(0,t) - \mathrm{F_{rad}}(z_{\mathrm{i}}(t),t)}{\rho_{\mathrm{air}}\mathrm{c_p} z_{\mathrm{i}}(t)} + \frac{w_{\mathrm{e}}(t)\Delta\theta_{\mathrm{l,\,i}}}{z_{\mathrm{i}}(t)} \tag{4.20}$$

$$\frac{dq_{\mathrm{T}}(t)}{dt} + q_{\mathrm{T,\,adv}}(t) = \frac{C_T V(q_{\mathrm{T,\,s}} - q_{\mathrm{T}})}{z_{\mathrm{i}}(t)} + \frac{w_{\mathrm{e}}(t)\Delta q_{\mathrm{T,\,i}}}{z_{\mathrm{i}}(t)} \tag{4.21}$$

Since SHFand LHFdon't vary strongly in time, we assume them to be constant. Through algebraic manipulation, we can convert Eq. (2.14) and Eq. (4.21) to the same form as in Eq. (4.14) and Eq. (4.15), respectively. The main difference between the solution of the two turbulent surface flux models is that the Bowen Ratio based model adds surface net radiation terms to $\mathcal{T}$ and $\mathcal{Q}$, whereas the aerodynamic formula adds a constant term.

To solve the differential functions, we utilize the approximations in our previous chapter. We can divide the right hand side of all equations, $\mathcal{T}$, $\mathcal{Q}$ and $\mathcal{Z}$, into three groups: 1) a constant term involving longwave and surface flux terms, 2) a solar zenith angle dependent term, involving entrainment and net radiation expressions in θ_{l}, 3) square of solar zenith angle dependent term. If advection is neglected, each term has a closed-form analytic solution. Next, we introduce these functions.

4.1.5 Analytic Function Definitions

Our analytic solution utilizes three functional forms to represent the solution of a differential equation that arises very frequently throughout this dissertation:

$$\frac{dX(t)}{dt} - D \cdot X(t) = \mathcal{X}(t) \tag{4.22}$$

The general solution can be obtained using the following integral:

$$X(t) = \exp(Dt') \int_{t'=0}^{t'=t} \exp(-Dt')\mathcal{X}(t')dt' \tag{4.23}$$

As described in the previous section, the right hand side of Eq. (4.22) has three forms of time-dependent functions for all differential equations, where only the coefficients of these functions differ across variables. These forms are 1) a constant value, 2) a μ_0 term and 3) a μ_0^2 term. μ_0 is the cosine of the solar zenith angle. We define three functions to represent the solutions to these terms:

$$\frac{du_1(t)}{dt} - Du_1 = 1, \qquad \frac{du_2(t)}{dt} - Du_2 = \mu_0(t), \qquad \frac{du_3(t)}{dt} - Du_3 = \mu_0^2(t) \tag{4.24}$$

The solution to all variables, when advection is omitted, can be written as a linear combination of the three u functions. However, we need to define a modified version of this function to cover the new differential equations that arise with advection. We use a second parameter, shown by H, to represent a general D value, instead of the specific subsidence divergence and we add a second index, shown by N, to represent a multiple-integral solution instead of the current single integral one:

$$u_{1,N}(t,H) = \exp(Ht) \int_{t'=0}^{t} \int_{t''=0}^{t'} (\ldots) \int_{t^{(N)}=0}^{t^{(N-1)}} \exp(-Ht^{(N)})dt^{(N)} \tag{4.25}$$

$$u_{2,N}(t,H) = \exp(Ht) \int_{t'=0}^{t} \int_{t''=0}^{t'} (\ldots) \int_{t^{(N)}=0}^{t^{(N-1)}} \exp(-Ht^{(N)})\mu_0(t^{(N)})dt^{(N)} \tag{4.26}$$

$$u_{3,N}(t,H) = \exp(Ht) \int_{t'=0}^{t} \int_{t''=0}^{t'} (\ldots) \int_{t^{(N)}=0}^{t^{(N-1)}} \exp(-Ht^{(N)})\mu_0^2(t^{(N)})dt^{(N)} \tag{4.27}$$

t', t'' and $t^{(i)}$ are all used to represent temporal integration variables. All integrals are bounded between zero and the previous integration variable. The first integral is taken until the actual time, t. The shape and importance of each function are explained in detail in the next section.

4.2 Analytic Solution with Large Scale Horizontal Advection

In this section, we derive the analytic solution of cloud evolution for a multiple column system coupled through advection. To do this, we start with the simple case of two columns to understand the main interaction due to advection. Then, we extend this into multiple columns to represent a more diverse area. Using the multi column general solution, we take the limit of the number of columns to infinity, while reducing the column sizes to infinitesimal to obtain a continuous domain solution.

4.2.1 The Advection Interactions Between Two Columns

We start by defining two horizontally adjacent columns indexed in ascending order. Since the format of Eq. (4.14), (4.15) and Eq. (4.16) are the same, we will use γ_i as a general variable for column i for notational simplicity. The general differential equation format to be solved becomes:

$$\frac{d\gamma_i}{dt} - D\gamma_i + \gamma_{i,adv} = \mathcal{G}(t) \tag{4.28}$$

The horizontal advection component is defined as:

$$\gamma_{adv} = \overrightarrow{V} \cdot \nabla\gamma = V_x \frac{\partial\gamma}{\partial x} + V_y \frac{\partial\gamma}{\partial y} \tag{4.29}$$

V_x and V_y designate the components of the wind speed, respectively. For two columns, divided as *ocean* and *land*, the advection terms can be explicitly written using upstream difference finite approximation. We only consider the x direction, defined as a normal to the coastline, in our solution, neglecting Coriolis effect and

the orthogonal y direction pressure differences:

$$\gamma_{\text{land, adv}} = \frac{V_x}{\Delta x_{\text{land}}}(\gamma_{\text{land}} - \gamma_{\text{ocean}}) \tag{4.30}$$

Δx is the horizontal distance between the column boundaries. The ocean column is a large area with mostly horizontally homogeneous structure. As a result, the ocean column advection is very small and is approximated as zero. The land column stretches from the edge of the ocean into inland. We define an advection divergence term, similar to the subsidence divergence term, as $D_{\text{adv}} = V_x/\Delta x$. Substituting the advection expressions back into the original equations results in a system of differential equations:

$$\frac{d\gamma_{\text{ocean}}}{dt} - D\gamma_{\text{ocean}} = \mathcal{G}_{ocean} \tag{4.31}$$

$$\frac{d\gamma_{\text{land}}}{dt} - D\gamma_{\text{land}} + D_{\text{adv, land}}\gamma_{\text{land}} - D_{\text{adv, land}}\gamma_{\text{ocean}} = \mathcal{G}_{land} \tag{4.32}$$

Since there is a single advection term, we denote $D_{\text{adv}} = D_{\text{adv, land}}$ for convenience. To solve the system of differential equations, we utilize the Laplace transform of both equations and convert into matrix form. We use s to represent the Laplace variable:

$$\begin{vmatrix} s - D & 0 \\ -D_{\text{adv}} & s - D + D_{\text{adv}} \end{vmatrix} \begin{vmatrix} \gamma_{\text{ocean}} \\ \gamma_{\text{land}} \end{vmatrix} = \begin{vmatrix} \mathcal{G}_{ocean}(s) + \gamma_{\text{ocean}}(0) \\ \mathcal{G}_{land}(s) + \gamma_{\text{land}}(0) \end{vmatrix} \tag{4.33}$$

Substituting the ocean component:

$$(s - D + D_{\text{adv}})\,\gamma_{\text{land}} = D_{\text{adv}}\frac{(\mathcal{G}_{ocean}(s) + \gamma_{\text{ocean}}(0))}{s - D} + (\mathcal{G}_{land}(s) + \gamma_{\text{land}}(0)) \tag{4.34}$$

Using partial fraction expansion:

$$\gamma_{\text{ocean}} = \frac{(\mathcal{G}_{ocean}(s) + \gamma_{\text{ocean}}(0))}{s - D} \tag{4.35}$$

$$\gamma_{\text{land}} = \frac{(\mathcal{G}_{land}(s) + \gamma_{\text{land}}(0))}{s - D} \tag{4.36}$$

$$+ \quad (\mathcal{G}_{ocean}(s) - \mathcal{G}_{land}(s) + (\gamma_{\text{ocean}}(0) - \gamma_{\text{land}}(0)))\left(\frac{1}{s - D} - \frac{1}{s - D + D_{\text{adv}}}\right)$$

To understand what the individual components represent, we write out the uncoupled case ($D_{\text{adv}} = 0$) for both columns:

$$\gamma_{\text{ocean}} = \frac{(\mathcal{G}_{ocean}(s) + \gamma_{\text{ocean}}(0))}{s - D}, \qquad \gamma_{\text{land}} = \frac{(\mathcal{G}_{land}(s) + \gamma_{\text{land}}(0))}{s - D} \tag{4.37}$$

It can be seen that the first term in the land advection solution is the uncoupled solution of the ocean column. The rest of the terms is the difference between the land and ocean solutions evaluated with a virtual subsidence divergence value of $D - D_{\text{adv}}$. This is the same uncoupled solution, with the difference of using $D - D_{\text{adv}}$ as the subsidence divergence term, instead of just D.

To represent this solution back in time-domain, we use the three u functions introduced in Section 4.1.5. The uncoupled solutions are obtained as:

$$\begin{aligned} \gamma_{\text{ocean}}(t) &= \gamma_{\text{ocean}}(0)e^{Dt} + \mathcal{G}_{ocean,1}u_1(t,D) \\ &+ \mathcal{G}_{ocean,2}u_2(t,D) + \mathcal{G}_{ocean,3}u_3(t,D) \qquad (4.38) \\ \gamma_{\text{land}}(t) &= \gamma_{\text{land}}(0)e^{Dt} + \mathcal{G}_{land,1}u_1(t,D) \\ &+ \mathcal{G}_{land,2}u_2(t,D) + \mathcal{G}_{land,3}u_3(t,D) \qquad (4.39) \end{aligned}$$

Therefore, the coupled cases are solved as:

$$\begin{aligned} \gamma_{\text{ocean}}(t) &= \gamma_{\text{ocean}}(0)e^{Dt} + \mathcal{G}_{ocean,1}u_1(t,D) + \mathcal{G}_{ocean,2}u_2(t,D) \\ &+ \mathcal{G}_{ocean,3}u_3(t,D) \qquad (4.40) \\ \gamma_{\text{land}}(t) &= \gamma_{\text{land}}(0)e^{Dt} + \mathcal{G}_{land,1}u_1(t,D) + \mathcal{G}_{land,2}u_2(t,D) + \mathcal{G}_{land,3}u_3(t,D) \\ &+ ((\gamma_{\text{ocean}}(0) - \gamma_{\text{land}}(0))\,(\exp(Dt) - \exp((D - D_{\text{adv}})t)) \\ &+ (\mathcal{G}_{ocean,1} - \mathcal{G}_{land,1})(u_1(t,D) - u_1(t, D - D_{\text{adv}})) \\ &+ (\mathcal{G}_{ocean,2} - \mathcal{G}_{land,2})(u_2(t,D) - u_2(t, D - D_{\text{adv}})) \\ &+ (\mathcal{G}_{ocean,3} - \mathcal{G}_{land,3})(u_3(t,D) - u_3(t, D - D_{\text{adv}})) \qquad (4.41) \end{aligned}$$

When the wind speed is low, the solution converges to the advection-free land solution as the columns decouple. Therefore, the main determining factor is how the u functions changed with the $D - D_{\text{adv}}$ value and therefore the wind speed. An important remark here is that the subsidence divergence, D, is very small compared to D_{adv} values for normal wind speeds. For example, for $D = -3.75 \times 10^{-6}$ s^{-1} and a 10 km land column, a wind speed of only -3.75 cm s^{-1} is enough for $D_{\text{adv}} = D$. Therefore, D can be neglected when D_{adv} is present in the u functions. Furthermore, the u functions are inversely proportional to their D input. This means that a strong wind speed will lead the $u(t, D - D_{\text{adv}})$ terms

to converge to zero very quickly. If this happens, the solution of the coupled land column converges to the solution of the ocean column. To show this, all three u functions have been plotted for 24-hours using wind speeds ranging from no-wind to 5 m s^{-1} in Figure 4.2.

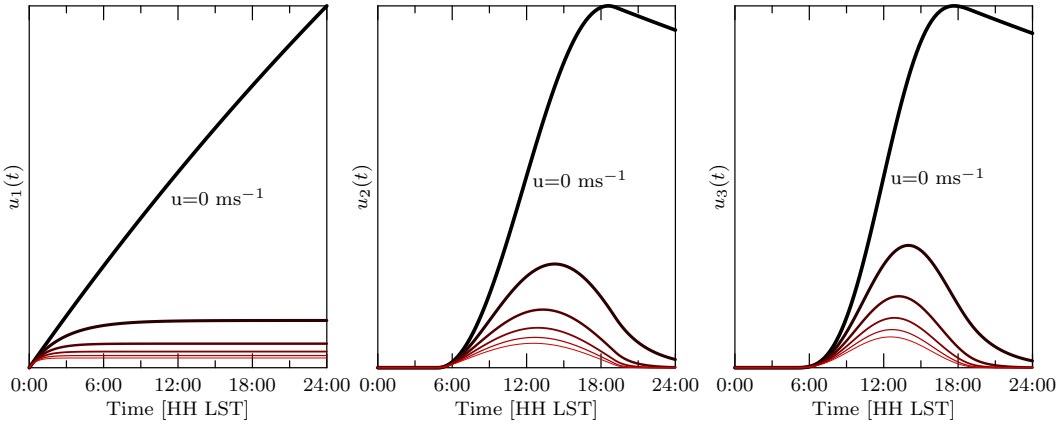

Figure 4.2: Effect of wind speed on the u functions. The top line is the no-wind case and each line represent a 1 m s^{-1} increment in wind speed as we go down from the no-wind case. The figure consists of three subplots of the three u functions. In each subplot, we have plotted 6 lines with wind speeds ranging from no-wind to 5 m s^{-1} with 1 m s^{-1} increments. The top lines in all plots are the no-wind cases and the wind speed increases in order as we go down. Even for a 1 m s^{-1} wind speed, the value of the u functions are remarkably smaller than the original no-wind values.

Even for a wind speed of 1 m s^{-1}, it can be observed that the resulting u-function values are much less than the original no-wind case. Since the coupled land column solution consists of a difference between the no-wind and with-wind u functions, the latter term will quickly diminish for a strong wind and the solution will converge to the solution of the ocean column. This underlines that the ocean column has a drastic effect on the coupled land column.

To show the effect on the actual cloud variables, we created two columns based on the initial conditions from the CGILS experiment ([38]). Both columns are verified against UCLA Large Eddy Simulations (LES) ([29]) using the same initial conditions. The ocean column is represented by an ocean surface model with LHFand SHFat 80 Wm^{-2} and 5 Wm^{-2}, respectively. The land column is represented by a Bowen Ratio based surface model, where the Bowen Ratio is set to

1. The land column size is 10 km and the ocean column is not affected by the land. Wind speed is increased from 0 to 3 m s^{-1} with 0.5 m s^{-1} increments. The results for inversion height, total water mixing ratio and liquid potential temperature are shown in Figure 4.3.

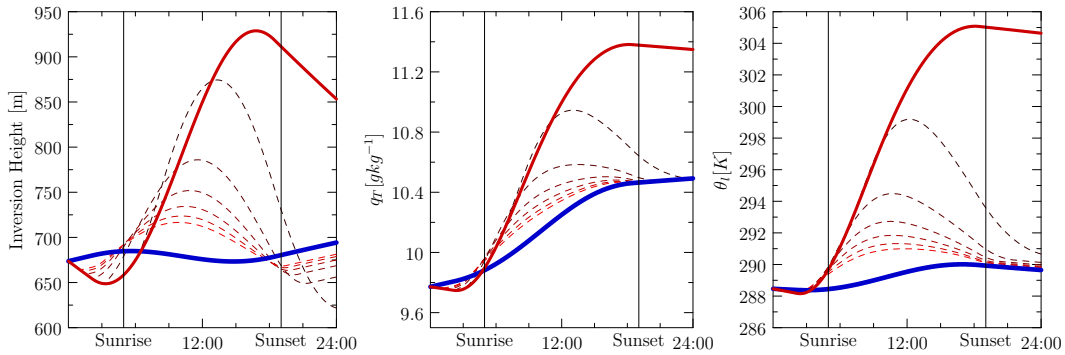

Figure 4.3: Effect of wind speed on a coupled two column setup. The thick red and blue curves represent the uncoupled land and ocean solutions. respectively. Each dashed curve is the coupled land result, where wind speed is increased with 0.5 m s^{-1} steps.

When there is no wind speed, both columns are decoupled and we observe the advection-free results. Ocean column is unaffected due to its large column size and homogeneous structure, and dominates the land column of size 10 km. The 3 dashed curves closest to the ocean results are the 2, 2.5 and 3 m s^{-1} results, which are very close to the ocean results. This is expected from our solution, since even a small wind speed of 0.75 m s^{-1} is strong enough create an effect 20x greater than the subsidence for a 10 km column, since $D_{\text{adv}} = 20D$. It can greatly alter the land column results and converge them closer to the ocean results. A wind speed greater than 1.5 m s^{-1}, as shown by the 3 dashed curves closest to the ocean, is enough to make the land column converge close to the ocean results, showing the importance of advection.

Finally, to connect these results to the actual physical variables, we investigate how the three advection terms of z_{i}, q_{T} and θ_{l} affect the inversion height and cloud base height terms. We use Eq. (2.14) and Eq. (2.15) with the advection terms to obtain the inversion height expression. Through algebraic manipulation, we can show that both entrainment and subsidence are independent of the advection of

q_{T} and θ_{l} (see Section 4.6.1). This means that inversion height is only affected by its own advection term between the columns ($z_{\mathrm{i,\ adv}}$) and any change in q_{T} and θ_{l} due to their respective advection, $q_{\mathrm{T,\ adv}}$ and $\theta_{\mathrm{l,\ adv}}$, has no direct effect on z_{i}.

For cloud base height, since it directly depends on the conserved variables, there is a direct connection to the advection terms of $q_{\mathrm{T,\ adv}}$ and $\theta_{\mathrm{l,\ adv}}$ (see Section 4.6.2). As a result the cloud thickness is affected by the inversion height advection and by the total moisture and liquid potential temperature advection. Before going into more detailed sensitivity analysis, we generalize the two column solution to multiple columns in the next section.

4.2.2 Generalization to Multiple Columns

We extend our initial case of two columns into a more generalized formulation for multiple columns. This way, more diverse cases can be studied to represent more complex scenarios. For any variable γ, let γ_i be its value for the i^{th} column on the x axis. The first column is used to represent the ocean, but from the algebraic perspective, we name it column 1 for unified representation. Using upstream finite difference, the resulting equation can be written as:

$$\frac{d\gamma_x}{dt} - D\gamma_x = \mathcal{G}_x(t) - \frac{V_x}{\Delta x}\left(\gamma_x - \gamma_{x-1}\right), \qquad \frac{d\gamma_1}{dt} - D\gamma_1 = \mathcal{G}_1(t) \tag{4.42}$$

Taking the Laplace transform of all equations as in the two column case:

$$\gamma_x(s - D + D_{adv,x}) - \gamma_x(0) = \mathcal{G}_x(s) + D_{adv,x}\gamma_{x-1} \tag{4.43}$$

We can combine all equations into matrix form as:

$$Ax = b \tag{4.44}$$

$$A = \begin{pmatrix} s - D & 0 & 0 & 0 & \dots \\ -D_{\mathrm{adv}} & s - D + D_{\mathrm{adv}} & 0 & 0 & \dots \\ \dots & -D_{\mathrm{adv}} & s - D + D_{\mathrm{adv}} & 0 & \dots \\ 0 & \dots & 0 & -D_{\mathrm{adv}} & s - D + D_{\mathrm{adv}} \end{pmatrix} \tag{4.45}$$

$$x = \begin{pmatrix} \gamma_1 \\ \vdots \\ \gamma_N \end{pmatrix}, \qquad b = \begin{pmatrix} \mathcal{G}_1 + \gamma_1(0) \\ \vdots \\ \mathcal{G}_N + \gamma_N(0) \end{pmatrix} \tag{4.46}$$

This is a lower triangular matrix and can further be manipulated as:

$$\begin{pmatrix} s-D \\ s-D+D_{\text{adv}} \\ \vdots \\ s-D+D_{\text{adv}} \end{pmatrix} \begin{pmatrix} \gamma_1 \\ \vdots \\ \gamma_N \end{pmatrix} = \begin{pmatrix} \mathcal{G}_1+\gamma_1(0) \\ \vdots \\ \mathcal{G}_N+\gamma_N(0) \end{pmatrix} + D_{\text{adv}} \begin{pmatrix} 0 \\ \gamma_1 \\ \vdots \\ \gamma_{N-1} \end{pmatrix} \tag{4.47}$$

The resulting system of equations has a recursive form with the boundary condition on the first column:

$$\gamma_i(s) = \frac{\mathcal{G}_i+\gamma_i(0)}{s-D+D_{\text{adv}}} + D_{\text{adv}}\frac{\gamma_{i-1}}{s-D+D_{\text{adv}}}, \qquad \gamma_1(s) = \frac{\mathcal{G}_1+\gamma_1(0)}{s-D} \tag{4.48}$$

The recursive equation can be rewritten explicitly as:

$$\begin{aligned} \gamma_i(s) &= \frac{\mathcal{G}_1+\gamma_1(0)}{s-D}\left(\frac{D_{\text{adv}}}{s-D+D_{\text{adv}}}\right)^{i-1} \\ &+ \frac{1}{D_{\text{adv}}}\sum_{j=1}^{i-1}\left(\mathcal{G}_{i-j+1}+\gamma_{i-j+1}(0)\right)\left(\frac{D_{\text{adv}}}{s-D+D_{\text{adv}}}\right)^{j} \end{aligned} \tag{4.49}$$

We need a partial fraction expansion of the first term in order to obtain its inverse Laplace transform. We use the following power series to obtain the partial fraction expansion:

$$\begin{aligned} \sum_{j=0}^{i-1}\left(\frac{D_{\text{adv}}}{s-D+D_{\text{adv}}}\right)^{j} &= \frac{\left(\frac{D_{\text{adv}}}{s-D+D_{\text{adv}}}\right)^{i}-1}{\frac{D_{\text{adv}}}{s-D+D_{\text{adv}}}-1} \\ &= \frac{s-D+D_{\text{adv}}}{s-D} - \frac{D_{\text{adv}}}{s-D}\left(\frac{D_{\text{adv}}}{s-D+D_{\text{adv}}}\right)^{i-1} \end{aligned} \tag{4.50}$$

$$\frac{1}{s-D}\left(\frac{D_{\text{adv}}}{s-D+D_{\text{adv}}}\right)^{i-1} = \frac{1}{s-D} - \frac{1}{D_{\text{adv}}}\sum_{j=1}^{i-1}\left(\frac{D_{\text{adv}}}{s-D+D_{\text{adv}}}\right)^{j} \tag{4.51}$$

Using this identity, we obtain the solvable explicit expression.

$$\begin{aligned} \gamma_i &= \frac{\mathcal{G}_1+\gamma_1(0)}{s-D} \\ &+ \frac{1}{D_{\text{adv}}}\sum_{j=1}^{i-1}\left(\mathcal{G}_{i-j+1}+\gamma_{i-j+1}(0)-\mathcal{G}_1-\gamma_1(0)\right)\left(\frac{D_{\text{adv}}}{s-D+D_{\text{adv}}}\right)^{j} \end{aligned} \tag{4.52}$$

The first term is the advection-free solution of the first column, present in all equations of all columns due to the upstream difference. For $j=1$, the summation

starts from column i and sums up to $j = i - 1$, representing the second column. Therefore, the summation term consists of the difference of all prior columns from the first column, scaled by a power series. Using our previous definition of the u-functions, the analytic solution for column i is obtained by taking the inverse transform to time domain:

$$\begin{aligned}
\gamma_i &= \gamma_1(0)\exp(Dt) + \mathcal{G}_{1,1}u_1(t,D) + \mathcal{G}_{1,2}u_2(t,D) + \mathcal{G}_{1,3}u_3(t,D) \qquad (4.53)\\
&+ \frac{1}{D_{\text{adv}}}\sum_{j=1}^{i-1} D_{\text{adv}}(\gamma_{i-j+1}(0) - \gamma_1(0))\exp((D - D_{\text{adv}})t)\frac{(tD_{\text{adv}})^{j-1}}{(j-1)!}\\
&+ (\mathcal{G}_{i-j+1,1} - \mathcal{G}_{1,1})u_{1,j}(t, D - D_{\text{adv}})D_{\text{adv}}^j\\
&+ (\mathcal{G}_{i-j+1,2} - \mathcal{G}_{1,2})u_{2,j}(t, D - D_{\text{adv}})D_{\text{adv}}^j\\
&+ (\mathcal{G}_{i-j+1,3} - \mathcal{G}_{1,3})u_{3,j}(t, D - D_{\text{adv}})D_{\text{adv}}^j
\end{aligned}$$

As expected, the solution of a column depends on the sum of the difference between all columns before it and the first column. The effect of the first column is present and dominant as we have observed in the two column analysis in the previous section. The effect of each previous column is dependent on the wind speed through the advection divergence value. For the single integral u functions, we have shown that the amplitude of the functions are inversely proportional to the advection divergence, therefore the values of the u functions diminished for strong wind speeds. However, we need the higher order integral u functions and how they change for different columns to make a correct assessment on how previous columns affect the current column. For this purpose, we calculated their values for 10 columns, with each column having a D_{adv} value of 3.3 km/1 m s^{-1}. The value is selected to have a total column length of 33 km, an expected length of effect for the ocean column. The resulting functions are plotted in Figure 4.4.

The first and apparent trend for all three top subplots of the u functions is that the curves are delayed versions of each other within each subplot. An interesting fact is that the delay between any two curves is exactly equal to the time required for the wind to pass through a column: $\Delta x/V_x$, 3300 s in this case. The second observation is that, all curves are attenuated versions of each other. The attenuation is in fact exponential and follows the $\exp(Dx/V_x)$ trend. The

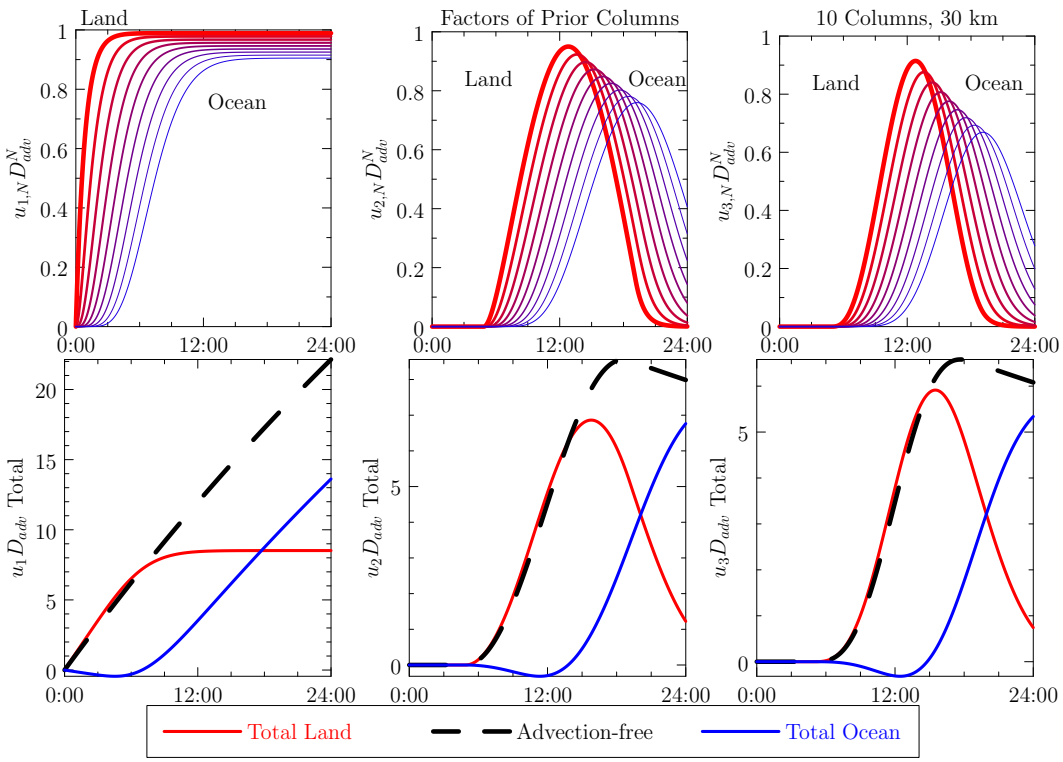

Figure 4.4: Individual effect of each column on the solution. (top) Higher order u functions for 10 columns. Each column has a horizontal column length of 3.3 km. The N^{th} order u function curve is scaled by D^N_{adv} for normalization as in Eq. (**??**). The given curves are required to solve the 10^{th} column (most inland) of the system. For the solution of the i^{th} column, only the first i curves from the left are needed. The left-most thick red curve is the original single integral u function. The right-most curve is the 9 integral u function and is scaled by the coefficients of the column next to the ocean. (bottom) The sum of all curves shown on the top three figures is represented by the red curves. The sum of all ocean terms in Eq. (**??**) is represented by the blue curves. The advection-free single integral u function solutions are represented by the black dashed curves.

underlying reason is explained in the next section. Finally, all curves have the same shape as the original underlying functions that were used to create the respective u functions: the constant 1 for u_1, μ_0 for u_2 and μ_0^2 for u_3.

In the multi-column solution, all curves are scaled with their respective column coefficients and summed up to obtain the actual solution with advection. To understand how effective the ocean column is with respect to the combined effect of all land columns, we set the value of all coefficients to be 1. This means

that all columns are accounted for in an equal manner. At the bottom of the figure, we plotted the sum of all land terms using the red curves, the sum of all ocean column terms using the blue curves and the advection-free single integral u functions using the dashed black curves. The total effect of all inland columns is dominant throughout the day until 18:00, when the ocean's delayed effect surpasses the total land's effect. The time difference between the total land (red) and total ocean (blue) curves is exactly 30000 s = 8.3 hours, corresponding to $N\Delta x/V_x$.

4.2.3 Conversion to Continuous Domain

Our model described until now assumes a discrete grid of multiple columns and we obtained the analytic solution for the provided model. Note that the grid can have any number of columns with any area size. The versatility of our analytic solution can be utilized to convert the discrete grid into a continuous area by making the grid size infinitesimal and taking the limit of the number of columns to infinity. In this section, we use this notion to obtain the analytic solution for a continuous domain. A continuous domain solution allows us to define any heterogeneous horizontal conditions, such as varying surface fluxes or different Bowen ratio across the selected domain. This gives us the versatility to represent and solve complex scenarios.

We start with the Laplace domain solution in Eq. (4.52). We fix the length of our domain to x_T and divide this domain into N columns as before. This results in a column size of $\Delta x = x_T/N$ using a uniform division. We start our coordinate system from $x = 0$, corresponding to the middle of the first column. Thus, the middle point of the i^{th} column corresponds to $x_i = ix_T/N$. Using these definitions, our advection divergence parameter becomes $D_{\text{adv}} = V_x N/x_T$. As found in Eq. (4.52), the solution of the i^{th} column is the weighted sum of all the columns before itself. Since we are taking the limit to infinitesimal sized columns, we need to convert the summation to the form of a Riemann summation, which will converge to an integral expression. So, we multiply and divide the expression by Δx and represent all variables using the position notation(x), instead of the

index notation(i):

$$\gamma(s,x_i) = \frac{\mathcal{G}(s,x_1)+\gamma_1(0)}{s-D} + \frac{1}{D_{\text{adv}}\Delta x}\sum_{j=1}^{i}\frac{(\mathcal{G}(s,x_{i-j+1})+\gamma_{i-j+1}(0)-\mathcal{G}(s,x_1)-\gamma_1(0))D_{\text{adv}}^{j}}{(s-D+D_{\text{adv}})^{j}}\Delta x \quad (4.54)$$

Next, we use the grid spacing definitions: $x_i = (i-1)\Delta x + x_1$ and $x_j = (j-1)\Delta x$, to show $x_{i-j+1} = x_i - x_j$. Finally, we use by its definition, $j = x_j N/x_T$. The resulting expression becomes:

$$\gamma(s,x_i) = \frac{\mathcal{G}(s,x_1)+\gamma(0,x_1)}{s-D} + \frac{1}{D_{\text{adv}}\Delta x}\sum_{j=1}^{i}\frac{(\mathcal{G}(s,x_i-x_j)+\gamma(0,x_i-x_j)-\mathcal{G}(s,x_1)-\gamma(0,x_1))D_{\text{adv}}^{\frac{x_jN}{x_T}}}{(s-D+D_{\text{adv}})^{\frac{x_jN}{x_T}}}\Delta x \quad (4.55)$$

As the next step, we take the limit as $N \to \infty$. The Riemann summation converges to an integral from $x_j = x_1$ to $x_j = x_i$. We replace $x = x_i$, $x_1 = 0$ and $x' = x_j$ for notational simplicity:

$$\gamma(x) = \lim_{N\to\infty}\frac{\mathcal{G}(s,0)+\gamma(0,0)}{s-D} + \frac{1}{D_{\text{adv}}\Delta x}\int_{x'=0}^{x}\frac{(\mathcal{G}(s,x-x')+\gamma(0,x-x')-\mathcal{G}(s,0)-\gamma(0,0))D_{\text{adv}}^{\frac{x'N}{x_T}}}{(s-D+D_{\text{adv}})^{\frac{x'N}{x_T}}}dx' \quad (4.56)$$

We first focus on the fraction inside the integral. In its current form, the fraction goes to a 1 and its exponent to ∞, resulting in a limit uncertainty. We expand both the numerator and the denominator by $1/D_{\text{adv}}$ and replace all $D_{\text{adv}} = V_x N/x_T$:

$$\lim_{N\to\infty}\frac{1}{\left[\left(\left(\frac{(s-D)x_T}{V_x}\right)\frac{1}{N}+1\right)^{N}\right]^{x'/x_T}}$$

We utilize the following mathematical limit identity to solve this limit:

$$\lim_{N\to\infty}\left(1+\frac{x}{N}\right)^{N} = \exp(x)$$

$$\Rightarrow \quad \lim_{N\to\infty}\frac{1}{\left[\left(\left(\frac{(s-D)x_T}{V_x}\right)\frac{1}{N}+1\right)^{N}\right]^{x'/x_T}} = \exp(-(s-D)x'/V_x)$$

Going back to our integral in Eq. (4.56):

$$\gamma(s,x) = \frac{\mathcal{G}(s,0)+\gamma(0,0)}{s-D}$$
$$+\frac{1}{V_x}\int_{x'=0}^{x}(\mathcal{G}(s,x-x')+\gamma(0,x-x')-\mathcal{G}(s,0)-\gamma(0,0))e^{(-(s-D)x'/V_x)}dx'$$

We can evaluate the $x=0$ terms in the integral combined with the term outside the integral:

$$\gamma(s,x) = \left(\frac{\mathcal{G}(s,0)+\gamma(0,0)}{s-D}\right)e^{\left(-\frac{sx}{V_x}\right)}e^{\left(\frac{Dx}{V_x}\right)}$$
$$+\frac{1}{V_x}\int_{x'=0}^{x}(\mathcal{G}(s,x-x')+\gamma(0,x-x'))e^{\left(-\frac{(s-D)x'}{V_x}\right)}dx'$$

Multiplying a function by an exponential function in the Laplace domain results in a time-shift in the time domain: $\exp(-cs)F(s) \rightarrow f(t-c)u(t-c)$, where $u(t-c)$ is the unit step function. We use this knowledge to take the inverse Laplace transform of the term outside the integral. The fraction inside the parentheses is the Laplace transform of $\gamma(t,x=0)$. The first exponential results in a time domain shift by $-x/V_x$ and the second exponential is a constant in Laplace domain, thus can be inverted as a factor. Therefore, the inverse transform can be simplified into:

$$\gamma(t,x) = \gamma\left(t-\frac{x}{V_x},0\right)e^{\frac{Dx}{V_x}}u(V_xt-x)$$
$$+\mathcal{L}^{-1}\left[\frac{1}{V_x}\int_{x'=0}^{x}(\mathcal{G}(s,x-x')+\gamma(0,x-x'))e^{\left(-\frac{(s-D)x'}{V_x}\right)}dx'\right]$$

Since Laplace transform is a linear operator, it can be switched with the integral operation. In the inside of the integral, the exponential term results in a time-domain shift for the first term and a Dirac-delta function for the second (constant) term:

$$\gamma(t,x) = \gamma\left(t-\frac{x}{V_x},0\right)\exp\left(\frac{Dx}{V_x}\right)u(V_xt-x)$$
$$+\frac{1}{V_x}\int_{x'=0}^{x}\left[u(V_xt-x')\mathcal{G}(t-\frac{x'}{V_x},x-x')+\gamma(0,x-x')\delta(t-\frac{x'}{V_x})\right]\exp\left(\frac{Dx'}{V_x}\right)dx'$$

Converting the integral variable using $t' = t - x'/V_x$:

$$\begin{aligned}\gamma(t,x) &= u(V_x t - x)\gamma\left(t - \frac{x}{V_x}, 0\right)\exp\left(\frac{Dx}{V_x}\right) \\ &+ u(x - V_x t)\gamma(0, x - tV_x)\exp(Dt) \\ &+ \exp(Dt)\int_{t'=t-x/V_x}^{t} u(t')\mathcal{G}(t', x - tV_x + t'V_x)\exp(-Dt')\,dt' \quad (4.57)\end{aligned}$$

First, note that $x_{oc} \triangleq V_x t$ corresponds to the amount of distance that an airmass originating from the ocean has traveled. Similarly, $t_{oc} \triangleq x/V_x$ describes the time required for an airmass originating over the ocean to reach the current column at distance x. Utilizing these remarks, the first term in Eq. (4.57) is the effect of ocean. The effect is delayed by t_{oc} and is attenuated by the subsidence divergence exponentially. For a fixed reference location, a stronger wind speed would reduce t_{oc}, resulting in a shorter delay and less attenuation, thus stronger ocean presence inland.

The second term is the effect of the initial condition of an inland column, x_{oc} distance away from position x. As the other initial conditions, this effect is attenuated by the subsidence divergence exponentially.

The final term is the combined effect of all prior columns, excluding the initial conditions, and combines only the window of a region where the wind speed had enough time to reach the current position (from $t - t_{oc}$ until t). The exponential factor inside the integral favors closer columns exponentially as compared to farther away ones.

Consider the case of an air column starting at the ocean at $t = 0$ and advected inland by wind. We change our frame of reference to the air parcel, such that $x = V_x t$. The solution of this air column becomes:

$$\gamma_{air}(t) = \gamma(0,0)\exp(Dt) + \exp(Dt)\int_{t'=0}^{t}\mathcal{G}(t', t'V_x)\exp(-Dt')\,dt' \quad (4.58)$$

The air column is affected cumulatively by each column it passes to shape its properties in time. The effects of any prior columns are attenuated exponentially by the subsidence divergence. However, since D is very small, this attenuation is

also very small. For $D = -3.75 \times 10^{-6}$ s^{-1}, this means that the air column will bear the effects of the columns it passed over the past $D^{-1} \simeq 3$ days in an almost equal manner. If wind is sustained over its path, the parcel incorporates the effects of a region of more than 200 km. However, synoptic-scale winds, Coriolis force and topology variations make this value physically invalid.

For example, for inversion height ($\gamma = z_{\mathrm{i}}$), $\mathcal{G}$ is the entrainment velocity. This means that the inversion height of the air column at any time is the difference between the total of all buoyancy fluxes along its path pushing up and sum of all subsidence pushing it down. Detailed analysis is provided in the sensitivity analysis section.

In the next section, we consider the special case of a homogeneous land area to understand the effect of distance to the ocean, how distant the effect of the ocean can reach and how the conditions in both regions affect the coupled solution.

4.2.4 Homogeneous Land Continuous Solution

For the special case of a homogeneous region, the expression in Eq. (4.57) can be simplified. For a homogeneous area, the dependence on position is neglected; $\mathcal{G}(t,x) = \mathcal{G}(t)$. Therefore, we simplify Eq. (4.57) to obtain the inland solution:

$$\gamma(t,x) = u(V_x t - x)\gamma_{\mathrm{ocean}}\left(t - \frac{x}{V_x}\right)e^{\frac{Dx}{V_x}} + u(x - V_x t)\gamma_{\mathrm{land}}(0)e^{Dt} + e^{Dt}\int_{t'=t-x/V_x}^{t} u(t')\mathcal{G}_{land}(t')e^{-Dt'}dt'$$

We divide the integral into two cases of $t < x/V_x$ and $t > x/V_x$:

$$\gamma(t,x) = u(V_x t - x)\gamma_{\mathrm{ocean}}\left(t - \frac{x}{V_x}\right)e^{\frac{Dx}{V_x}} + u(x - V_x t)\gamma_{\mathrm{land}}(0)e^{Dt} + u(x - V_x t)e^{Dt}\int_{t'=0}^{t} \mathcal{G}_{land}(t')e^{-Dt'}dt' + u(V_x t - x)\left[e^{Dt}\int_{t'=0}^{t} \mathcal{G}_{land}(t')e^{-Dt'}dt' - e^{\frac{Dx}{V_x}}e^{(Dt-Dx/V_x)}\int_{t'=0}^{t-x/V_x} \mathcal{G}_{land}(t')e^{-Dt'}dt'\right]$$

$$= \gamma_{\text{land}}(t) + u(V_x t - x) e^{\frac{Dx}{V_x}} \left[\gamma_{\text{ocean}} \left(t - \frac{x}{V_x} \right) - \gamma_{\text{land}} \left(t - \frac{x}{V_x} \right) \right] \tag{4.59}$$

γ_{land} and γ_{ocean} have been used to denote the land and ocean solutions without any advection. This expression shows the coupling of land and ocean clearly. At any inland position, the advection-free land solution is modified by a delayed ocean and delayed land difference attenuated exponentially with distance. A stronger subsidence divergence increases the attenuation and the effect of ocean stays limited. In contrast, a stronger wind decreases the attenuation and the ocean can reach more inland as expected. However, due to the subsidence being very small, the attenuation has only a small effect for wind speeds stronger than 1 m s^{-1}. For example, the attenuation is only 10% for a 30 km and 19% for a 60 km distance from the ocean. Any stronger wind will linearly scale these example values.

Eq. (4.59) can be rewritten to group the land terms together.

$$\begin{aligned} \gamma(t,x) &= \gamma_{\text{land}}(t) - \gamma_{\text{land}} \left(t - \frac{x}{V_x} \right) u(V_x t - x) e^{\frac{Dx}{V_x}} \\ &+ u(V_x t - x) e^{\frac{Dx}{V_x}} \gamma_{\text{ocean}} \left(t - \frac{x}{V_x} \right) \end{aligned} \tag{4.60}$$

Since the attenuation by the exponential term is small, we have a difference between the advection-free land solution and its delayed version. Any variable that changes slowly in time over the land, will be dominated by the ocean, since the difference between the not-delayed and delayed land terms will cancel each other out. For any variable with high variance in time, the coupled solution will deviate from the ocean's solution. As an example, shortwave terms will result in a large deviation after sunrise and sunset, where the observed variables before and after the delay will be significantly different. In contrast, ocean longwave terms will be dominant as the radiative temperatures vary slowly over time. More technical and numeric analysis is provided in the sensitivity analysis section.

4.3 Verification

To verify the correctness of our analytic solution, we implemented the differential equation versions of our model (Eq. (**??**)) and solved them using numerical

time-step integration. The time-step resolution is 100 s. Then, we compare the result of the numeric result with the analytic one for verification of correctness. The case study involves fifty columns, where the first column models the ocean with a constant surface flux. All the other columns model the land area with a constant Bowen Ratio ($\beta = 1$). All initial conditions are obtained from CGILS. The total studied area is 30 km and is divided uniformly across columns. The ocean column is not affected by advection. The wind speed is 4 m s^{-1}. Since the land area is homogeneous, we utilized our analytic homogeneous solution in Eq. (4.59). The results are given in Figure 4.5.

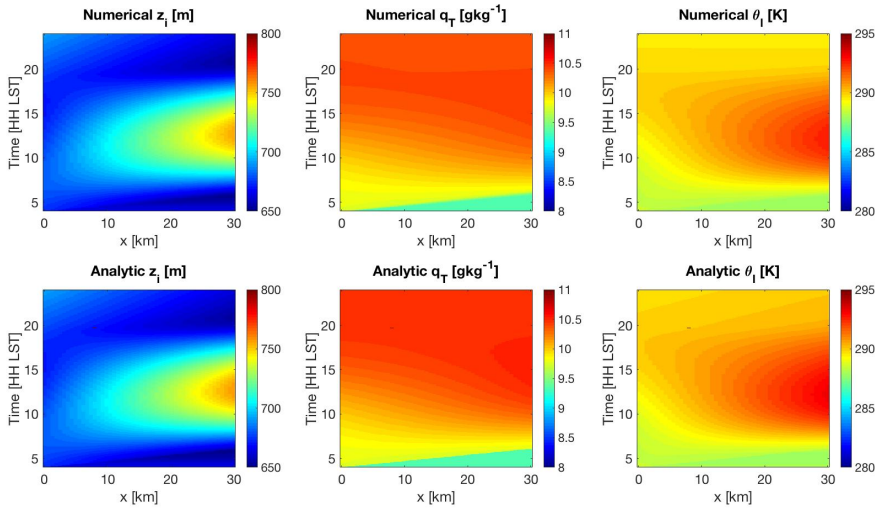

Figure 4.5: Numerical solution of 50 columns compared against the analytic solution.

The results show that our analytic solution correctly represents the solution to the set of governing differential equations. For the case of 50 columns, the difference is less than 1% for all variables. The difference further decreases as the columns get smaller, because the analytic solution provides the exact solution for a single point, whereas the numerical solution governs the solution of a column containing multiple points. As the columns get smaller, the regions converge to points and the solutions become the same.

4.4 Sensitivity Analysis

In the previous sections, we obtained the analytic solution for multiple columns of air coupled by large scale advection. In this section, we analyze the sensitivity of the solution to initial and boundary conditions.

4.4.1 Homogeneous Land Sensitivity

We use Eq. (4.59) instead of the more general solution of Eq. (4.57) for two main reasons: 1) the former provides a simpler solution, enabling detailed analysis of coefficients; 2) unless there is high resolution continuous information available over the studied region, the latter equation will converge to a series of homogeneous columns that uses the former equation to describe the relationship between the columns. We start by writing out the land and ocean functions in their general solution formats and assuming $V_x t \geq x$:

$$\gamma(t,x) = \gamma_{\text{land}}(0)e^{Dt} + e^{Dt}\int_{t'=0}^{t} \mathcal{G}_{land}(t')e^{-Dt'}dt'$$

$$+u(V_x t - x)e^{Dt}\left[\gamma_{\text{ocean}}(0) - \gamma_{\text{land}}(0) + \int_{t'=0}^{t-\frac{x}{V_x}} \left(\mathcal{G}_{ocean}(t') - \mathcal{G}_{land}(t')\right)e^{-Dt'}\right]dt'$$

$$= e^{Dt}\gamma_{\text{ocean}}(0) + e^{Dt}\left[\int_{t'=t-\frac{x}{V_x}}^{t} \mathcal{G}_{land}(t')e^{-Dt'}dt' + \int_{t'=0}^{t-\frac{x}{V_x}} \mathcal{G}_{ocean}(t')e^{-Dt'}dt'\right] \quad (4.61)$$

The first observation from the equation is that the initial condition of the land has no effect once the wind brings the ocean air to the studied position of x. The second remark is that the integral over land covers a fixed amount of time, x/V_x, whereas the integral over ocean grows over time. This means that the ocean's effect would overwhelm the coupled land solution in time. However, this accumulation is slightly counter-balanced by the exponentials inside the integrals, since the exponential for the land term is always $\exp(-Dx/V_x)$ times greater than its ocean counterpart.

Next, we replace the integrals by their u-function solutions:

$$\begin{aligned}\gamma(t,x) &= \mathcal{G}_{1,land}u_1(t) + \mathcal{G}_{2,land}u_2(t) + \mathcal{G}_{3,land}u_3(t) + \gamma_{\text{ocean}}(0)e^{Dt} \\ &+ e^{\frac{Dx}{V_x}}\Bigg[\left(\mathcal{G}_{1,ocean} - \mathcal{G}_{1,land}\right)u_1(t - \frac{x}{V_x}) \\ &+ \left(\mathcal{G}_{2,ocean} - \mathcal{G}_{2,land}\right)u_2(t - \frac{x}{V_x}) + \left(\mathcal{G}_{3,ocean} - \mathcal{G}_{3,land}\right)u_3(t - \frac{x}{V_x})\Bigg]\end{aligned}$$

We start the analysis for night time, where u_2 and u_3 are zero. However, since the effect of ocean arrives with a time delay, it is possible that the ocean air during day time can reach the land during night time. For the night time analysis, we assume that the daytime influences have vanished or are insignificant at $t > t_{\text{sunset}} + x/V_x$. Expanding the u_1 terms yields:

$$\begin{aligned}\gamma(t,x) &= \gamma_{\text{ocean}}(0)e^{Dt} + \mathcal{G}_{1,land}\left(\frac{e^{\frac{Dx}{V_x}} - 1}{D}\right) + \mathcal{G}_{1,ocean}\left(\frac{e^{Dt} - e^{\frac{Dx}{V_x}}}{D}\right) \\ &= \gamma_{\text{ocean}}(t) + \frac{\mathcal{G}_{1,ocean} - \mathcal{G}_{1,land}}{D}\left(1 - e^{\frac{Dx}{V_x}}\right) \\ &\approx \gamma_{\text{ocean}}(t) + \left(\mathcal{G}_{1,ocean} - \mathcal{G}_{1,land}\right)\frac{x}{V_x} \qquad (4.62)\end{aligned}$$

The resulting coupled column solution is the same as the advection-free ocean column at night time with a constant offset proportional to the distance to the ocean. The $\mathcal{G}_1$ coefficients represent the net longwave radiation terms at the inversion height and surface, and the surface heat flux terms. Therefore, a greater difference in radiative temperatures and surface fluxes between land and ocean will produce a greater offset and difference. Since the u_1 terms are present during both day and night times, the produced offset is valid at all times.

During day time, u_2 and u_3 terms are also present. To analyze this case, we focus on the land terms in Eq. (**??**) first. The expression consists of the finite difference of u_2 in time: $u_2(t) - u_2(t - x/V_x)$. u_2 and u_3 are based on the cosine of the solar zenith angle, μ_0, therefore are most dominant during solar noon, $t = 12 \times 3600$ s. For a distance of 30 km, the amount of time shift is small compared to t itself. Therefore, it is possible to treat this difference as a finite difference approximation for the first derivative and replace it by $\mu_0\frac{x}{V_x}$ for u_2 and $\mu_0^2\frac{x}{V_x}$ for u_3, as long as x is small enough compared to t. The resulting approximate expression

becomes:

$$\gamma(t,x) \approx \left(\mathcal{G}_{1,land} + \mathcal{G}_{2,land}\mu_0(t) + \mathcal{G}_{3,land}\mu_0^2(t)\right)\frac{x}{V_x} + e^{\frac{Dx}{V_x}}\gamma_{\text{ocean}}\left(t - \frac{x}{V_x}\right)$$

Subtracting γ_{ocean} from both sides and approximating the finite difference of the ocean terms as in the land terms yields:

$$\begin{aligned}\gamma(t,x) &\approx \gamma(t,0) + \left[\left(\mathcal{G}_{1,land} - \mathcal{G}_{1,ocean}\right) + \left(\mathcal{G}_{2,land} - \mathcal{G}_{2,ocean}\right)\mu_0(t)\right. \\ &+ \left.\left(\mathcal{G}_{3,land} - \mathcal{G}_{3,ocean}\right)\mu_0^2(t)\right]\frac{x}{V_x}\end{aligned}$$

Our previous chapters include detailed analyses of the coefficients under various conditions. We found that $\mathcal{G}_1 < 0$ and $\mathcal{G}_2, \mathcal{G}_3 > 0$ under standard atmosphere conditions. For small distances to the ocean, the resulting expression is very close to the ocean's solution itself. As the distance increases, the effect of the ocean decreases, whereas this decrease is counterbalanced by the land terms during the day and further reduced during the night.

For the inversion height, this expression converges to a very interesting result:

$$z_{\text{i}}(t,x) = z_{\text{i}}(t,0) + \left[w_{\text{e}}(t,x) - w_{\text{e}}(t,0)\right]\frac{x}{V_x} \tag{4.63}$$

The difference between the inversion heights is directly proportional to the difference between the entrainment velocities. As expected, this acts as a balancing factor for the inversion height over the land. During day time, the land mass has stronger turbulent fluxes and higher buoyancy flux, resulting in a stronger entrainment relative to the ocean. This results in a higher inversion height. In contrast, during night time, stronger radiative cooling of the land column results in a smaller entrainment, therefore results in a smaller inversion height. But, due to advection, this difference is damped in inverse proportion to the distance and will result in higher inversion heights during night time and lower during day time compared to the advection-free case. To show this, we expand the entrainment expressions:

$$\begin{aligned}w_{\text{e}}(t) &= \frac{1}{\zeta_D}\left[\text{F}_{\text{rad}}(z=0,t)\left(\frac{c_1 - 2s_1}{\text{c}_{\text{p}}\rho_{\text{air}}}\right) + \text{F}_{\text{rad}}(z=z_{\text{i}},t)\left(\frac{c_3 - 2s_2}{\text{c}_{\text{p}}\rho_{\text{air}}}\right)\right. \\ &+ \left. c_1\frac{\text{SHF}}{c_p\rho_{\text{air}}} + c_2\frac{\text{LHF}}{\text{L}_{\text{v}}\rho_{\text{air}}}\right]\end{aligned} \tag{4.64}$$

During the day, surface fluxes are stronger due to strong turbulent fluxes over the land and the net radiation terms are smaller due to higher attenuation over the ocean, resulting in a positive difference and a higher inversion height over the land. During night time, net radiation consists of only longwave radiation. The surface turbulent fluxes are stronger over the ocean as compared to the land, and the cloud top longwave cooling is also stronger over the ocean, resulting in a negative difference and a lower inversion height over the land.

For the total water mixing ratio, the expression becomes:

$$\begin{aligned} q_{\mathrm{T}}(t,x)z_{\mathrm{i}}(t,x) &= q_{\mathrm{T}}(t,0)z_{\mathrm{i}}(t,0) \\ &+ \left[q_{\mathrm{T,\ inv}}\left(w_{\mathrm{e}}(t,x)-w_{\mathrm{e}}(t,0)\right)+\frac{\mathrm{LHF}(t,x)-\mathrm{LHF}(t,0)}{\mathrm{L_v}\rho_{\mathrm{air}}}\right]\frac{x}{V_x} \end{aligned}$$

The entrainment velocity difference was studied for inversion heights and was found to be positive during day and negative during night. Since this difference is multiplied by the free troposphere mixing ratio, the sign of the difference is not affected. The second term involves the difference between the latent heat fluxes. The value and the sign of this difference highly depends on the Bowen Ratio of the land surface. For a moist surface, thus small Bowen Ratio, the land surface dominates. The high rate of evaporation over the moist land surface results in the ocean air to reduce the land column moisture. However, this reduction does not automatically mean that the relative humidity is also reduced. The relative humidity has a high sensitivity on temperature. For large Bowen Ratio, the evaporation decreases and the moisture content of the ocean air exceeds that of the land air, supplying it with moisture to counter-act dissipation.

For the liquid potential temperature, the expression is:

$$\begin{aligned} \theta_{\mathrm{l}}(t,x)z_{\mathrm{i}}(t,x) &= \theta_{\mathrm{l}}(t,0)z_{\mathrm{i}}(t,0)+\left[\theta_{\mathrm{l,\ inv}}\left(w_{\mathrm{e}}(t,x)-w_{\mathrm{e}}(t,0)\right)\right. \\ &+ \left.\frac{\mathrm{SHF}(t,x)-\mathrm{SHF}(t,0)}{\mathrm{c_p}\rho_{\mathrm{air}}}+\frac{\Delta\mathrm{F_{rad}}(t,x)-\Delta\mathrm{F_{rad}}(t,0)}{\mathrm{c_p}\rho_{\mathrm{air}}}\right]\frac{x}{V_x} \end{aligned}$$

$\Delta\mathrm{F_{rad}}$ is defined as the difference of net radiation at the inversion and surface. The expression is very similar to the total mixing ratio expression. However, for the ocean surface, the sensible heat flux is very small as compared to the land surface. Therefore, except for very small Bowen Ratio close to zero, the land column will be warmer during the day and cooler during the night. The higher heat

capacity of the ocean surface creates a temperature difference between land region that drives the temperature advection. The large temperature swings over the land are limited by the warmer air during the night and cooler air during the day from the ocean.

Combining all cases, liquid potential temperature is higher over the land relative to the ocean. However, the cool air over the ocean is advected over the land, cooling down the land column. The water mixing ratio advection highly depends on the Bowen Ratio of land, where for moist land surface the evaporation is higher and the ocean air results in a drier airmass. This process is reversed quickly with higher Bowen Ratio, where the moist ocean air increases the water content of the land. When combined together, temperature has a stronger effect on saturation. Since temperature is cooled over the land through advection, the saturation altitude and the lifting condensation level will drop, reducing the cloud base height. The diurnal variation of the inversion height is reduced due to the presence of advection, resulting in a smoother inversion height. The resulting effect is a thicker cloud, more persistence and less dissipation.

To show these properties, we have plotted the solution for inversion height, total water mixing ratio and liquid potential temperature for three different local times at 5:00, 8:00 and 11:00 in Figure 4.6. The wind speed is 4 m s^{-1}. The SHFand LHFof the ocean are kept constant at 5 W m^{-2} and 80 W m^{-2}, respectively. The land region is homogeneous with a Bowen Ratio of $\beta = 1$. All initial conditions are taken from CGILS-s12.

At 5:00 LST, net longwave radiation dominates the net radiation flux. The surface heat fluxes and cloud top longwave cooling over the ocean are stronger compared to land, which results in a lower buoyancy flux, more condensation and lower temperatures over the land area, as compared to the ocean. As expected, z_{i}, q_{T} and θ_{l} are smaller over the land compared to ocean. However, this difference is reduced by the advection from ocean.

At 8:00 LST, net shortwave radiation starts to balance the longwave cooling and we see a rise in temperature, in inversion height due to higher buoyancy and in total water mixing ratio due to higher evaporation. As we go inland, all three

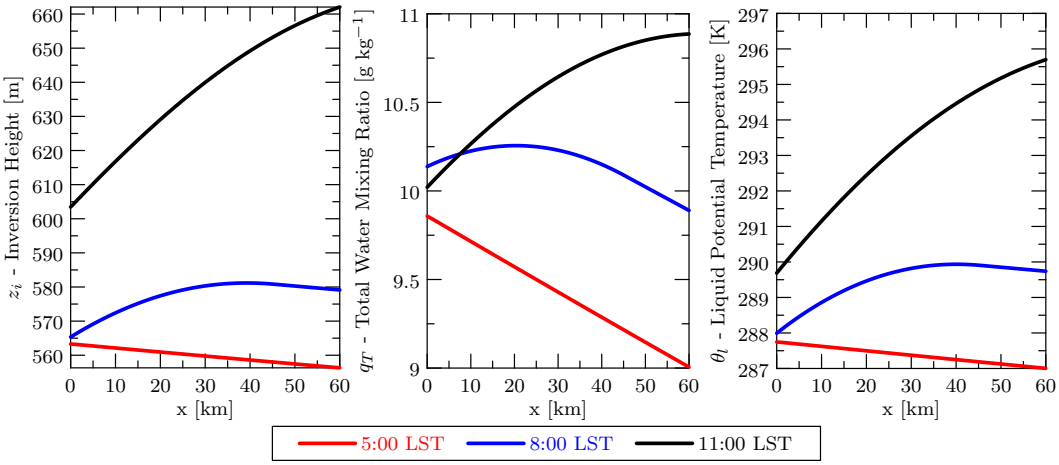

Figure 4.6: The effect of advection on inversion height, total water mixing ratio and liquid potential temperature and its dependence on the distance from the ocean. The land region is modeled using a constant Bowen Ratio of $\beta = 1$, whereas the ocean region has constant turbulent surface fluxes. Three local time instances are plotted: 5:00 to represent before sunrise, 8:00 to observe the mixed case of pre- and post-sunrise conditions on land and 11:00 for the day time cases.

variables make a concave curve. This is the delayed effect of the ocean column. The air column present over the ocean during the sunrise will arrive $x = 40$ km at this hour. The cooler night ocean air from 4 hours before reaches the $x = 60$ km position and the relatively warmer day air from 2 hours before reaches $x = 30$ km. Since different airmasses from times before and after sunrise reach different portions of land, we observe a strong change over different regions of the land. Compared to the red and black curves, blue curves don't have a monotonic change with distance as the effect of cool night time air and warmer day time air affect different regions of the land.

At 11:00 LST, net shortwave radiation is dominant across both ocean and land as we near solar noon. The heating results in strong surface heat fluxes over the land, driving buoyancy and entrainment up, as compared to the ocean surface. Increased warming and evaporation result in higher moisture content and temperatures. However, the cool ocean air limits the increase of the land air temperature and counter-acts the cloud dissipation process.

4.4.2 Inhomogeneous Land Sensitivity

Next, we continue with the inhomogeneous continuous solution, following the trajectory of an air parcel originating from the ocean and being advected inland. We use Eq. (4.58) for our analysis. For inversion height, the solution becomes:

$$z_{\mathrm{i}}(t) = z_{\mathrm{i}}(0)e^{Dt} + \frac{e^{Dt}}{\zeta_D}\int_{t'=0}^{t} e^{-Dt'}\left[\mathrm{F}_{\mathrm{rad}}(z=0,t')\left(\frac{c_1-2s_1}{\mathrm{c_p}\rho_{\mathrm{air}}}\right)\right.$$
$$\left. + \mathrm{F}_{\mathrm{rad}}(z=z_{\mathrm{i}},t')\left(\frac{c_3-2s_2}{\mathrm{c_p}\rho_{\mathrm{air}}}\right) + c_1\frac{\mathrm{SHF}(t')}{c_p\rho_{\mathrm{air}}} + c_2\frac{\mathrm{LHF}(t')}{\mathrm{L_v}\rho_{\mathrm{air}}}\right]dt'$$

Note that the net radiation fluxes and the surface heat fluxes are calculated for the column the air parcel is passing through at any time t': $x = V_x t'$. We evaluate these functions for a scenario, where the soil moisture decreases and the Bowen Ratio increases as we go from the ocean to further inland. Since the moisture decreases, we expect thinner clouds inland and a smaller attenuation of net radiation through the cloud. Furthermore, with increasing Bowen Ratio, more surface radiation is converted into sensible heat flux. Both factors cause the integrand to decrease for night cases and increase for day cases. Since the solution is an almost equally weighted average of the path, we expect inversion height to be lower over inland locations as compared to the advection-free case, resulting in a smoother and more uniform inversion height across its path.

For the total water mixing ratio, the solution becomes:

$$q_{\mathrm{T}}(t)z_{\mathrm{i}}(t) = q_{\mathrm{T}}(0)z_{\mathrm{i}}(0)e^{Dt} + \frac{e^{Dt}}{\zeta_D}\int_{t'=0}^{t} e^{-Dt'}\left[q_{\mathrm{T,\ inv}}w_{\mathrm{e}}(t') + \frac{\mathrm{LHF}(t')}{\mathrm{L_v}\rho_{\mathrm{air}}}\right]dt'$$

From the inversion height analysis, we know that the entrainment velocity will increase towards inland areas. As the Bowen Ratio increases, the amount of net radiation converted into latent heat flux decreases. The combined effect is a reduction in the integrand as the free troposphere mixing ratio is small and LHFdominates the expression. This is expected since the air gets drier as the evaporation reduces inland. The integral's result is the average across the path, which will result in higher total water mixing ratio inland.

Finally, for the liquid potential temperature, the solution is:

$$\theta_{\mathrm{l}}(t)z_{\mathrm{i}}(t) = \theta_{\mathrm{l}}(0)z_{\mathrm{i}}(0)e^{Dt} + \frac{e^{Dt}}{\zeta_D}\int_{t'=0}^{t} e^{-Dt'}\left[\theta_{\mathrm{l,\ inv}}w_{\mathrm{e}}(t') + \frac{\mathrm{SHF}(t')}{\mathrm{c_p}\rho_{\mathrm{air}}} + \frac{\Delta\mathrm{F_{rad}}(t')}{\mathrm{c_p}\rho_{\mathrm{air}}}\right]dt'$$

With increasing Bowen Ratio, entrainment increases, more net radiation is converted into sensible heat flux and a lower attenuation results in a smaller net radiation difference across the boundary layer. The combined effect is an increase in the integrand as the air gets warmer over the more inland areas. The average across the path will result in a lower temperature.

The analyses explain what can be expected in our scenario. The air parcel originating from the ocean and being advected inland experiences a lower buoyancy at the beginning of its journey, which increases towards more inland areas. But the total displacement in the inversion height is lower than an air parcel that would have stayed over the inland area all along, reducing the inversion height relatively. The beginning of the journey is a cooler column with higher evaporation due to the higher soil moisture content. This moisture is reduced and the air is warmed up along the path. However, the air parcel has a higher moisture and cooler temperature relative to the advection-free case of a column inland. Combined, this results in thicker and more persistent clouds to form inland, which was not possible for advection-free isolated conditions.

4.5 Conclusions

In the previous chapter, the analytic solution enabled us to extract hidden dependencies and study the sensitivity of cloud dynamics to initial and boundary conditions. The shortcoming was that the result only represents the isolated conditions and we observe that the clouds dissipate quickly unless the surface has a high rate of evaporation. In this chapter, we extended this model into the meso-scale by creating multiple columns that are coupled through advection. The multiple column solution is then transformed into a continuous-space closed-form analytic solution that can provide us how various regions interact with each other in the presence of a wind. The solution's correctness is verified against time-stepping

based numerical simulations. In the sensitivity analysis, we show that the ocean surface cools the ocean air, which is then advected over the land to cool down the land airmass. This results in a lower lifting condensation level and a thicker cloud. For isolated conditions, where the cloud was shown to dissipate, advection can be effective enough to make the clouds persist. Both analytic solutions enable the study of Sc under isolated and coupled conditions. The persistence of Sc over coastal areas is highly dictated by the presence of advection, as clouds quickly dissipate over land under advection-free conditions.

4.6 Analytic Derivations

4.6.1 Derivation for the effect of advection on Inversion Height

To connect the advection result of q_{T} and θ_{l} to the cloud parameters of inversion height and cloud base height, we revert back to the definition of virtual potential temperature to derive the velocity scale for the entrainment. We scale Eq. (4.9) and Eq. (4.10) by $c_{1,3}$ and $c_{2,4}$, respectively, and sum them up:

$$c_{1,3}\frac{d\theta_{\mathrm{l}}}{dt} + c_{2,4}\frac{dq_{\mathrm{T}}}{dt} = \frac{\overline{w'\theta'_{\mathrm{v}}}(0,t) + c_3 w_{\mathrm{e}}(t)\Delta\theta_{\mathrm{l,\,i}} + c_4 w_{\mathrm{e}}(t)\Delta q_{\mathrm{T,\,i}}}{z_{\mathrm{i}}(t)} + \frac{c_1 \mathrm{F}_{\mathrm{rad}}(0,t) - c_3 \mathrm{F}_{\mathrm{rad}}(z_{\mathrm{i}},t)}{\rho_{\mathrm{air}} \mathrm{c_p} z_{\mathrm{i}}(t)} - c_{1,3}\theta_{\mathrm{l,\,adv}} - c_{2,4} q_{\mathrm{T,\,adv}} \tag{4.65}$$

The resulting Eq. (4.65) is combined with Eq. (4.1) to obtain the expression for virtual potential temperature flux:

$$\overline{w'\theta'_{\mathrm{v}}}(z,t) = c_1 \frac{\mathrm{F}_{\mathrm{rad}}(0,t)}{\mathrm{c_p}\rho_{\mathrm{air}}} - c_{1,3}\frac{\mathrm{F}_{\mathrm{rad}}(z,t)}{\mathrm{c_p}\rho_{\mathrm{air}}} + \overline{w'\theta'_{\mathrm{v}}}(0,t) + \frac{z}{z_{\mathrm{i}}(t)}\left(\frac{c_3 \mathrm{F}_{\mathrm{rad}}(z_{\mathrm{i}},t) - c_1 \mathrm{F}_{\mathrm{rad}}(0,t)}{\rho_{\mathrm{air}}\mathrm{c_p}} - \overline{w'\theta'_{\mathrm{v}}}(0,t) - w_{\mathrm{e}}(t)(c_3\Delta\theta_{\mathrm{l,\,i}} + c_4\Delta q_{\mathrm{T,\,i}})\right)$$

The dependence on the advection terms are canceled out with this expression and it has no advection dependent terms. Therefore the resulting velocity scale, entrainment velocity and inversion height terms are not affected by the advection of q_{T} and θ_{l}. The only advection term that remains for inversion height is

its own advection:

$$\frac{dz_{\mathrm{i}}(t)}{dt} - Dz_{\mathrm{i}} = -z_{\mathrm{i,\ adv}} + \zeta_1 \mathrm{F_{rad}}(0,t) + \zeta_2 \mathrm{F_{rad}}(z_{\mathrm{i}},t) + \frac{\zeta_3}{z_{\mathrm{i}}} \int_{z=0}^{z=z_{\mathrm{i}}} c_{1,3} \mathrm{F_{rad}}(z,t) dz \quad (4.66)$$

4.6.2 Derivation for the effect of advection on Cloud Base Height

We use the cloud base height expression in [33] and linearize the dependence on q_{T} as in the previous chapter, such that:

$$z_{\mathrm{b}}(t) - z_{\mathrm{b}}(0) = \delta_1(q_{\mathrm{T}}(t) - q_{\mathrm{T}}(0)) + \delta_2(\theta_{\mathrm{l}}(t) - \theta_{\mathrm{l}}(0)) \quad (4.67)$$

δ_1 and δ_2 are constant expressions and are used for notational simplification. Eq. (4.67) is multiplied by z_{i} to obtain:

$$z_{\mathrm{b}} z_{\mathrm{i}} = z_{\mathrm{i}}(z_{\mathrm{b}}(0) - \delta_1 q_{\mathrm{T}}(0) - \delta_2 \theta_{\mathrm{l}}(0)) + \delta_1(q_{\mathrm{T}} z_{\mathrm{i}}) + \delta_2(\theta_{\mathrm{l}} z_{\mathrm{i}}) \quad (4.68)$$

The expressions $q_{\mathrm{T}} z_{\mathrm{i}}$ and $\theta_{\mathrm{l}} z_{\mathrm{i}}$ were solved using advection in this section for both cases of land and ocean. On top of their original form, there are additional terms added due to advection. These terms are directly scaled by δ_1 and δ_2 to have a linear effect on the cloud base height.

This chapter contains material from B. Ozge Akyurek, Jan Kleissl, "Closed-Form Analytic Solution of Cloud Dissipation for a Mixed-Layer Model", AMS Journal of Atmospheric Sciences 2017. The dissertation author was the primary investigator and author of this paper.

Chapter 5

Conclusions and Future Directions

In this dissertation, we model Sc clouds over coastal regions and obtain an analytic solution as opposed to the defacto method of numerical simulations. Numerical studies attempt to obtain sensitivity of parameter through exhaustive simulations, whereas our analytic solution provides all connections and dependencies in a single formula, shining light to connections that might not be observable as easily. Our solution covers a meso-scale setup connected through advection, while maintaining the high-accuracy solution on a micro-scale at each location.

The solutions presented in this dissertation are provided to guide related researchers in drawing conclusions on desired scenarios. The analytic solutions are light-weight, require almost no computation and, can provide equilibrium and extremum conditions. The results can be directly applied to weather predictions, solar forecasting and flight planning on short-term and renewable energy planning on the long-term since the analytic solution can provide any long-term future result immediately without having to *time-step* there.

It is hard to measure the effect of advection directly through sensor measurements, because it requires multiple sensors on the wind path. However, our analytic solution becomes an indispensible tool for these situations for estimating the affects of advection. If the results can be matched against real observations at the ocean and land end points, the properties of the region between the end points

can be directly inferred from our solutions, reducing the sensing costs.

5.1 Conclusions

We have provided an analytic closed-form solution to the cloud thickness evolution of stratocumulus clouds in a mixed layer model framework with a focus on application over coastal lands. This solution enabled sensitivity studies for inversion height, cloud base height and cloud thickness. While the parameter space was not explored exhaustively, for the typical base case chosen here, the following parameters influenced cloud thickness: Bowen Ratio, subsidence, and initial inversion height. Critical initial cloud thicknesses, that can be dissipated pre and post-sunrise were derived. Furthermore, we provided extrema analyses for inversion height and cloud thickness expressions to show when these variables reach their maximum and minimum values. Cloud dissipation can occur pre-sunrise, but this situation is unlikely in practice as such adverse conditions would likely have prevented cloud formation in the first place. If cloud does not dissipate pre-sunrise, then a morning maximum and afternoon minimum in cloud thickness is observed. For large initial inversion heights, this observation is reversed as a morning minimum for cloud thickness. If this minimum is associated with a cloud thickness of zero then the cloud deck breaks up during the day. If the minimum is associated with a cloud thickness greater than zero, then clouds are guaranteed to be maintained throughout the day.

For isolated conditions, it was shown that the cloud only persists for higher moist surfaces that supply the water content through the latent heat flux. However, there are also external meso-scale effects that contribute to the cloud dynamics. We extended our analytic solution to include large-scale horizontal advection, where multiple air columns are coupled through wind-flow. This discrete column-based solution is then extended into a continous solution. The solution states that the the ocean air column looses its effect exponentially as we go further inland. The effect is magnified for stronger winds, as more moisture and cool air can be advected inland, and diminished with stronger subsidence. The cool air reduces the boundary layer

temperature over the land and enhances cloud persistence for conditions that was not possible for the isolated case.

5.2 Future Directions

Even though the work presented in this dissertation provides a good match against LES results, the models and assumptions that were required to solve the equations limit its application compared to the variable meteorological conditions in the real world. Examples include soil moisture change, precipitation, wind profiles, and decoupling.

The constant Bowen ratio assumption looses its validity once the moisture content of the soil changes. This limitation can be overcome by including a better land surface model and a surface energy balance system. A surface energy balance system uses satellite based measurements along with meteorological information to estimate the surface parameters. An accurate land surface model is crucial as it determines the turbulent fluxes that drive the mixing process within the boundary layer.

Precipitation and drizzle are other important factors for the water budget within the boundary layer. The physics behind these phenomena is the subject of ongoing research. These models can be combined with the budget equations to include them within the analytic solution. This would enable us to observe the effect of precipitation and drizzle on the cloud dynamics.

An interesting future direction applicable to this work is the inclusion of wind-profiles. The columns are currently coupled through advection and wind-flow, however this also creates a feedback loop to the strength of wind-flow itself. The thermodynamic budgets of the boundary layer will directly affect the pressure distribution over the columns and will determine the wind speed.

Another direction is the study of decoupling. Even though decoupling occurs less frequently than the well-mixed conditions, multi-layer clouds can form in deep boundary layers that can result in the vertical column deviating from well-mixed conditions. Decoupling can occur under stronger winds and, stronger

temperature and moisture gradients. As we extended our solution to multiple columns, a similar approach can be used to extend into multiple clouds within a vertical column to study the decoupling process.

Bibliography

[1] D. R. Easterling, G. A. Meehl, C. Parmesan, S. A. Changnon, T. R. Karl, and L. O. Mearns, "Climate extremes: Observations, modeling, and impacts," *Science*, vol. 289, no. 5487, pp. 2068–2074, 2000. [Online]. Available: http://science.sciencemag.org/content/289/5487/2068

[2] G. Fischer, M. Shah, F. N. Tubiello, and H. van Velhuizen, "Socio-economic and climate change impacts on agriculture: an integrated assessment, 1990–2080," *Philosophical Transactions of the Royal Society of London B: Biological Sciences*, vol. 360, no. 1463, pp. 2067–2083, 2005. [Online]. Available: http://rstb.royalsocietypublishing.org/content/360/1463/2067

[3] O. E. Sala, F. Stuart Chapin, J. J. Armesto, E. Berlow, J. Bloomfield, R. Dirzo, E. Huber-Sanwald, L. F. Huenneke, R. B. Jackson, A. Kinzig, R. Leemans, D. M. Lodge, H. A. Mooney, M. Oesterheld, N. L. Poff, M. T. Sykes, B. H. Walker, M. Walker, and D. H. Wall, "Global biodiversity scenarios for the year 2100," *Science*, vol. 287, no. 5459, pp. 1770–1774, 2000. [Online]. Available: http://science.sciencemag.org/content/287/5459/1770

[4] S. Twomey, "Pollution and the planetary albedo," *Atmospheric Environment (1967)*, vol. 8, no. 12, pp. 1251 – 1256, 1974. [Online]. Available: http://www.sciencedirect.com/science/article/pii/0004698174900043

[5] D. M. Smith, S. Cusack, A. W. Colman, C. K. Folland, G. R. Harris, and J. M. Murphy, "Improved surface temperature prediction for the coming decade from a global climate model," *Science*, vol. 317, no. 5839, pp. 796–799, 2007. [Online]. Available: http://science.sciencemag.org/content/317/5839/796

[6] C.-H. Moeng, "A large-eddy-simulation model for the study of planetary boundary-layer turbulence," *Journal of the Atmospheric Sciences*, vol. 41, no. 13, pp. 2052–2062, 1984. [Online]. Available: https://doi.org/10.1175/1520-0469(1984)041⟨2052:ALESMF⟩2.0.CO;2

[7] D. S. Kaufman, D. P. Schneider, N. P. McKay, C. M. Ammann, R. S. Bradley, K. R. Briffa, G. H. Miller, B. L. Otto-Bliesner, J. T. Overpeck, and B. M. Vinther, "Recent warming reverses long-term arctic cooling,"

Science, vol. 325, no. 5945, pp. 1236–1239, 2009. [Online]. Available: http://science.sciencemag.org/content/325/5945/1236

[8] M. Khairoutdinov and Y. Kogan, "A new cloud physics parameterization in a large-eddy simulation model of marine stratocumulus," *Monthly Weather Review*, vol. 128, no. 1, pp. 229–243, 2000. [Online]. Available: https://doi.org/10.1175/1520-0493(2000)128⟨0229:ANCPPI⟩2.0.CO;2

[9] E. J. OConnor, R. J. Hogan, and A. J. Illingworth, "Retrieving stratocumulus drizzle parameters using doppler radar and lidar," *Journal of Applied Meteorology*, vol. 44, no. 1, pp. 14–27, 2005. [Online]. Available: https://doi.org/10.1175/JAM-2181.1

[10] Y. Tominaga and T. Stathopoulos, "Cfd simulation of near-field pollutant dispersion in the urban environment: A review of current modeling techniques," *Atmospheric Environment*, vol. 79, pp. 716 – 730, 2013. [Online]. Available: http://www.sciencedirect.com/science/article/pii/S1352231013005499

[11] J. P. Mellado, "Cloud-Top Entrainment in Stratocumulus Clouds," *Annual Review of Fluid Mechanics*, vol. 49, pp. 145–169, Jan. 2017.

[12] B. S. Elkins, M. Keyhani, and J. I. Frankel, "Surface heat flux prediction through physics-based calibration, part 2: Experimental validation," *Journal of Thermophysics and Heat Transfer*, 2013.

[13] R. J. Small, J. Bacmeister, D. Bailey, A. Baker, S. Bishop, F. Bryan, J. Caron, J. Dennis, P. Gent, H.-m. Hsu, M. Jochum, D. Lawrence, E. Muoz, P. diNezio, T. Scheitlin, R. Tomas, J. Tribbia, Y.-h. Tseng, and M. Vertenstein, "A new synoptic scale resolving global climate simulation using the community earth system model," *Journal of Advances in Modeling Earth Systems*, vol. 6, no. 4, pp. 1065–1094, 2014. [Online]. Available: http://dx.doi.org/10.1002/2014MS000363

[14] S. A. Klein and D. L. Hartmann, "The seasonal cycle of low stratiform clouds," *Journal of Climate*, vol. 6, no. 8, pp. 1587–1606, 1993. [Online]. Available: http://dx.doi.org/10.1175/1520-0442(1993)006⟨1587:TSCOLS⟩2.0.CO;2

[15] R. Eastman and S. G. Warren, "Diurnal cycles of cumulus, cumulonimbus, stratus, stratocumulus, and fog from surface observations over land and ocean," *Journal of Climate*, vol. 27, no. 6, pp. 2386–2404, 2014. [Online]. Available: http://dx.doi.org/10.1175/JCLI-D-13-00352.1

[16] M. Jamaly, J. L. Bosch, and J. Kleissl, "Aggregate ramp rates of distributed photovoltaic systems in san diego county," *IEEE Transactions on Sustainable Energy*, vol. 4, no. 2, pp. 519–526, April 2013.

[17] P. Kollias and B. Albrecht, "The turbulence structure in a continental stratocumulus cloud from millimeter-wavelength radar observations," *Journal of the Atmospheric Sciences*, vol. 57, no. 15, pp. 2417–2434, 2000. [Online]. Available: http://dx.doi.org/10.1175/1520-0469(2000)057⟨2417:TTSIAC⟩2.0.CO;2

[18] S. Bony, "Marine boundary layer clouds at the heart of tropical cloud feedback uncertainties in climate models," *Geophys. Res. Lett.*, vol. 32, no. 20, 2005. [Online]. Available: http://dx.doi.org/10.1029/2005GL023851

[19] D. K. Lilly, "Models of cloud-topped mixed layers under a strong inversion," *Quarterly Journal of the Royal Meteorological Society*, vol. 94, no. 401, p. 292309, Jul 1968. [Online]. Available: http://dx.doi.org/10.1002/qj.49709440106

[20] C. S. Bretherton and M. C. Wyant, "Moisture transport, lower-tropospheric stability, and decoupling of cloud-topped boundary layers," *J. Atmos. Sci.*, vol. 54, no. 1, p. 148167, Jan 1997. [Online]. Available: http://dx.doi.org/10.1175/1520-0469(1997)054⟨0148:MTLTSA⟩2.0.CO;2

[21] E. Serpetzoglou, B. A. Albrecht, P. Kollias, and C. W. Fairall, "Boundary layer, cloud, and drizzle variability in the southeast pacific stratocumulus regime," *Journal of Climate*, vol. 21, no. 23, pp. 6191–6214, 2008. [Online]. Available: http://dx.doi.org/10.1175/2008JCLI2186.1

[22] J. Rmillard, P. Kollias, E. Luke, and R. Wood, "Marine boundary layer cloud observations in the azores," *Journal of Climate*, vol. 25, no. 21, pp. 7381–7398, 2012. [Online]. Available: http://dx.doi.org/10.1175/JCLI-D-11-00610.1

[23] B. Stevens, "Entrainment in stratocumulus-topped mixed layers," *Quarterly Journal of the Royal Meteorological Society*, vol. 128, no. 586, pp. 2663–2690, 2002. [Online]. Available: http://dx.doi.org/10.1256/qj.01.202

[24] M. Fang, B. A. Albrecht, V. P. Ghate, and P. Kollias, "Turbulence in continental stratocumulus, part i: External forcings and turbulence structures," *Boundary-Layer Meteorology*, vol. 150, no. 3, pp. 341–360, 2014. [Online]. Available: http://dx.doi.org/10.1007/s10546-013-9873-3

[25] P. Caldwell, C. S. Bretherton, and R. Wood, "Mixed-layer budget analysis of the diurnal cycle of entrainment in southeast pacific stratocumulus," *J. Atmos. Sci.*, vol. 62, no. 10, pp. 3775–3791, oct 2005. [Online]. Available: http://dx.doi.org/10.1175/JAS3561.1

[26] V. E. Larson, K. E. Kotenberg, and N. B. Wood, "An analytic longwave radiation formula for liquid layer clouds," *Monthly Weather Review*, vol. 135, no. 2, p. 689699, Feb 2007. [Online]. Available: http://dx.doi.org/10.1175/MWR3315.1

[27] P. G. Duynkerke, "Turbulence, radiation and fog in dutch stable boundary layers," *Boundary-Layer Meteorology*, vol. 90, no. 3, p. 447, Mar. 1999. [Online]. Available: http://dx.doi.org/10.1023/A:1026441904734

[28] R. Seager, M. B. Blumenthal, and Y. Kushnir, "An advective atmospheric mixed layer model for ocean modeling purposes: Global simulation of surface heat fluxes," *Journal of Climate*, vol. 8, no. 8, pp. 1951–1964, 1995. [Online]. Available: http://dx.doi.org/10.1175/1520-0442(1995)008⟨1951:AAAMLM⟩2.0.CO;2

[29] B. Stevens, C.-H. Moeng, A. S. Ackerman, C. S. Bretherton, A. Chlond, S. de Roode, J. Edwards, J.-C. Golaz, H. Jiang, M. Khairoutdinov, M. P. Kirkpatrick, D. C. Lewellen, A. Lock, F. Mller, D. E. Stevens, E. Whelan, and P. Zhu, "Evaluation of Large-Eddy Simulations via observations of nocturnal marine stratocumulus," *Mon. Wea. Rev.*, vol. 133, no. 6, pp. 1443–1462, jun 2005. [Online]. Available: http://dx.doi.org/10.1175/mwr2930.1

[30] M. S. Ghonima, T. Heus, J. R. Norris, and J. Kleissl, "Factors controlling stratocumulus cloud lifetime over coastal land," *J. Atmos. Sci.*, vol. 73, no. 8, pp. 2961–2983, aug 2016. [Online]. Available: http://dx.doi.org/10.1175/JAS-D-15-0228.1

[31] J. J. van der Dussen, S. R. de Roode, and A. P. Siebesma, "Factors controlling rapid stratocumulus cloud thinning," *Journal of the Atmospheric Sciences*, vol. 71, no. 2, pp. 655–664, 2014. [Online]. Available: http://dx.doi.org/10.1175/JAS-D-13-0114.1

[32] P. G. Duynkerke, S. R. de Roode, M. C. van Zanten, J. Calvo, J. Cuxart, S. Cheinet, A. Chlond, H. Grenier, P. J. Jonker, M. Khler, G. Lenderink, D. Lewellen, C.-L. Lappen, A. P. Lock, C.-H. Moeng, F. Mller, D. Olmeda, J.-M. Piriou, E. Sánchez, and I. Sednev, "Observations and numerical simulations of the diurnal cycle of the EUROCS stratocumulus case," *Quarterly Journal of the Royal Meteorological Society*, vol. 130, no. 604, pp. 3269–3296, oct 2004. [Online]. Available: http://dx.doi.org/10.1256/qj.03.139

[33] M. S. Ghonima, J. R. Norris, T. Heus, and J. Kleissl, "Reconciling and validating the cloud thickness and liquid water path tendencies proposed by R. Wood and J. J. van der Dussen et al." *J. Atmos. Sci.*, vol. 72, no. 5, p. 20332040, May 2015. [Online]. Available: http://dx.doi.org/10.1175/JAS-D-14-0287.1

[34] R. Goody, *Principles of atmospheric physics and chemistry*. Oxford University Press, 1995.

[35] E. P. Shettle and J. A. Weinman, "The transfer of solar irradiance through inhomogeneous turbid atmospheres evaluated by Eddingtons approximation,"

J. Atmos. Sci., vol. 27, no. 7, p. 10481055, Oct 1970. [Online]. Available: http://dx.doi.org/10.1175/1520-0469(1970)027⟨1048:TTOSIT⟩2.0.CO;2

[36] J. D. Turton and S. Nicholls, "A study of the diurnal variation of stratocumulus using a multiple mixed layer model," *Quarterly Journal of the Royal Meteorological Society*, vol. 113, no. 477, p. 9691009, Jul 1987. [Online]. Available: http://dx.doi.org/10.1002/qj.49711347712

[37] C. S. Bretherton, S. K. Krueger, M. C. Wyant, P. Bechtold, E. Van Meijgaard, B. Stevens, and J. Teixeira, "A GCSS boundary-layer cloud model intercomparison study of the first astex lagrangian experiment," *Boundary-Layer Meteorology*, vol. 93, no. 3, p. 341, Dec. 1999. [Online]. Available: http://dx.doi.org/10.1023/A:1002005429969

[38] M. Zhang, C. S. Bretherton, P. N. Blossey, S. Bony, F. Brient, and J.-C. Golaz, "The CGILS experimental design to investigate low cloud feedbacks in general circulation models by using single-column and Large-Eddy Simulation models," *Journal of Advances in Modeling Earth Systems*, vol. 4, no. 4, 2012, m12001. [Online]. Available: http://dx.doi.org/10.1029/2012MS000182

[39] D. Bolton, "The computation of equivalent potential temperature," *Monthly Weather Review*, vol. 108, no. 7, pp. 1046–1053, 1980. [Online]. Available: http://dx.doi.org/10.1175/1520-0493(1980)108⟨1046:TCOEPT⟩2.0.CO;2

[40] B. O. Akyurek and J. Kleissl, "Closed-form analytic solution of cloud dissipation for a mixed layer model," *Journal of the Atmospheric Sciences*, vol. 0, no. 0, p. null, 0.

[41] S. Nicholls and J. Leighton, "An observational study of the structure of stratiform cloud sheets: Part i. structure," *Quarterly Journal of the Royal Meteorological Society*, vol. 112, no. 472, p. 431460, Apr 1986. [Online]. Available: http://dx.doi.org/10.1002/qj.49711247209

[42] J. S. Wakefield and W. H. Schubert, "Mixed-layer mode simulation of eastern north pacific stratocumulus," *Monthly Weather Review*, vol. 109, no. 9, pp. 1952–1968, 1981. [Online]. Available: https://doi.org/10.1175/1520-0493(1981)109⟨1952:MLMSOE⟩2.0.CO;2